Master's thesis

NTNU
Norwegian University of Science and Technology
Faculty of Natural Sciences
Department of Physics

Aleksandar Kavazov

Fabrication of platinum mushroom-shaped microelectrode array for *in vitro studies of neural networks and neural network pathologies*

Master's thesis in Physics
Supervisor: Prof. Pawel Sikorski
Co-supervisor: Assoc. Prof. Ioanna Sandvig, Assoc. Prof. Axel Sandvig, Ph.D. Nicolai Winter-Hjelm
May 2021

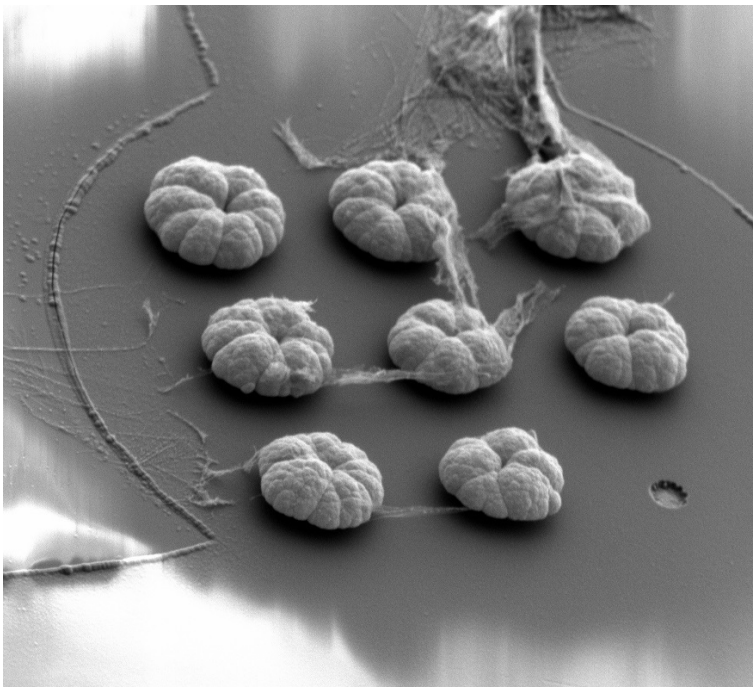

NTNU
Norwegian University of Science and Technology

Aleksandar Kavazov

Fabrication of platinum mushroom-shaped microelectrode array for *in vitro studies of neural networks and neural network pathologies*

Master's thesis in Physics
Supervisor: Prof. Pawel Sikorski
Co-supervisor: Assoc. Prof. Ioanna Sandvig, Assoc. Prof. Axel Sandvig, Ph.D. Nicolai Winter-Hjelm
May 2021

Norwegian University of Science and Technology
Faculty of Natural Sciences
Department of Physics

NTNU
Norwegian University of
Science and Technology

This page is intentionally left blank.

The thesis is intended to be printed in color.

Abstract

The field of electrophysiology experiences huge progress in the application of microelectrode arrays (MEAs) for a better understanding of the mechanisms underlying complex brain functions. Various recording platforms with tailored functionality have been developed in recent years. They opened new possibilities in the analysis of spontaneous and evoked action potentials by means of extracellular recording and stimulations of neural cells. Modern MEAs have tens to thousands of channels to investigate the activity of small portions of brain slices or neural cell cultures. An important aspect in building such devices is to minimize the signal-to-noise ratio (SNR) during recordings and to provide an efficient coupling coefficient between the cells and the electrodes during simulations. In recent years, several groups investigated the opportunities to increase the SNR by using mushroom-shaped 3D microelectrodes. Reportedly, this type of electrodes possesses the ability to obtain intracellular recordings without invading and damaging the cells which is a great advantage over other techniques used for this type of recordings. This makes mushroom-shaped MEAs an attractive alternative in many neurosciences research projects and preclinical drug testing programs.

The current work describes the fabrication of mushroom-shaped microelectrodes with a focus on the neurobiological background necessary for the reader to understand the basic concepts behind neuron-electrode signal transduction. Also, described are the instruments and techniques of nanofabrication used in this project. They include photolithography, thin-film deposition, and electroplating. Furthermore, results from the optimization of the process steps are presented to bring attention to the possibilities for improvement of the manufacturing methods. The development of the mushroom shape of the electrodes was successful. Their size (cap diameter 5 um), however, was too big to trigger engulfment from neurons and signs of intracellular recordings were not observed. And lastly, a discussion of future improvements and some limitations of the instruments and the materials used is provided by the author, giving an overview of the challenges faced during the development of the MEA and pointing a direction towards refinement of the performance of the electrodes.

Sammendrag

Feltet elektrofysiologi opplever store fremskritt i anvendelsen av mikroelektro de arrayer (MEA) for bedre forståelse av mekanismene som ligger til grunn for komplekse hjernefunksjoner. Ulike opptak plattformer med skreddersydd funksjonalitet er utviklet de siste årene. De åpnet nye muligheter i analysen av spontane og fremkalte handlingspotensiale ved hjelp av ekstracellulære opptak og stimulering av nevrale celler. Moderne MEAs har titusenvis av kanaler for å undersøke aktiviteten til små porsjoner av hjerne skiver eller nevrale cellekulturer. Et viktig aspekt ved å bygge slike enheter er å minimere signal-til-støy-forholdet (SNR) under opptak og å gi en effektiv kobling koeffisient mellom cellene og elektrodene under stimulering. I de siste årene har flere grupper undersøkt mulighetene for å øke SNR ved å bruke soppformede 3D-mikroelektroder. Angivelig har denne typen elektroder muligheten til å oppnå intracellulære opptak uten å invadere og skade cellene, noe som er en stor fordel i forhold til andre teknikker som brukes for denne typen opptak. Dette gjør soppformede MEA til et attraktivt alternativ i mange forskningsprosjekter innen nevrovitenskap og prekliniske legemiddeltester.

Det nåværende arbeidet beskriver fabrikasjonen av soppformede mikroelektroder med fokus på den nevrobiologiske bakgrunnen som er nødvendig for at leseren skal forstå de grunnleggende konseptene bak nevron elektrode signaltransduksjon. Også beskrevet er instrumentene og teknikkene for nanofabrikasjon brukt i dette prosjektet. Videre presenteres resultater fra optimalisering av prosess trinnene for å gjøre oppmerksom på mulighetene for forbedring av produksjonsmetodene. Og til slutt, en diskusjon om slike forbedringer og noen begrensninger av instrumentene og materialene som brukes, er gitt av forfatteren, som gir en oversikt over utfordringene ved utvikling av slike MEAs, og gir forslag til videreutvikling av disse for enda bedre ytelse.

Preface

This Master´s thesis is submitted in partial fulfillment of the requirements for the degree Master of Science in Physics at the Norwegian University of Science and Technology (NTNU). The work presented has been performed during the academic year of 2020/2021 at the Department of Physics (MSPHYS), as part of the course FY3900 - Master Thesis in Physics. Experimental work has been carried out in laboratories of the Department of Neuromedicine and Movement Science (INB) and in the cleanroom of NTNU NanoLab. Due to the Covid-19 outbreak, access to lab facilities has been limited during parts of the project. This has mainly affected work related to cell preparations and recordings, for which Nicolai Winter-Hjelm and Edevard Hvide have consequently conducted most work presented herein.

Acknowledgments

First and foremost, I would like to extend my sincerest gratitude to my supervisor Pawel Sikorski. He has been an invaluable mentor throughout my master's project. His help with planning experiments, discussing problems arising along the way, pushing me to think critically, and giving advice and feedback on the written thesis has been greatly appreciated. Furthermore, I would like to thank Pawel Sikorski for giving feedback on my written thesis, and for contributing to the foundation of this work.

A great thank you is also extended to Yanna Sandvig, Axel Sandvig, and Peter Kollensperger for co-supervising my project and giving me the opportunity to be a part of their research group at the Institute of Neuromedicine and Movement Science and at NTNU NanoLab. Their thrust has been highly appreciated, and I am truly looking forward to employing the knowledge and skills gained along with this project.

In addition, I would like to thank my co-supervisors Nicolai Winter-Hjelm and Janelle Weir for their genuine support, feedback, and help throughout the project. Their ideas, inputs, and knowledge made this project possible, and they have given me a whole new toolbox of practical and theoretical skills that will come to great use in the future. I would also like to thank master student Edevard Hvide, who has taken care of most of the cell work of this project.

Gratitude is also extended to engineers Mathilde Barriet, Mark Chiappa, Martijn de Roosz, Jens Hövik, Paulo Brito, and Amin Hossein Zavieh at NTNU NanoLab for training in instruments and technical support throughout the project. They have been truly irreplaceable in giving advice when processes and instruments have been uncooperative and when techniques and protocols have not given the desired results.
The Research Council of Norway is acknowledged for the support to the Norwegian Micro- and Nano-Fabrication Facility, NorFab.

Table of contents

List of figures:

List of tables:

Abbreviations:

CNS - central nervous system
AP - action potential
ATP - adenosine triphosphate
RMP - resting membrane potential
PSC - postsynaptic current
PSP - postsynaptic potential
EPSP - excitatory postsynaptic potential
IPSP - inhibitory postsynaptic potential
MRI - magnetic resonance imaging
LTP - long-term potentiation
LTD - long-term depression
AMPA - α-amino-3-hydroxy-5-methyl-4-isoxazole propionic acid
NMDA - *N*-methyl-D-aspartate
AD - Alzheimer's disease
PD - Parkinson's disease
ALS- Amyotrophic lateral sclerosis
FND - Functional neurological disorders
LSD - lysergic acid diethylamide
Aβ - β-amyloid peptide
NSE - neuron-specific enolase
CPK-BB - creatinine phosphokinase isoenzyme BB
MBP - myelin basic protein
BBB - blood-brain barrier
BNB - blood-nerve barrier
PNI - peripheral nerve injury
LFP - local field potential
SNR - signal-to-noise ratio
EP - extracellular potential
MEA - microelectrode array
IPA - isopropyl alcohol
SNR - signal-to-noise ratio
SMU - source measuring unit
PAD - pulsed amperometric detection

Chapter 1

Introduction

One of the greatest challenges of this century is to understand how the human brain stores and processes information. Many international projects put efforts in order to reveal more about the mechanisms of this incredible machinery. Understanding the basic concepts in more detail could help with the treatment of neurological diseases, building more elaborate brain-machine interfaces, or more efficient neuromorphic computing systems. There are two major approaches to study the brain termed top-down and bottom-up. The first approach looks at the nervous system as a whole and investigates behavioral changes by means of stimulation of different areas. The second approach focuses on an exploration of the smallest computing units of the brain, the neurons, by means of *in vitro* studies. In the last two decades, *in vitro* platforms for neural networks have been tailored for various research purposes such as investigation of the mechanisms underlying epilepsy or the regeneration of cells after axotomy. The development of nanofabrication techniques has enabled the prototyping of such platforms, making them attractive tools for neuroscientists. The primary advantage of *in vitro* studies is that they can support a controlled environment, reducing the experimental variations. This allows testing specific cellular and molecular hypotheses.

Microelectrode arrays (MEAs) are a commonly used tool for the study of *in vitro* neural networks. Their ability to either record or stimulate neurons by simultaneously accessing multiple sites of neural circuits makes them a valuable tool. Different models of MEAs such as planar, high-density, flexible, or intracellular have been employed to investigate the neural mechanisms of communication and response to drug treatments. The currently available electrophysiological techniques for intracellular recordings have the disadvantage of damaging the cells which leads to cell death in a few hours post recordings. This project focuses on the fabrication of novel mushroom-shaped microelectrodes for intracellular recordings. The main advantage of such electrodes is that their shape and size trigger the natural tendency of the neurons for phagocytosis. The neurons partially engulf the electrodes, leading to a strong coupling and higher signal-to-noise ratio of the recordings, which is advantageous for spike sorting and tracking. The intracellular-like profile of such recordings has gotten a lot of attention in the last few years. Having the advantage to obtain such recordings without damaging the cells, mushroom-shaped electrodes are a promising tool for advances in many fields of neuroscience -from drug delivery and neurotoxicity to developing better models of neurological diseases and investigating the computational capabilities of neural networks.

The main aim of this project has been to fabricate a 3D mushroom-shaped MEA for neural signal detection and test its biocompatibility and functionality. This has been done by design and optimization of photolithographic and electrochemical deposition process steps. The device consists of a recording site, built onto a borosilicate glass substrate, and PDMS structures forming closed compartments for the neural cell cultures. The following chapters

will give a brief overview of the theoretical concepts, instruments, and methods of fabrication used throughout this project. First, the most important aspects of neurobiology will be presented, followed by a theoretical framework for the relevant methods of electrophysiology and electrochemical deposition. Next, instruments, materials, and techniques used in this project will be introduced, followed by results from optimization of the fabrication steps and from testing the device with cell cultures. Lastly, a discussion of the challenges faced during optimization of the process steps as well as perspectives for their resolution is provided, followed by a protocol for the fabrication of platinum 3D mushroom-shaped MEAs.

Chapter 2

Theory

2.1 Neurobiology

The human brain is considered to be the most complex object known to man. With its staggering number of neurons of approximately 86 billion and up to 10 000 times more connections between them, it is still not fully mapped and understood[1,2]. The advancement of staining and imaging techniques is the major factor that contributes to a better understanding of the structure of these functional units of the brain and the connections between them. Using these techniques together with biochemical and electrophysiological methods allows examining the development and the function of the neurons and how they group to form complex networks capable of supporting perception, memory, and other cognitive processes that occur seemingly synergetic in the brain. Modeling these networks by employing information theory and mathematics is now an important part of neurobiology and a potential tool for the development of medical treatments and diagnostic methods for Alzheimer's and Parkinson's diseases[3,4]. To examine in detail certain aspects of these diseases, reductionist approaches such as *in vitro* research models are proven useful. An important part of the implementation of these models is the microelectrode arrays platform for neural recordings and stimulations. The design of such platforms can vary according to the intended purpose of use which makes them an attractive tool for prototyping medical devices and examining the effect of drugs on certain types of cells[5-7].

The next sections are meant to provide the reader with an overview of the anatomy of the neurons and the main structures and processes involved in signal propagation.

2.1.1 Cell types in the nervous system

The nervous system consists of two main categories of cells: neurons and supporting glial cells. Neurons can be classified by their function, morphology, chemical activity, or gene expression. They are the cells receiving sensory inputs from the environment, sending motor commands to the muscles, and coordinating the signal transduction. Thus, they can be classified by their function: sensory neurons, motor neurons, and interneurons. The enormous diversity of the neurons based on their receptors and neurotransmitter release will not be covered in this work. However, all neurons share common traits when it comes to their anatomy and morphology and they will be presented in the following section.

The glial cells outnumber the neurons in a ratio of 3:1 according to discussion in more recent papers[7]. Despite their number, they are not involved in electrical signal propagation but rather supporting it. There are three types of glial cells: astrocytes, oligodendrocytes, and microglial cells. An important function of astrocytes is to maintain an appropriate chemical

balance for neuronal signaling. Oligodendrocytes provide myelination of the axons in the CNS. Their counterparts in the periphery are the Schwann cells. However, unlike oligodendrocytes, each myelinating Schwann cell provides insulation to only one axon. This arrangement supports the saltatory conduction of action potentials with repropagation at the nodes of Ranvier. This increases the speed of conduction and saves energy. Microglial cells have a function similar to that of macrophages which are the immune cells of the body. They remove cellular debris from injury sites and secrete pro-inflammatory signaling molecules that are also produced by the immune system.

2.1.2 Structure of the neurons

The neurons are highly specialized to receive and transmit electrical signals. The first and most obvious feature is their morphology. The extensive branching that connects each neuron with its neighbors protrudes from the cell body called soma. These branches are called neurites and are the common name for all protrusions from the soma. The neurites can be further separated into an axon and dendrites (see Fig. 1). Each neuron has most commonly one axon which sends an electrical signal to the dendrites of other neurons, their soma, or in some cases - other axons. The axon can branch out at the end and reach many dendrites of different neurons or many axons can terminate on one neuron. The number of inputs (convergence) and outputs (divergence) of a neuron is an important parameter that categorizes the degree of connectivity of the cell [8]. The axon endings form special contacts with the dendrites called synapses. They are specialized parts of the neuron where the secretory apparatus from the presynaptic site sends signaling molecules (neurotransmitters) to the postsynaptic receptors. This transmission of neurotransmitters happens in the vicinity of these synaptic connections called the synaptic cleft. Only some neurons are continuously connected through gap junctions and allow for passive current flow from one to another contributing to faster signal transduction and synchronization of electrical activity among populations of neurons [9].

Another important feature of the nerve cells that are directly involved in the transmission of electrical signals is their plasma membrane [11]. The main function of the plasma membrane is to separate the interior and the exterior of cells. It consists of a lipid bilayer and membrane proteins with different functions. In one individual cell, there can be up to hundreds of different types of protein each with its function such as localizing metabolic pathways, facilitating diffusion and active transport, transducing signals, cellular identification, and cytoskeletal connections.

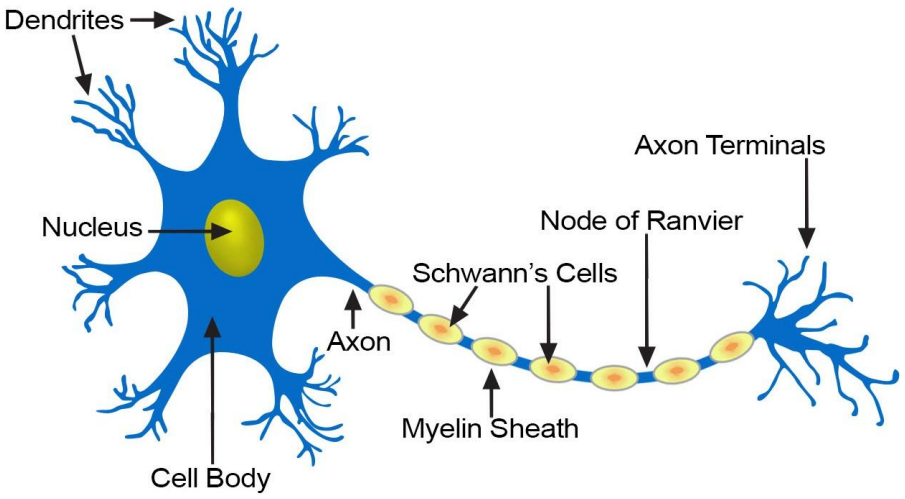

Fig. 1 Basic structure of a neuron. The common features are indicated with arrows, their size is not up to scale. Image adapted from [10].

Channel proteins for example control the rate at which proteins of specific molecules can travel across the membrane. Signal proteins on the other hand are responsible for the binding of certain substances and subsequently sending a signal, often as a chemical signaling cascade, into the cell activating related cellular responses.

2.1.3 Resting Membrane Potential and Action Potential

Even when the neurons do not fire an AP, they support a voltage (charge) difference across their membrane called resting membrane potential or RMP (see Fig.2). This resting potential is determined by the concentration differences of ions across the membrane and by the

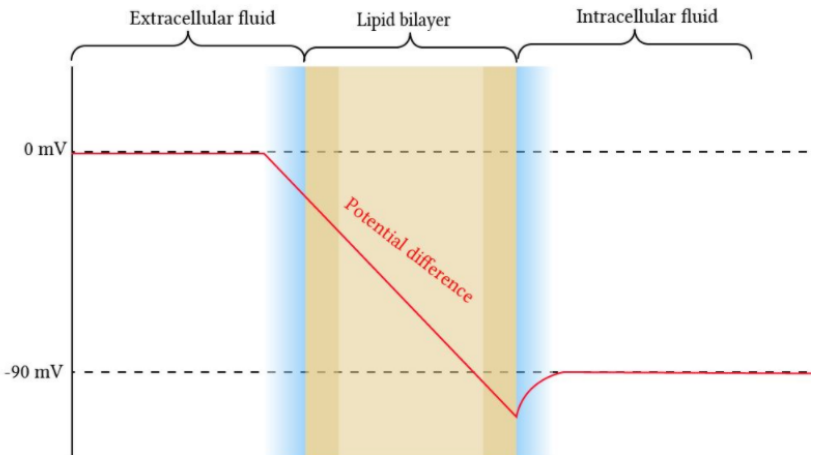

Fig. 2 Voltage drop across the cell membrane. The concentration differences of the ion charge carriers across the membrane lead to a potential difference between the intracellular and the extracellular environment. Image adapted from [12].

permeability of this membrane to each type of ion. The ion concentration difference is maintained by proteins known as active transporters. They move ions across the membrane by using the energy of the cell by metabolizing adenosine triphosphate or ATP. An example of such a transporter is the sodium-potassium pump that moves the ions against their concentration gradients where three sodium ions are extruded from and two potassium ions are imported into the cell per ATP molecule processed. This pump is the main supporter of the concentration gradients of Na+ and K+ across the membrane. Opposing the sodium-potassium pump, are passive leak channels, permeable only to certain kinds of ion allowing them to flow freely in the direction of their concentration gradients (see Fig.3). Thus, ion channels and active transporters work against each other to generate potential across the membrane. It is important to emphasize that the flow of ions will seemingly stop (the membrane potential is kept approximately constant) at the point where the electrical gradient created by the net flux of charged particles is equal and with opposite direction to the change in the concentration gradient.

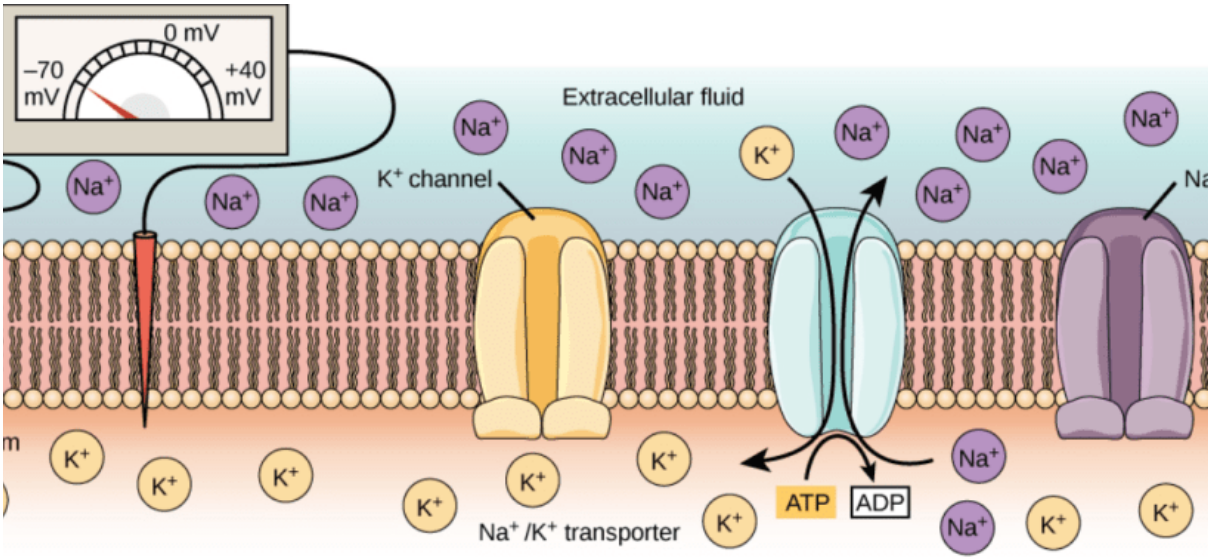

Fig. 3 Sodium-potassium pump and passive leak channels along the neuronal cell membrane. For each ATP molecule, the pump moves three sodium and two potassium ions in opposite directions, each against its concentration gradient. Passive channels are always open and ions pass through them continuously. Image adapted from [13].

This point is called the electrochemical equilibrium. The potential generated across the membrane for each ion species can be calculated using the Nernst equation and knowing the concentration of the ions X in and out of the cell:

$$E_x = \frac{RT}{zF} ln \frac{X_{out}}{X_{in}} = \frac{58}{z} log \frac{X_{out}}{X_{in}}$$

where E_x is the equilibrium potential, R is the gas constant, T is the absolute temperature in the Kelvin scale, z is the electrical charge of the ion, and F is Faraday's constant[14-16]. In order to describe the more complex situation of having a concentration of different ions with different permeability of the membrane for each ion species, a more elaborate equation was developed by Goldman, Hodgkin, and Katz in 1943. This equation is an extended version of the Nernst equation where the voltage across the membrane is expressed as:

$$V = 58log\ \frac{P_k\ [K+]_{out} + P_{Na}[Na+]_{out} + P_{Cl}[Cl-]_{in}}{P_k\ [K+]_{in} + P_{Na}[Na+]_{in} + P_{Cl}[Cl-]_{out}}$$

Here, P is the permeability, and in square brackets is the concentration for each ion. The reason why chloride concentrations are inverted in the equation (intracellular concentration in the numerator and extracellular in the denominator) is that the ions flow in the opposite direction of the two other ions across the membrane. Na/K pump and leak channels along the membrane keep the concentrations of ions constant and the membrane potential at approximately -70mV.

Additionally, there are voltage-gated ion channels along the membrane that can alternate the permeability to certain ions when the potential changes. Most importantly, some of these channels are responsible for the early influx of Na+ followed by a delayed efflux of K+ if the influx of Na+ ions is high enough to depolarize the membrane above a certain threshold. If the membrane reaches its threshold. it fires an AP. In mammalian neurons, more than a dozen voltage-dependent channels are expressed. Thus, providing a wide range of ways to encode information in the AP by generating different shapes, frequencies, and patterns [17].

Once an AP is fired, the proximal voltage-gated Na+ channel starts to open rapidly. The influx of sodium ions causes further depolarization of the membrane. During this phase of depolarization (see Fig.4) the inside of the cell becomes more positive and the potential reaches values close to the equilibrium potential for sodium ions and the channel starts to close. At this potential K+ channels start to open causing an efflux of potassium ions and repolarization of the membrane. This efflux continues until the phase of hyperpolarization is reached and the potassium channels are closed. This phase brings the membrane to more negative values but soon the RMP is restored, the neuron is ready to fire another AP. The phase of repolarization is also known as a refractory period during which the chances for triggering an AP are low because the difference between the actual membrane potential and the threshold potential is bigger than what it is during rest.

Following these phases of opening and closing of ion channels, AP propagates down the axon until it reaches its target. The areas of the membrane that were recently depolarized will not depolarize again because of the refractory period and therefore the AP can travel down the axon in one direction.

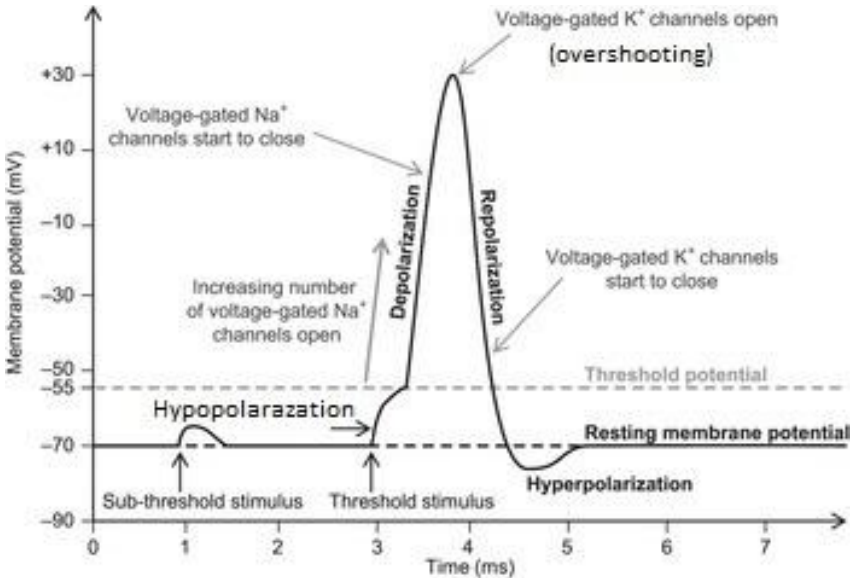

Fig. 4 Changes in membrane potential during typical AP. An action potential has several phases: hypopolarization, depolarization, overshoot, repolarization, and hyperpolarization. Hypopolarization is the initial increase of the membrane potential to the value of the threshold potential. The next phase is depolarization - a large influx of sodium ions. The overshoot value of the cell potential at the end of depolarization opens voltage-gated potassium channels, which causes a large potassium efflux and decrease of the potential, this is the repolarization phase. Repolarization leads to hyperpolarization, a state in which the membrane potential is more negative than the default membrane potential. Image adapted from [18].

2.1.4 Synaptic Transmission and Synaptic Plasticity

The neurons can communicate with up to 100 000 other neurons. An efficient mechanism of transduction of the signal from one cell to another is provided by the functional contacts between them called synapses. There are electrical synapses - a mechanical and electrically conductive link between two neighboring neurons that is formed at a narrow gap between the pre- and postsynaptic neurons known as a gap junction, and chemical synapses that secrete neurotransmitters - chemical agents that are released from the presynaptic neuron to bind to receptors on the postsynaptic neuron and ultimately inhibit or excite the cell. Inhibition refers to lowering the chances for firing AP while excitation - to raising them. The neurotransmitter receptors can be ionotropic - the neurotransmitter binds directly to ligand-gated ion channels, or metabotropic where the receptors do not have channels but instead, an intracellular domain know as G-protein that directly affects ion channels [19, 20]. The neurotransmitter molecules in the presynaptic neuron are packed into two types of vesicles - small clear-core vesicles containing small neurotransmitter molecules and large dense-core vesicles containing peptide neurotransmitters, some of which acts also as hormones. When an AP arrives at the presynaptic terminal the depolarization of the membrane causes opening of voltage-gated

Ca2+ channels. The influx of Ca2+ then triggers exocytosis - a fusion of the vesicles with the presynaptic membrane and the release of the neurotransmitter molecules (see Fig.5). Synaptotagmin and complexin are proteins activated by Ca2+ ions that bind to assembled SNARE protein complexes. SNARE and SM proteins undergo cycles of assembly and disassembly to bridge the gap between the membranes and fuse them[20,21]. The released molecules diffuse through the synaptic cleft to reach the postsynaptic neuron. The transmitter then binds to receptors effectively opening or closing postsynaptic channels. After the molecule is released from the receptors it undergoes enzymatic degradation or glial metabolite recycling [22-24].

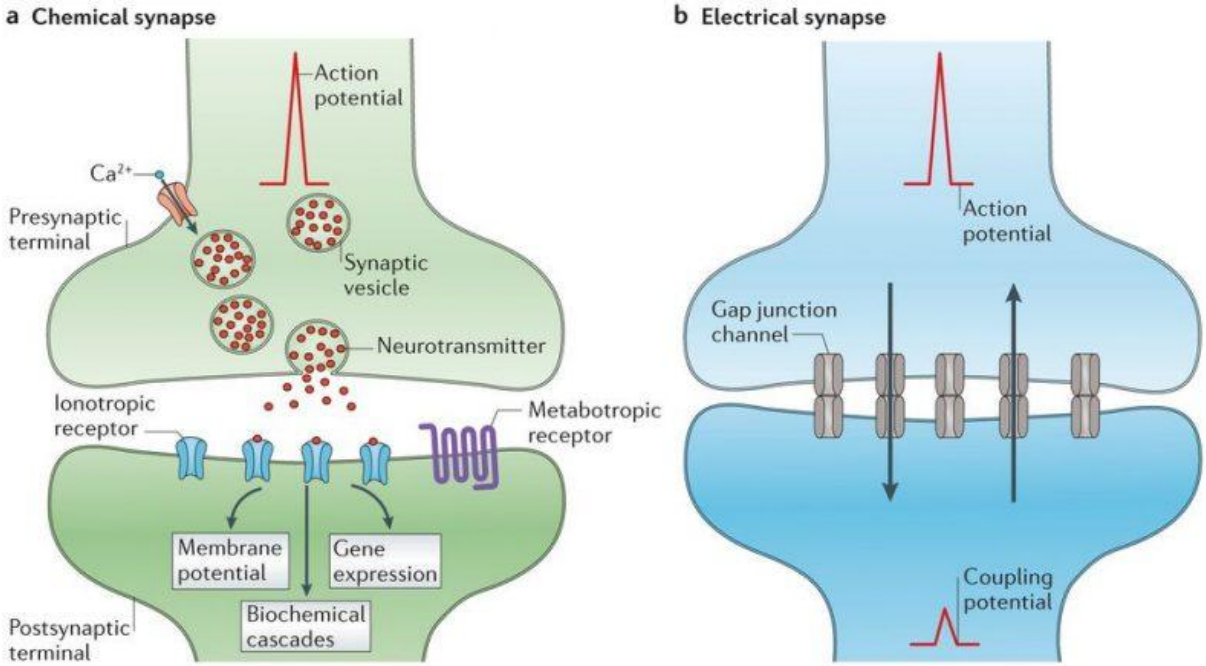

Fig. 5 The two main modalities of synaptic transmission. Chemical transmission requires sophisticated presynaptic molecular machinery that regulates the neurotransmitter release upon depolarization of the presynaptic terminal. Electrical transmission is mediated by clusters of intercellular channels called gap junctions that connect the interior of two adjacent cells. Electrical synapses are bidirectional in nature and enable the passage of electrical currents carried by ions. Image adapted from [25].

In general, the postsynaptic conductance changes after binding of the transmitter to the postsynaptic receptors causing a flow of ions. This postsynaptic current or PSC alters the membrane potential producing a postsynaptic potential or PSP. The potential at which a given neurotransmitter causes no net current flow of ions through that neurotransmitter receptor´s ion channel is called reverse potential. The reversal potential depends on the concentration of ions in and out of the cell. Its value compared to the threshold for AP of the neuron determines whether a PSP is excitatory (EPSP) or inhibitory (IPSP). In the case of EPSP the reversal potential is more positive than the threshold for AP, the cell depolarizes and the chance for firing is higher. It is possible, however, for the PSP to depolarize the neuron but

still act as an IPSP. If the reversal potential is lower than the threshold but higher than the normal resting membrane potential, the cell will depolarize but the PSP will still act inhibitory by keeping the potential under the AP threshold. It is also possible for inhibitory transmitters such as GABA to act excitatory when the concentration and permeability of ions change the reversal potential for chloride [26,27]. A shift in the reversal potential of GABA-mediated signaling through Cl- channels are found to correlate with the occurrence of epilepsies, autism spectrum disorders, and other developmental disorders. Drugs that target the Cl- ions concentration in GABAergic neurons can therefore be considered as potential therapeutic applicants for these disorders [28].

The PSPs of individual synapses in the brain are much smaller than the threshold for AP. Most neurons have on average thousands of synaptic connections with other neurons and the PSPs produced at any given moment sum together to determine whether the cell will fire or not. This dendritic integration of EPSPs and IPSPs is essential for the high computational degree of freedom that neurons exhibit. The summation of individual PSPs ultimately determines the somatic membrane potential and the neuronal spiking pattern. The information processing abilities of the cells then are highly dependent on their degree of convergence and divergence. In most simplified models the algebraic sum of EPSPs and IPSPs is used to determine the overall effect of summation. These linear and some non-linear summations are examined in various papers [29-33]. Different models are necessary to describe summation in different types of neurons but as a general rule, the summed response at the soma is equal to the algebraic sum of EPSPs, IPSPs, and a nonlinear term that is proportional to the amplitudes of both EPSPs and IPSPs [30]. The morphology of the cell together with the neurotransmitters and receptors involved in the signal transduction are important parameters to be considered when modeling the expression of this nonlinear term.

The synaptic connections between neurons are dynamic entities. New connections can form and previously established connections can either weaken or strengthen their contacts under the influence of neural activity. This ability of the synapses to respond to changes is known as synaptic plasticity. These processes of adaptation are more active in the developmental stages of the immature brain but also play an important role in learning and memory in adults [34,35]. Evidence in support of this is when the resulting damage of early occurring brain injury is often attenuated relative to later occurring injuries. The neurite projections between neurons in the developing brain are much more than the one in an already developed brain and this allows for cortical areas distant from the injury to undergo major neuroanatomical reorganization in order to partially restore certain functions [36]. The synaptic plasticity leads to both structural and functional changes in the cells. While some life experiences influence anatomical changes in the neurons (volumetric differences in the morphometry of particular brain regions), others can change the firing pattern of the cell by biochemical regulatory mechanisms.

Synaptic plasticity is a change in the process of signal transmission and can occur in different forms. They can be separated into two main categories: short-term and long-term plasticity. There are a few forms of short-term synaptic plasticity that enhance neurotransmitter release.

These are facilitation, augmentation, and potentiation. They involve metabolic processes dependent on Ca2+ ions concentrations and their effect on neurotransmitter release. Synaptic facilitation is an increase in the strength of contact when two or more APs arrive at the cell within a few milliseconds interval. The first AP triggers an influx of Ca2+ ions as part of the signal transduction cascades involved in the vesicle release. Because the mechanism of returning the presynaptic neuron back to resting levels of Ca2+ is slower than a few milliseconds, another AP arriving in this interval will bring the Ca2+ levels to higher concentrations compared to the case of only one AP. The rate of building up the calcium levels is therefore related to the firing frequency of the synapse. More Ca2+ ions available in the presynaptic terminal facilitate the release of neurotransmitter vesicles by subsequent AP. Augmentation and potentiation also enhance the amount of neurotransmitters released from the cell in case of repeating synaptic activity but they act in different time scales. Augmentation occurs in the interval of a few seconds, while potentiation can last up to a few minutes. The mechanism of these forms of short-term plasticity is not completely understood but it is known that Ca2+ ions interact with proteins and activate protein kinases that are involved in the membrane fusion of the vesicles [37-39]. Another form of short-term plasticity is synaptic depression. When the synaptic activity is sustained over time the reserves of available vesicles are depleted. This decreases the strength of signal transmission while new vesicles become available from one of three pools - the readily releasable pool, the recycling pool, and the reserve pool [40, 41]. The duration of synaptic depression is determined by the rate of supply with vesicles from these pools. All forms of short-term plasticity interact together to cause complex changes in the synaptic transmission. These changes can dramatically alter the processing of information from the neurons leading to functional adaptations.

Long-term plasticity refers to the alternation of the synaptic transmission for time scales from over 30 minutes up to a lifetime. Different molecular mechanisms contribute to these long-lasting changes. Posttranslational modifications of proteins modulate the trafficking of glutamate receptors and this mechanism is responsible for the initial changes in the transmission. If it is sustained over time it will lead to changes in the gene expression of the cell which can cause a permanent alteration of brain functions. Donald Hebb is the first one to bring the attention of neuroscientists to neuroplasticity and its importance in learning and behavior [42]. When two neurons fire together they strengthen their connections and this is called long-term synaptic potentiation or LTP. When the neurons repeatedly fire in an uncoordinated manner, the connection between them weakens and this is called long-term depression or LTD. The degree of voltage change in the postsynaptic neuron determines whether a signal is weakened or strengthened. In LTP the voltage change increases compared to previous signals and in LTP - decreases. The most important parameter of the process of signal transmission, in this case, is the time interval between the firing of the neurons. The critical period is found to be 20ms [43-45] but some papers argue that this is not extensively valid [46]. Cells that fire together below 20ms apart undergo LTP, if the firing is more than 20ms apart LTD occurs. This is also called spike-timing-dependent plasticity. The most studied example of this type of synaptic plasticity is in glutamate active hippocampal neurons. Glutamate receptors and their generation is the main mechanism involved in LTP

and LTD. There are two glutamate receptors that are particularly important - AMPA and NMDA receptors. The AMPA receptor is permeable to sodium and potassium and depolarizes the cell when it is open. The NMDA receptor is blocked by Mg2+ ions at negative voltages. When the neuron is depolarized, the magnesium ion is displaced and the NMDA receptor opens. Sodium ions enter the cell and potassium ions leave the cell, contributing to further depolarization. Together with the Na+ ions, Ca2+ ions also enter the cell. It is this calcium ion current that causes spike timing-dependent plasticity to occur. When the two neurons fire together in the interval of 20ms the AMPA receptors activated by glutamate cause depolarization and opening of NMDA receptors. This leads to a large influx of Ca2+ ions. When the cells fire more than 20ms apart the postsynaptic neuron is in process of repolarization when another signal arrives. This repolarization causes fewer NMDA channels to be available for opening, leading to a smaller influx of Ca2+. Large calcium influx triggers LTP and more moderate calcium influx - LTD. In the cell, new AMPA receptors are constantly recycled. The new receptors undergo exocytosis and migrate to the postsynaptic areas while receptors from this area migrate to undergo endocytosis. The inside of the cell contains pools of AMPA receptors. When the calcium influx is large enough it triggers a cascade of kinases. These kinases alter the recycling of AMPA receptors by increasing the rate of exocytosis. They also alter the receptors, making them more permeable. This means more receptors with higher efficiency are available to detect signals, or LTP occurs. When the levels of calcium influx are lower, the threshold for triggering kinases is not reached. A protein phosphatase in this case is triggered from the Ca2+ that also alters the recycling of AMPA. The phosphatases increase the rate of endocytosis leading to fewer receptors available at the postsynaptic site. Decreasing the number of receptors leads to smaller voltage changes in the postsynaptic terminal, generating LTD[47].

During the repetitive synaptic activity, all forms of plasticity interact together to change the transmission in complex ways. Besides the spike timing dependence, the morphology of the cells, their chemical balance, and surrounding are also important parameters to be taken into consideration when the mechanisms of plasticity are studied and computationally modeled.

2.1.5 Structural and Functional Disorders of the CNS

The incredible complexity of the levels of organization in the human brain ultimately gives rise to all cognitive functions. This happens through the integration of multiple, spatially distributed neural systems. Thus, pathological perturbations in one part of the brain will have an effect on another. These perturbations most often spread via axonal pathways. The propagation, however, is hard to model due to the incredible complexity of the mechanisms involved in axonal transport: from different molecular motors using the cellular cytoskeleton as a highway to a long but not finished list of genes regulating all aspects of the transportation [48-52]. It is hypothesized that disruptions in the normal regime of axonal transport are one of the main reasons for the development of neurological disorders such as Alzheimer's disease (AD), Amyotrophic lateral sclerosis (ALS), and Parkinson's disease

(PD) [49,51,52]. To understand and model the progression of such diseases is important to have knowledge of the topology of the underlying neural architecture, also called a connectome. The connectome is a map of the neural connections in the brain and allows to model the propagation of diseases and injuries across the brain [50]. Recently, models implementing AI are used to predict the early development of diseases and treatment responses based on connectomic approaches [53-55]. The use of MEA platforms is essential for such studies.

The disorders of the CNS can be summarised in a few categories: structural disorders, functional disorders, vascular disorders, infections, and degeneration.

1. Vascular disorders are a malfunction of the blood vessels that can affect the brain by altering the blood flow and ultimately, the oxygen and nutrition supply. Examples of brain disease caused by vascular disorder are stroke, transient ischemic attack (TIA), subarachnoid hemorrhage, subdural hemorrhage and hematoma, and extradural hemorrhage.

2. Infections of the CNS can be caused by bacteria, viruses, or fungi. They can be life-threatening especially for children and require intensive health care. Most common infections of the brain include meningitis, encephalitis, polio, and epidural abscess. Therapies for CNS infections are difficult to establish due to changing microbial resistance patterns. Understanding the mechanism of cerebral inflammation and the evolving microbial epidemiology is important for optimizing therapies in patients with meningitis, for example. Selective immunomodulation, molecular diagnostics, and preventive strategies seem to be the key in the management of CNS infections [61].

3. In degenerative diseases, the cells of the CNS experience a progressive loss of structure or function and even death due to chronic inflammation. Some of the factors that drive chronic inflammation include misfolded and aggregated proteins. Recently, inhibition of the processes that produce these amyloidogenic proteins by phenolic compounds is reported in research models in vitro but they still have no success in vivo [68].

   Some of the most common neurodegenerative diseases include PD, AD, ALS, multiple sclerosis, and Huntington's disease. Since the adult brain has limited abilities of neuroregeneration, the dead cells are not replaced and this permanent loss of function is irreversible. With aging, the immune cells of the brain, macrophages, and microglia, display impaired phagocytosis which results in increased toxic protein accumulation - the amyloidogenic proteins, which are associated with progressive pathology of Aβ in AD and α‑synuclein in PD[64]. Some successful immune therapies for neuroinflammatory disorders include the intervention of cannabinoids. They attenuate the excitotoxic glutamatergic neurotransmission and modulate the metabolism of microglia and astrocytes[65-67]. The efforts of clinicians are therefore

directed towards prevention but there are a few strategies that can potentially become a successful treatment. Between them are: 1) antagonizing the cytotoxic causal events [56]; 2) stimulating endogenous protective processes [57,58], and 3) promoting structural repair with the use of grafts [59] and stem cell transplants [60].

4. Functional neurological disorders (FND) are a form of psychogenic illness that can be triggered by a response to physical or psychological trauma. The normal functioning of the brain is alternated without the occurrence of detectable structural damages. That makes this type of disorder difficult to detect. The symptoms include muscle weakness, loss of balance, abnormal movement, paralysis, disruptions in sensory signals, or loss of consciousness. The conditions are disabling for the patients but in many cases reversible. The treatment depends on the type of the disorder and can be either psychological interventions in form of behavioral therapies or physiological strategies for rehabilitation [62]. In some cases of FND psychedelic drugs as LSD (lysergic acid diethylamide) and psilocybin are found to have promising effects on patients through activating alternative pathways of aberrant neural self-representation [58].

5. Structural damage of neurons can occur either in CNS or in the peripheral nervous system. In CNS most of the damaged cells do not regenerate due to slow debris clearance, astroglial scarring, and intrinsic growth capacity. However, it is shown in a few studies [69-72] that the CNS neurons retain the capacity to regenerate when provided with an appropriate peripheral nerve graft [73]. This suggests the presence of inhibitory growth factors in CNS. The most important of them is NogoA which is a membrane protein present on oligodendrocytes and chondroitin sulfate proteoglycans (CSPGs) that are produced mainly by glia [74]. Neutralization of these inhibitory growth factors promotes axonal restoration. The concentrations of proteins and enzymes, such as S-100 protein, neuron-specific enolase (NSE), creatinine phosphokinase isoenzyme BB (CPK-BB), and myelin basic protein (MBP) can be used as biochemical markers to assess the extent of the injury and for the prediction of a long-term outcome.

   The peripheral nervous system consists of all nerves and ganglia outside the brain and the spinal cord. This system carries out the connection between the CNS and the limbs and organs. In contrast with the brain and the spinal cord the spinal nerves do not have protective bone formations or blood-brain barrier (BBB) and are therefore more vulnerable to mechanical damage and toxin poisoning. However, the nerves are surrounded by a protective layer of connective tissue, primarily made from collagen, called epineurium (see Fig.6). This sheath surrounds all fascicles, an organized bundle of neurons, and blood vessels present in the nerve. The fascicles also have a protective layer of tissue called the perineurium. The perineurium cells are epithelioid myofibroblasts and exhibit a chemical barrier selectivity that protects the underlying neurons. The neurons enclosed by the perineurium in a single fascicle can be myelinated or unmyelinated. The myelinated neurons are enclosed in yet another

protective layer called endoneurium [75]. The endoneurium contains the nerve fibers and endoneurial liquid that plays an important role in regeneration after injury. The homeostasis of endoneurial cells is very important for the function of the blood-nerve barrier (BNB). BNB controls ion, solute, water, nutrient, macromolecule, and leukocyte influx and efflux between the bloodstream and endoneurium [76].

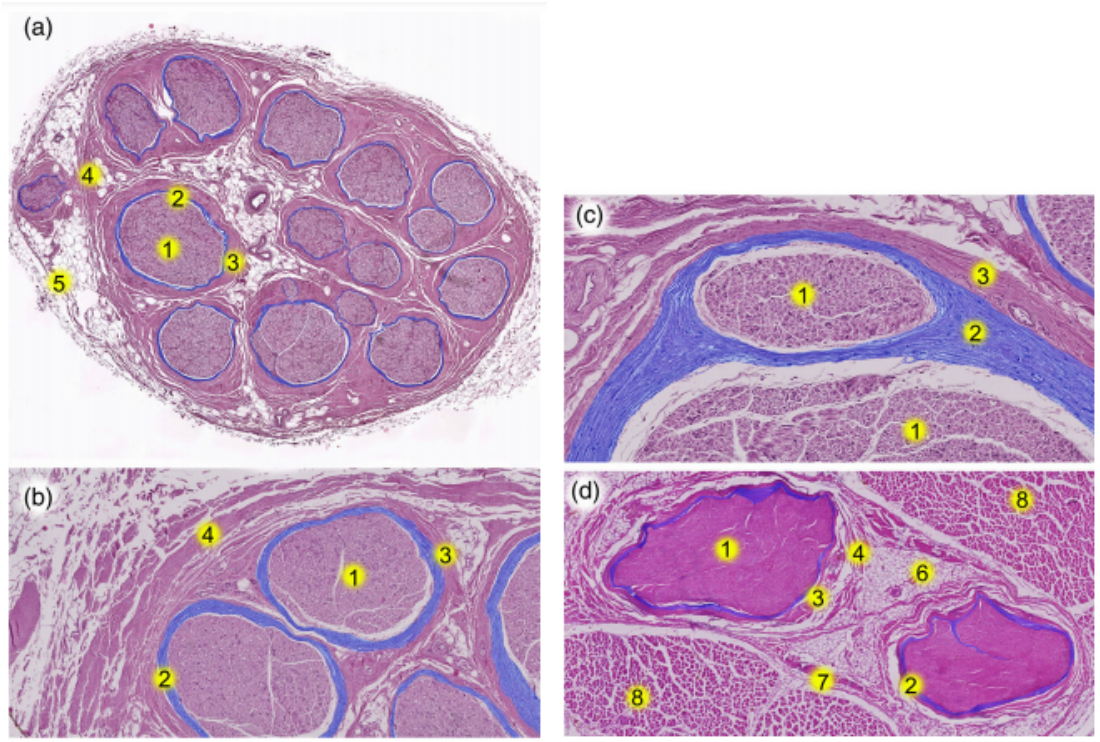

Fig. 6 Full cross-section of a human median nerve: 1 = axons in endoneurium, 2 = perineurium, 3 = internal epineurium, 4 = epineurium, 5 = circumneurium; 6 = fat compartment, 7 = epimysium, 8 = muscle, [70]. Magnification: (a) x40, (b) x120, (c) x300, (d) x40. Image adopted from [77].

The peripheral nerve injury (PNI) can be separated into three types of disorders - neuropraxia, axonotmesis, and neurotmesis. The least severe is neuropraxia, a reversible condition when the axon and the surrounding endoneurium fall under compression. This disrupts the myelination of the axon and therefore the signal transduction. In axonotmesis, the endoneurium is still intact but a segment loss along the axon can be observed. Regeneration of the axon is possible in this case since the endoneurium layer enclosed around the cell serves as a guide for the direction of the axon growth and supports appropriate growth factor concentrations within the endoneurial fluid by secreting serotonin and histamine. The distal end of the neuron undergoes degeneration also called Wallerian degeneration. The proximal part of the axon undergoes degeneration till the next node of Ranvier, after which the axon starts the regeneration process and reaches to connect in most cases to other neurons due to obstruction of extensive scar tissue, leaving the patients with little to no return of the function

[78]. The third type of PNI, neurotmesis, refer to the case of axon loss plus one of the following:

1) disruption of the endoneurium - still a possibility for fair regrowth
2) disruption of the perineurium - poor regrowth
3) disruption of the epineurium - no regrowth

A few successful therapies for recovery after PNI exist. Among them are electrostimulation, phototherapy, and ultrasound. Low-intensity electrostimulation (20 Hz or less) applied for 30 min to 1 h facilitates and promotes nerve regeneration. These results are reported in several studies [78-80]. Phototherapy is a promising method that uses low-power radiation to promote regrowth and axonal regeneration. Reduced scar tissue formation, fewer degenerative phenomena, and a significant increase in axonal growth and myelination are among the observable effects [81]. The applied electromagnetic stimulation promotes the synthesis of ATP, cell proliferation, and the expression of neurotrophic factors. This increases the available energy in the axons supporting faster nerve regeneration [78].

2.2 Electrophysiology

Electrophysiology is a discipline that studies the electrical properties of cells and biological tissues. It is the branch of physiology that pertains broadly to the flow of ions and particularly to the electrical recording techniques that enable the measurement of this flow. It finds applications in both clinical and research activities such as testing for nervous and cardiac diseases and abnormalities, or investigation of the electrical properties of cell membranes with a focus on the ion concentrations inside and outside the cell. Neuronal electrophysiology focuses on the properties of biological cells and tissues in the nervous system. Changes in these properties allow the nervous system to support its elaborate network of functions, which is responsible for keeping us alive and also allows us to achieve higher levels of consciousness. Studying these properties has many implications beyond the basic understanding of how the brain works, including investigations of neurological disorders and the potential uses or effects of pharmaceutical compounds. MEAs are widely used to perform electrophysiological experiments on tissue slices or dissociated cell cultures to understand different aspects of the aforementioned properties which make this type of device a valuable tool in the tool-kits of many neuroscience laboratories.

There are two categories of methods used in electrophysiology - intracellular and extracellular. Intracellular electrophysiological recordings obtain information from one single cell while extracellular recordings involve obtaining conductivity and impulse information from a group of cells. Three techniques are widely used in intracellular electrophysiology. They are current clamping, voltage clamping, and patch clamping. In the current clamping technique, a known current is applied to the cell and the change in the membrane potential is then measured. In voltage clamping, a sustained voltage is applied to the sample, initiating an

ion flow due to potential changes. A feedback loop is then used to maintain the voltage. In the patch clamping technique, a micropipette is used to attach to the cell of interest and measure the electrical properties. The cell is punctured and a small amount of the membrane is sucked inside, forming a seal. This technique studies the ion flow and the cell membrane potential.

Another technique that has been adopted in the field of electrophysiology is optogenetics. Modern optogenetics enables temporally precise excitatory or inhibitory modulation of neural and cardiac activity [82,83]. This process involves the use of light to control the activation of a cell, most commonly neurons, that have been genetically modified to express specific light-sensitive ion channels. Examples of optogenetic actuators for neural modulation are channelrhodopsin, halorhodopsin, and archaerhodopsin [84,85]. Cardiac optogenetics is an emerging field that finds application in cardiotoxicity, pacemaking, and defibrillation [86,87].

Wireless devices for electrophysiology are emerging tools that introduce new possibilities for applications in preclinical research. Such devices are modern computer-brain interfaces that enable dynamic screening and stimulation of freely moving subjects [88.89]. The combination of simultaneous multichannel recording site and optogenetic stimulation allows for new insights into real-time data separation and analysis of the activity of the brain.

2.2.1 Modeling of Neural Electrophysiology

With the extensive use of in-vitro models for neuroscientific investigations and the growing field of network electrophysiology, many studies on cultured cells are performed to better understand the neurophysiological mechanisms and computational properties of such cultures. The use of MEAs is a substantial part of such studies as they provide the basis for analysis of the behavior of neural populations *in vitro*. Neural models can be constructed at different levels of abstraction. Mathematical modeling and computer simulation techniques have become essential tools in understanding diverse aspects of neural processing.

In computational and biophysical neuroscience, to understand and interpret the gathered data from neural recordings it is useful to simplify the neuron to a degree where the general functions and behavior are preserved. The level of complexity of such models can vary according to the questions that try to answer. When dealing with a large network of neurons, the separate cells are often represented by a single compartment or so-called point model of a neuron, where both the soma and the neurites are considered a point in the network. This model is useful when one investigates signaling trends and cascades in complex networks rather than focusing on the individual traits of the neurons which affect the signal locally. Reducing the complexity of the system in this way makes it easier for further computational analysis[90].

More complex models are necessary when one wants to model the real-time processing and interactions in neurological networks, including embedded bio-compatible electronic devices. For this purpose, a more elaborate representation of the soma and the neurites is required. In many cases, it is useful to represent the soma by a sphere and the axons and dendrites - by cylinders. These models are named multicompartment models or stick-and-ball models. Such models are also used in building neuromorphic electronic devices [91] and investigating the intrinsic dynamics of different types of neurons [92]. Each of the compartments is then described by an electrical element with common electrical properties or a so-called electrical equivalent circuit. This method of representation serves as a bridge between biology and physics enabling the use of mathematical equations to describe the process of signal propagation in biological tissues [93].

2.2.2 Cable Theory

One of the most widely used classical models describing the propagation of spread current in neurites is the cable theory. Many neurons have either a complex geometry, or large spatial extent, or both. The spatial extent of the neurites provides difficulties in modeling the propagation. On the other hand, the fact that synaptic inputs are collected far away from the soma leads to inherent difficulty. When they arrive at the soma, they will be filtered and attenuated. In Fig. 7, the voltage attenuation in dendrite as a function of time at 3 distances from the current injection is presented. The current that is seen at the soma will then be different from the current provided at the site of the synapse. The current that arrives at the soma is usually smaller and with a different shape than the one injected at the site of transduction and is highly dependent on the distance from the current injection [94].

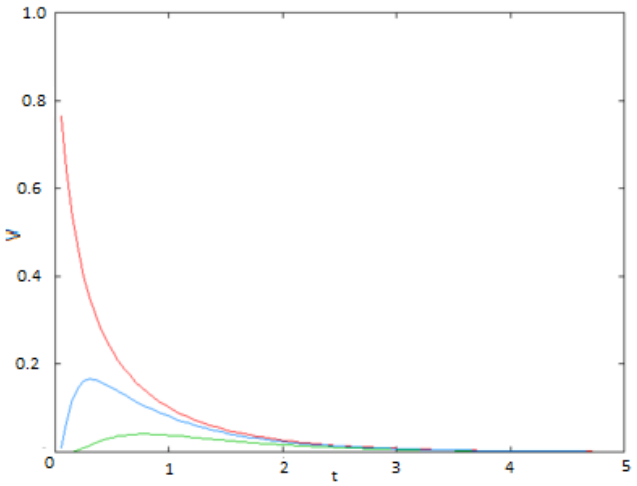

Fig. 7 Voltage as a function of time in response to a fast current injection at three different distances x from the location of injection: Red: x=0.3, Blue: x=1, Green: x=2. While very close to the current injection (red trace) the voltage rises strongly and rapidly, the voltage rise is less pronounced and also delayed further away (blue trace) and even more so for larger distances (green trace). Image adapted from [94].

In the case of a complex dendritic tree, as for Purkinje cells, the neurons receive large numbers of inputs that can reach up to tens of thousands. These inputs can interact in a highly nonlinear way during their propagation across the dendritic three which goes beyond the simple summation of the impulses, thus allowing for so-called dendritic computations. It is difficult to measure and control these distal inputs with the methods of electrophysiology and this is the reason why we know so little about how the dendrites integrate their synaptic inputs. One of the most important implications of cable theory is its ability to describe quantitatively how neurons integrate these inputs.

In cable theory, the neurites are represented as cylinders which are further divided into infinitesimal small patches, each with its intrinsic capacitance and resistance (see Fig. 8). A crucial assumption in cable theory is to remove the morphological complexity of the neuron and to describe the current propagation as if it travels through a long, thin cylinder. In this case, the voltage will vary a lot more along the long axis of the cylinder rather than along the perpendicular to this direction which is also the direction of propagation. Then the small variation in the voltage can be neglected and only the one parallel to the direction of propagation can be taken into consideration. This simplification has the advantage of reducing the computational requirements for modeling from three dimensions to one.

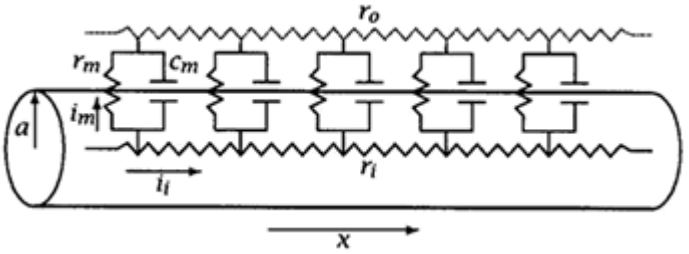

Fig. 8 Illustration of the electrical equivalent circuit used to describe cable theory. r_i *represents the internal resistance of the cytoplasm,* r_m *represents the resistance across the membrane,* c_m *is the capacitance across the membrane,* i_m *is the current flow through the membrane,* r_i *is the resistance of the neurite, and* r_0 *is the resistance of the extracellular environment. Image adapted from [95].*

The membrane is an electrical insulator separating opposing charges inside and outside the cell. To account for the insulating properties of the lipid bilayer of the cellular membrane, capacitor elements c_m, together with their resistance r_m, are used to model the dynamic processes during APs. These elements are represented in Fig. 8. Each patch of the membrane is then modeled as an RC circuit. The most important outcome of cable theory is the cable equation given by:

$$\tau_m \frac{\partial(x,t)}{\partial t} = \lambda^2 \frac{\partial^2 V_m(x,t)}{d\partial} - (V_m(x,t) - E_m)$$

, where τ_m is the time necessary for the current to decay, λ is the spatial spread of the current. Derivations of the equation can be found at [94] and [96]. The cable equation is derived from the aforementioned circuit model of the membrane and its intracellular and extracellular space. It can provide a quantitative description of current flow and voltage change both within and between neurons, allowing us to understand how they function and giving the base to model neural recordings which is discussed in the next sections.

2.2.3 Extracellular recordings

The transmembrane currents that occur in the neurons during neuronal activity give rise to local field potentials or LFP that can be measured in the extracellular medium. The synaptic transmembrane current is the main source of the extracellular signals. Na+ and Ca2+ spikes and ionic fluxes through the voltage- and ligand-gated channels also contribute to the shape of the measured signal. With the use of processing tools and computational modeling, extracellular recordings are a powerful method for revealing the cooperative behavior of neurons and their input and output activity dependencies.

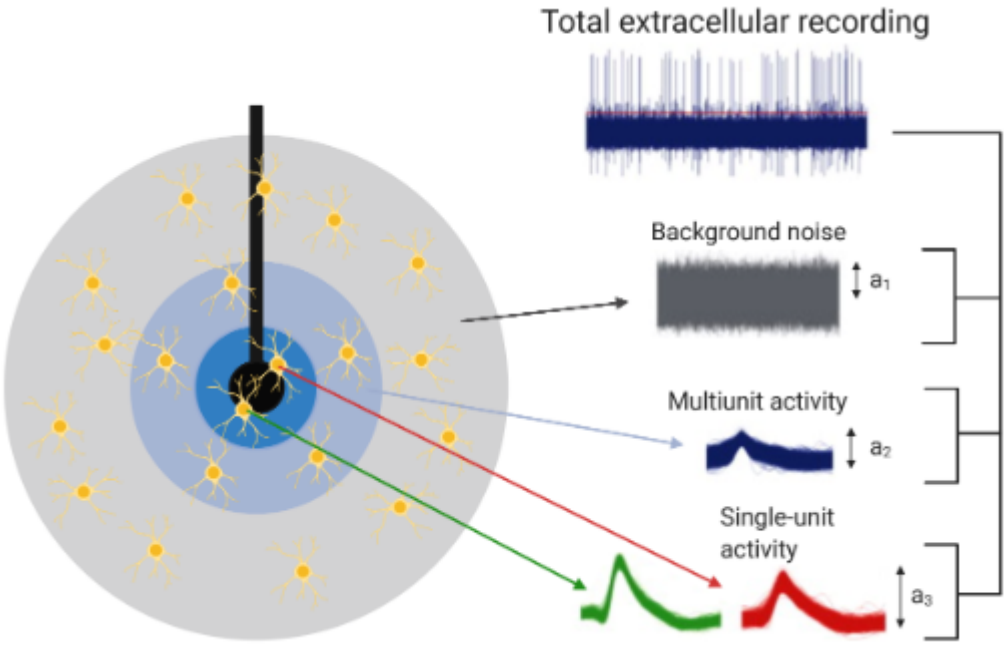

Fig. 9 The illustration shows typical extracellular recordings and sorting the signals by their proximity to the recording electrode. The amplitude a_1 shows the background noise, the overall activity is smeared out by the activity of the other cells and it is not traceable to individual neurons. The amplitude a_2 shows the multiunit activity near the electrode, spikes can be distinguished. Single-unit activity recordings occur from single neurons in the proximity of the electrode and have a distinguishable shape allowing for both spatial and temporal resolution of single-cell recordings, amplitude a_3. Image adapted from [98].

The LFP is a superposition of all ionic processes that occur in the proximity of the point of measurement. This includes any type of transmembrane current and any part of the excitable membrane of the neuron - a spine, dendrite, axon, or the soma. Besides the fast propagation of AP, the slower processes of glial metabolic-triggered ionic fluctuations also contribute to the strength of the extracellular field. The main characteristics of the LFP waveform - amplitude and frequency, thus depend on the degree of contribution from different sources and the properties of the medium in which the signal propagates. The distance from the firing cell to the recording electrode is deterministic for the shape and the amplitude of the signal. The amplitude of the recorded potential change scales with the inverse of the distance *r* between the source and the recording site (see Fig. 9)[97-101].

2.2.4 Volume conduction

Volume conduction theory describes the transmission of electric and magnetic fields from the primary current source through biological tissue to the recording electrode. When the frequency of the signal is below 1000 Hz (typical for APs) the capacitive component of the tissue impedance, the inductive and the electromagnetic propagation effects can be neglected and the transmission can be described by quasi-static Maxwell equations [102-104]. In the volume conduction theory, the neurites are represented as a one-dimensional cable that consists of a conductive core. The conductive core is the intracellular fluid with an ionic current flow creating ohmic conductance. The propagation of the signal along the neurites creates an ion exchange in the extracellular media that leads to charge imbalance which in turn gives rise to an extracellular potential (EP). The volume conductor representation depends on the distribution of the conductivity of the tissues or media that separate the current flow creating ohmic conductance. The propagation of the signal along the neurites creates an ion exchange in the extracellular media that leads to charge imbalance which in turn gives rise to an extracellular potential (EP). The volume conductor representation depends on the distribution of the conductivity of the tissues or media that separate the membrane currents from the extracellular recording site. In theory, the neurons can be in direct contact with the electrode but in most cases, there are extracellular proteins that prevent the cell from direct binding. These proteins are highly resistive and attenuate the signal from the cells. The shape, size, and distance of the electrode to the current source determine the strength of the signal [105]. In Fig. 10 a graph shows the dependence of the recorded spike amplitude plotted versus the distance from the electrode for different diameters of the electrode. It is apparent that smaller electrodes record higher amplitude, thus making the sorting of spikes easier. However, decreasing the area of the electrode increases the impedance which in turn decreases the signal-to-noise ratio (SNR) obscuring the detection of spikes. A method of increasing the effective area of the electrode, such as electrodeposition of porous platinum coatings is a possible solution to this problem.

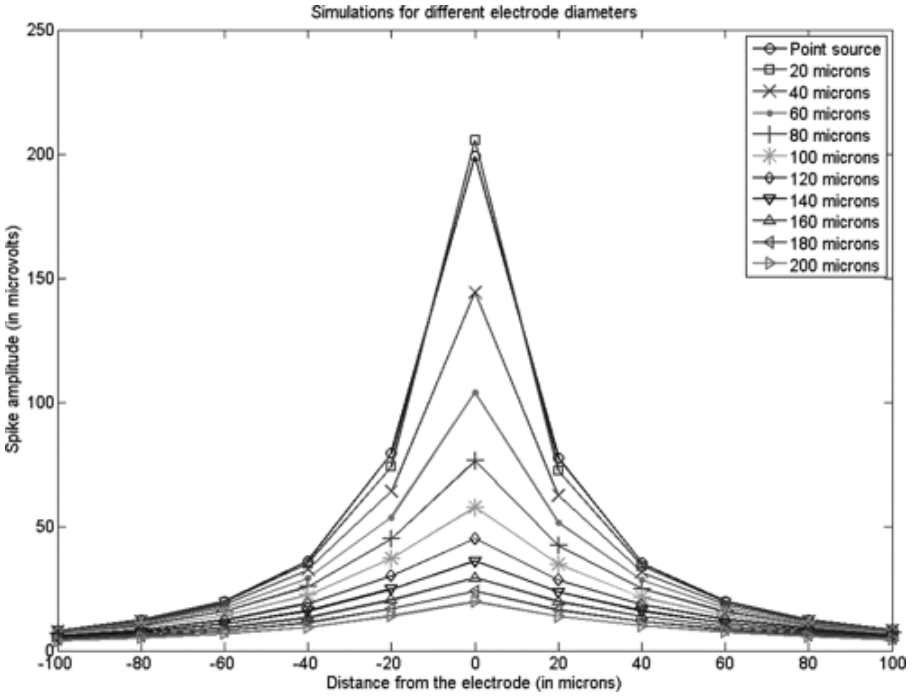

Fig. 10 The graph shows a plot of the amplitude of APs in microvolts versus the distance of the source to the electrode in microns for different sizes of the electrode. As shown, the amplitude of the spikes is higher for smaller electrodes and dissipates with the distance in a predictive manner. Best spike sorting properties will exhibit small electrodes in the near proximity to the neuron (up to 20um). Image adapted from [105].

electrical behavior of the system by quantitative evaluation of the conductance and the resistance of the elements. The elements, in this case, are the neuron, the electrolyte solution, and the electrode. The equivalent electrical circuit of a neuron is first described by Hodgkin and Huxley [106], 1952. The interface between neurons and microelectrode recordings in vitro has been first described as an electrical circuit in [107], 1968. Later, in 1996, a representation of the point-contact model was proposed by Weiss and Fromherz and is shown in Fig. 11a. Since then, different models are proposed to account for the distance between the neuron and electrode, including volume conduction theory[108-110], area-contact model [111], and others [112-114]. In Fig. 11b, a generalized model of the electrical circuit of a neuron and recording site is shown. This model is applicable for tissue slices and neural populations.

In the point-contact model in Fig. 11a, the capacitance of the lipid bilayer of the membrane is represented by c_m. The conductances of the potassium and sodium ion channels are g_k and g_{Na}, g_l is the leak conductance. E_k, E_{Na}, and E_l are the reversal potentials for potassium, sodium, and leak channels, respectively. R_{gap} and R_{seal} account for the resistance of the gap

between the neuron and the electrode, and for the resistance of the electrolyte to spread currents. The shape of the recorded signal for intracellular and extracellular APs is also shown. The influx of sodium ions causes a positive rise of the potential measured inside the cell, while the depletion of the same ions outside the cell is detected by the electrode as a negative spike. Modeling the electrical properties of the neuron-electrode system helps to understand the signals recorded by the microelectrode arrays (MEAs). The detected voltage is shaped by the electrical characteristics of the medium through which the signal travels.

The equivalent electrical circuit shown in Fig. 11b is separated into two parts. This is possible due to the assumption that the MEAs act as an insulator (does not contribute to the ionic exchange between the neuron and the electrolyte) with higher input impedance that prevents any effect from the electrode on the potential at the neuron site. The upper part, so-called fluid side, is represented by a voltage source while the lower, metal side, is represented by circuit elements describing the electrode-electrolyte interface by separating the effective

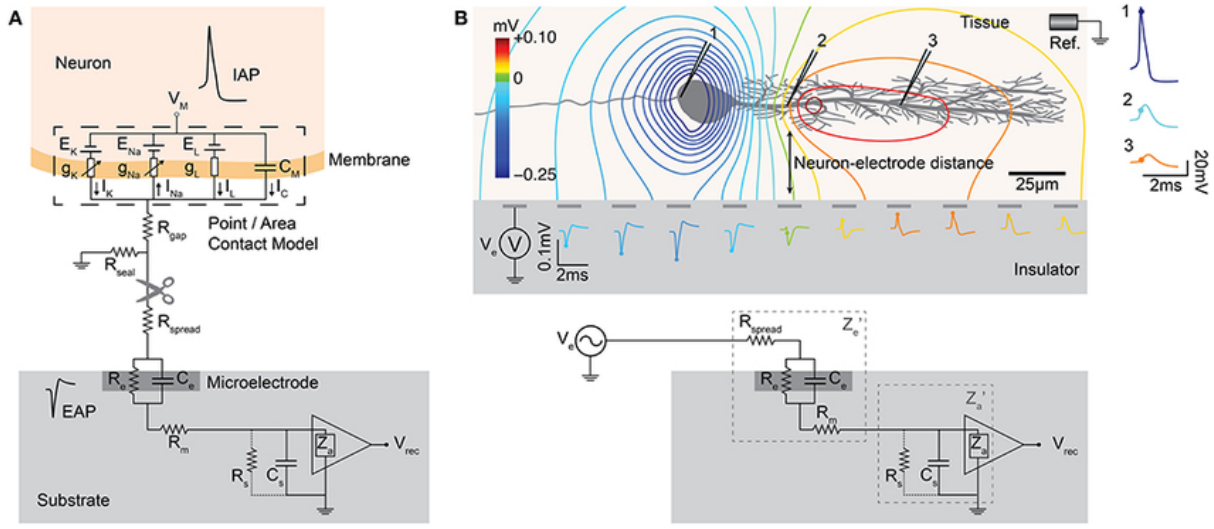

Fig. 11 a) The classic point-contact model of a neuron-electrode interface. The cell membrane is represented with an equivalent model based on the Hodgkin-Huxley model of the squid axon [106]. C_m represents the capacitance across the neuronal membrane. The voltage-gated ion channels are represented by non-linear conductances, g_K and g_{Na}, and the leak is shown as a linear conductance, g_l. The reversal potentials that drive the flow of ions are represented by E_K, E_{Na}, and E_l . The ion flow is shown by I_k, I_{Na}, I_l, and I_C. The location of the scissors indicates where the neuron-electrode interface can be separated into two parts. b) Neuron-electrode interface, fluid and metal sides. The distance between the neuron and the electrode influences the signal amplitude measured at the electrodes. Large negative spikes are recorded at the perisomatic area and positive spikes at the dendritic area of the neuron, the so-called return current. The voltage measured at the electrode is shaped by the electrical parameters of the electrode-electrolyte interface, represented by Z_e as the effective electrode impedance and Z_a as the effective input impedance. Image and figure text adapted from [116].

impedance of the interface Z_e and the effective input impedance Z_a of the bulk metal that transduces the signal to the amplifiers[115].

In this model, the input to the circuit is shown as a low impedance voltage source. The value corresponding to the potential resulting from the currents in the volume conductor. The voltage source V_e is then connected to the impedance of the electrode Z_e which is presented by the resistance and capacitance of the electrode R_e and C_e, the spread resistance R_{spread}, and the resistance of the metal part of the electrode. R_e and C_e are simplified components of the electric double layer at the electrode-electrolyte interface (see Fig. 12). The first layer consists of uniformly oriented ions on the electrode surface due to the chemical interaction

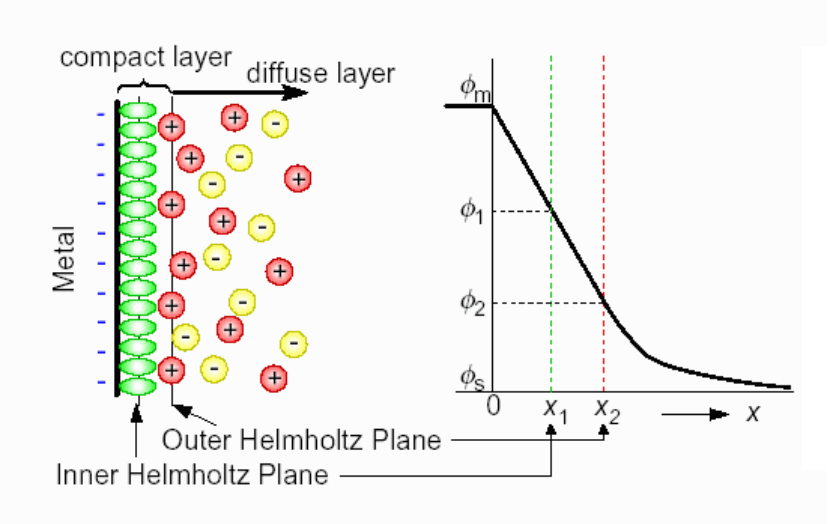

Fig. 12 The image shows the electric double layer at the electrode-electrolyte interface and the voltage drop as a function of the distance from the electrode. As shown, the voltage drops linearly across the first rigid layer, consisting of inner and outer Helmholtz's layers, and exponentially across the diffusive layer. The double-layer is formed to neutralize the charged surface and thus shields the bulk solution from the electrode where the voltage drops to zero. Image adapted from [118].

between the ions and the electrode. This layer is then screened by the second layer where charge redistribution in the media causes changes in the measured potential. The electric double-layer model is used to visualize the ionic environment and the voltage drop in the vicinity of the electrode's surface. This model can be applied both for metal surfaces under potential or ionic groups on a dielectric surface. The voltage drop is shown to decay linearly

at the inner and outer Helmholtz layers and exponentially at the diffusive layer until it reaches zero for the bulk solution [117]. The total capacitance of the electric double layer is given by:

$$\frac{1}{C_t} = \frac{1}{C_H} + \frac{1}{C_D}$$

, where C_H is the capacitance of Helmhotz's layers and C_D is the capacitance of the diffusive layer (see Fig. 12). The impedance is inversely proportional to the capacitance. This means that increasing the conductivity of the double layer will lead to decreasing of the impedance which will improve signal-to-noise ratio SNR given by:

$$\text{SNR}=20\log\frac{A_s}{A_N}$$

, where A_S and A_N are the amplitudes of the signal and the noise, respectively. Increasing the surface area of the electrode will increase the conductance, therefore will lead to better SNR.

2.2.5 Intracellular recordings

Intracellular recording allows the measurement of neural electrical events with a high degree of both spatial and temporal precision. These events account for processes inside the cell whereas the extracellular recordings only detect changes in the local field potential. One fundamental difference between the recorded potential is that while the extracellular recordings have a biphasic waveform starting with a drop in the measured potential, the intracellular signal from recordings starts with a rise in the measured potential (see Fig. 13). By the use of intracellular recordings, measurements of the passive membrane properties can be obtained as well as processes that will otherwise be difficult to separate from the background noise. These properties are resting membrane potentials, postsynaptic potentials, postsynaptic currents, and neuronal input resistance. The patch-clamp technique is a widely used method for intracellular recordings that can obtain a high SNR and good temporal resolution. This technique led to many advances in the understanding of the electrophysiology of the cell and the processes of firing an AP.

Other techniques use three-dimensional micro-and nano-structures as electrodes. This approach is shown to improve the quality of the signal obtained with MEAs to the degree to which the recordings of the spiking activity in vitro exhibit intracellular-like features [119]. Better SNR can be achieved for 3D microelectrodes with different methods of poration, such as spontaneous cell-membrane poration induced by the size and the shape of the electrodes,

electrical poration by bursts of electrical impulses through the electrodes, and spontaneous sealing between the cells and the electrodes by functionalization of the surface[119-121].

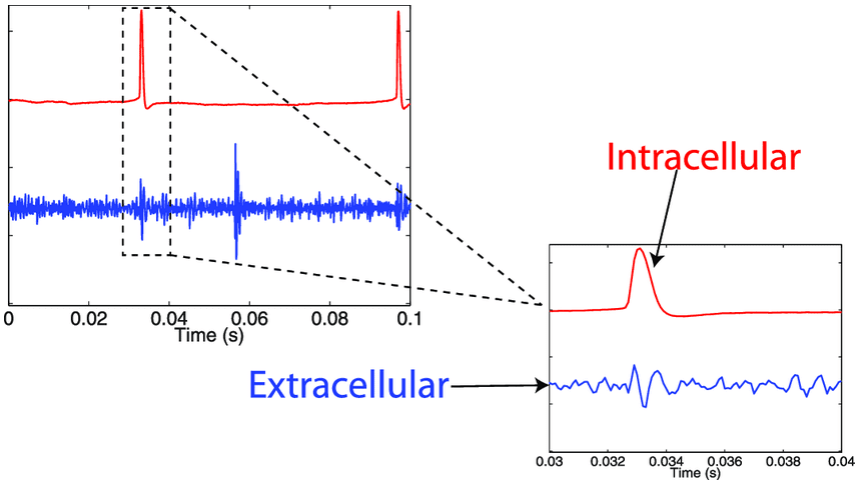

Fig. 13 The image depicts the difference between extracellular and intracellular recordings. The waveform of extracellular recordings is biphasic while the one for intracellular - monophasic. The amplitude of the intracellular recordings is higher due to higher seal resistance. Image adapted from [125].

A drawback of the poration techniques is that they alter the electrical processes inside the cell and damage the cell membrane which alters the recorded signal and commonly leads to cell death after a few hours. Other techniques of intracellular recordings are generally invasive and disrupt normal cell behavior. In the last decade, several research groups investigated the potential of mushroom-shaped microelectrodes to obtain intracellular recordings from neuronal and cardiomyotic tissues in vitro[119,123,124]. The advantage of this approach is that it is not invasive and the cells naturally tend to engulf the spine-like mushroom-shaped electrodes (see Fig. 14). The enlarged surface area compared to plain electrodes contributes to better sealing with the cell and decreases the impedance of the electrode which as mentioned before favors the SNR. 3D MEAs can have tens to more than a thousand electrodes and can be used to better understand how the computational abilities of neurons are linked to their morphology. Such information can facilitate advances in many areas of neuroscience - from better simulation models of the summation of signals inside the cell to drug delivery therapies and neurotoxicity tests.

Recently, in 2020, a method of functionalizing the surface of mushroom-shaped microelectrodes with PEDOT:PSS reported low impedance and significant improvements in the quality of the recordings [126]. PEDOT:PSS coating contributes to the engulfment from the neurons and this results in a high seal resistance value that leads to the enhancement of the coupling coefficient. The sealing resistance models the degree of the attachment between

the neuron and the microelectrode surface. It is generated by the solution within the gap between the surface of the electrode and the engulfing cell membrane.

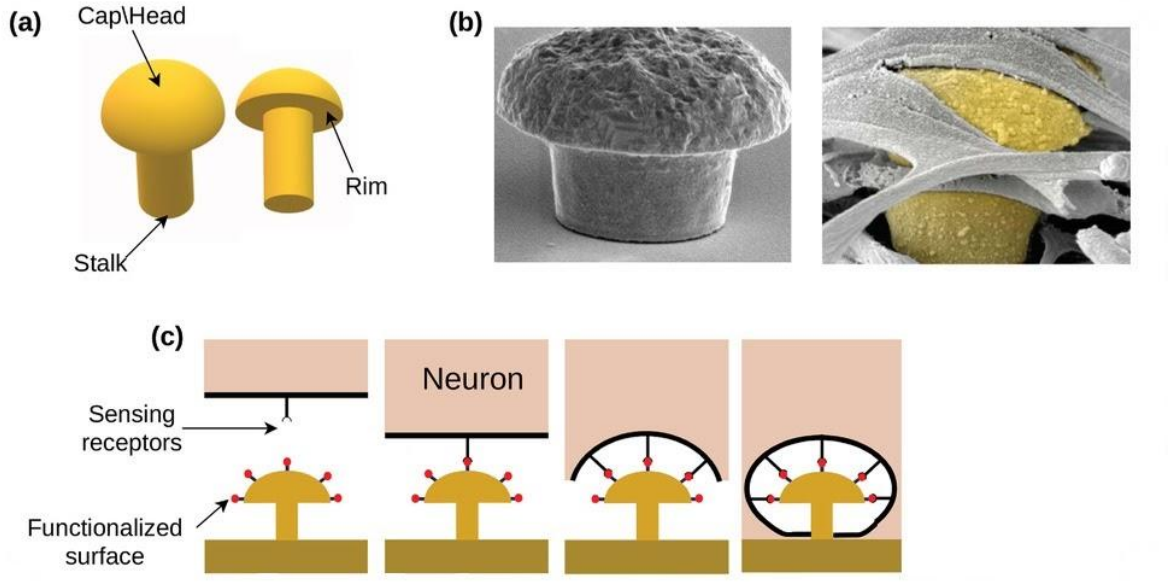

Fig. 14 a) General shape of the electrodes. b) SEM images of mushroom-shaped electrode - after electroplating and after seeding. c) Mechanism of engulfment due to surface functionalization. Image adapted from [127].

While the planar MEAs have poor cell adhesion (low seal resistance value) and are only capable of recordings of extracellular field potentials, the mushroom-shaped microelectrodes are able to record sub-threshold activity generated by individual neurons. Furthermore, with the use of 3D MEAs, it is possible to apply more effective stimulation (as a result of the high electrical coupling) without damaging the cells as less current is needed to achieve the same level of efficiency. This, together with the possibility to record "in-cell"-like recordings with excellent SNR over an extended period of time makes this type of electrodes a promising tool for many preclinical research activities [127].

Intracellular-like signals from neuronal cells can be achieved by securing physical and intracellular access to the electrodes. The engulfment of the GMμEs relies on the naturally occurring phenomenon of particle phagocytosis in living cells. This process is initiated when the cell senses foreign particles with sizes below 0.5 um [127]. Then activation of initiation receptors located in the cell will react with the molecules present on the surface (which shows how important it is to first functionalize the surface of the GMμEs). Next, the receptors of the cellular membrane start recruiting proteins, driven by an actin ring that permits the internalization of the particle into the plasma membrane and ultimately leading to engulfment. The performance of 3D MEAs depends on the nature of the neuron–microelectrode interface. An electrified interface develops when an electrode and a biological tissue are present in an electrolyte. This leads to a specific charge distribution - a formation of an electric double layer, see section 2.2.4. At this interface, two EDLs are formed: one at the side of the electrode and the other at the side of the neuronal membrane.

An EDL can be modeled as an equivalent circuit of a series of three capacitors, one for each layer - Inner and Outer Helmholtz Plane and the diffusion layer. This can be further simplified by connecting a resistor in parallel with the capacitors. This means that the neuron–microelectrode interface can be modeled by passive electrical components

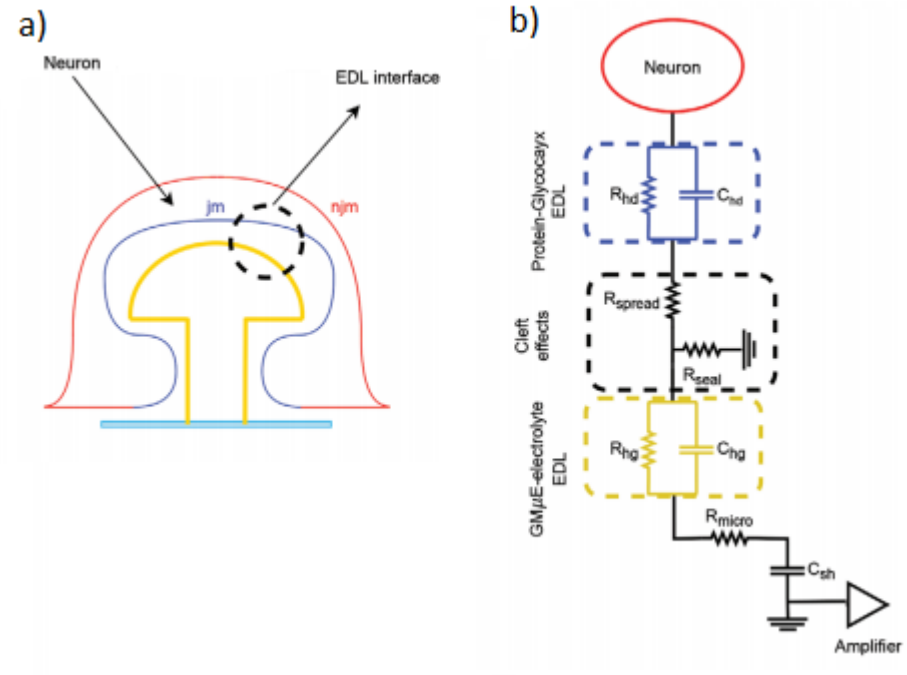

accounting for the cleft effects by introducing spread and seal resistance (see Fig. 15).

Fig. 15 Mushroom-shaped electrode - neuron interface. a)) Sketch of full engulfment by a neuron forming a double EDL at the cleft. b) EDL equivalent circuits shown as: protein-glycocayx EDL, microelectrode–electrolyte EDL, and the cleft effects, modeled by seal and spreading resistance. Image adapted from [127].

Several parameters of the system neuron-electrode are crucial for the quality of the recordings. These are the geometry of the electrodes, the formation of seal resistance, the spreading resistance, the junctional membrane resistance, the cleft thickness, and the density of the MEAs. The processes of fabrication of the mushroom-shaped electrodes determine the geometry of the caps. The first thing to be considered is the diameter of the holes in the photoresist layer through which the electroplating will take place. This determines the diameter of the stalk and therefore the active area of deposition. Next, the electroplating parameters such as applied potential, the temperature of the solution, and time of deposition will govern the evolution of cap diameter and height. These relationships are extensively studied in several papers [128-130]. It has been shown that increasing the temperature increases the diameter and the height of the cap which favors the performance. Four distinct phases of the electrodeposition are outlined by means of sweep voltammetry [128]. For higher overpotentials the deposition becomes porous and hydrogen evolution can occur

which deteriorates the control of the process of deposition. Lower overpotentials contribute to even depositions but slowing down the rate of the deposition.

The use of 3D microelectrodes for intracellular recordings gained a lot of attention from various research teams. Experiments mostly with cardiomyocytes, myotubes, and human embryonic cells have been conducted during the last decade. Although their use in neuronal recordings and stimulations hasn't been thoroughly explored due to the low probability for the neurons to be properly positioned above the electrode and engulf it, functionalization of the surface is a promising approach for the facilitation of successful coupling. However, it is shown [127] that mushroom-shaped microelectrodes in some cases outperform novel microelectrode configurations that use additional techniques to enhance the resolution of the recordings such as poration and penetration into the cell cytosol. Noninvasive in-cell-like recordings can be used to study the neuronal processes of signal transduction and even to promote the growth of neural networks into specific topographies. Also, these electrodes are suitable to be used in studies of muscle injuries and dystrophies paving the way for their potential applications in restoring nerve damage connections.

2.3 Photolithography

Photolithography is an essential step in nanofabrication and thus will be considered in the following section. Preparation of the substrate, spin coating, and physical and optical properties of the photoresists as well as their composition are discussed.

2.3.1 Properties of photoresists

Photoresist's composition
Resists are polymer solutions in an organic solvent containing sensitizer - a photoactive ingredient responsible for the resist ability to change structure under exposure to light. The solvent keeps the resist in liquid form. This is an important requirement for all resits since this allows for the spin coating procedure to take place. In negative resists where the exposed areas become insoluble, non-polar organic solvents such as toluene, xylene, or halogenated aliphatic hydrocarbons are used. In positive resists the solvents are organic - ethyl cellosolve acetate, ethoxyethyl acetate, diglyme, or cyclohexanone [135].

The polymers consist mainly of carbon, hydrogen, and oxygen-based molecules. Negative resists are based on polyisoprene polymers. They are not bonded to each other before exposure to light. Another type of negative resists is photopolymeric resist, e.g. methyl methacrylate. They consist of an allyl monomer that generates free radicals under light exposure. This reaction triggers the photopolymerization of the monomer. Positive resists consist of phenol-formaldehyde novolak resins. They are insoluble if not exposed to light with the necessary wavelength. Photosensitizers are used to change the structure of the

polymer during exposure. The resists undergo either photosolubilization in case of positive resists or crosslinking in case of negative resist. Bisazide sensitizers are used to promote crosslinking and diazonaphthoquinones to promote solubilization. The degree of the efficiency of the sensitizer is given by its quantum efficiency, which counts the fraction of photons that trigger a photochemical reaction. For diazonaphthoquinones sensitizers, the quantum efficiency has been measured to be 0.2 -0.3 while the value for negative resists sensitizers is in the range of 0.5 - 1 [135].

Physical properties of photoresists

Particular resists are chosen to be used, based on the process conditions they will encounter in the subsequent steps of microfabrication. This includes coating, spinning, baking, developing, ion implantation, and etching [136]. The main physical properties of resists are:

- resolution - the ability to differentiate from two neighboring features on the substrate; the smallest critical dimension (CD), achievable with particular resist is a value, directly related to the resolution.
- contrast - the sharpness of the transition from exposed to non-exposed areas; higher contrast means more vertical sidewalls.
- sensitivity - the minimum energy (in mJ/cm^2) required to obtain well-defined features in the resist.
- viscosity - defines the flow characteristics of a resist; it is an important parameter concerning the film thickness, generally higher viscosity gives a thicker layer; it can be changed by introducing more solvent to the resist; viscosity can be given as absolute viscosity (in cps) or kinematic viscosity (in cs), the relation between them is given by:

  $$kinematic\ viscosity[cs] = absolute\ viscosity[cps]/density[SG],$$

  where SG stands for specific gravity, which is a measure of the resist density, related to the solid content remain after soft bake
- adhesion - the resist must adhere to different types of surfaces, such as silicon, silicon dioxide, silicon nitride, and metals.
- surface tension - defined by the strength of the Van der Waals force between the molecules in a liquid, which tends to pull them away from the surface, toward the bulk; the surface tension must be high enough to keep the resist molecules together during spinning and subsequent steps, in the same time must be low enough to ensure for a good flow during dispense.
- etch resistance - defines the stability of the resist during etching; the etch rate is dependent on the conditions, such as pressure, temperature, voltage, gas composition, and concentration.
- electrodeposition resistance - the ability of the resist to withstand an attack by the electrolyte solution; good adhesion to the substrate is required to prevent peeling of resist and underplating; optimal soft bake parameters promote adhesion; hard baking, typically 10 ^0C below the melting point, promotes further crosslinking in negative

resists and also increases the adhesion but this leads to difficulties with the post-electroplating removal [135].

Optical parameters of photoresists

When light passes through different media, it changes its speed, direction, and intensity. The refractive index n, the absorption coefficient α , and the extinction coefficient are optical parameters that account for these changes and they are all dependent on the wavelength. The refractive index gives the speed of the light in the medium. The complex refractive index expressed as $n^{\star} = n + ik$ accounts for the amount of attenuation of the light passing through the material, where the imaginary part is responsible for the rate of this attenuation. The intensity of the incoming light I_0 decreases exponentially with the distance $d$when it passes through the resist. The absorption coefficient αis material dependent and accounts for the penetration depth of light after which intensity has dropped to 1/e. This can be expressed as:

$$I = I_0 \exp(-\alpha d) \text{ , where } \quad \alpha = \frac{4\pi k}{\lambda}$$

Other important parameters of the photoresists are the Cauchy constants and the Dill parameters. Cauchy constants are used to express the refractive index as a function of the wavelength:

$$n = N_1 + \frac{N_2}{\lambda^2} + \frac{N_3}{\lambda^4}$$

, where $N_1$is a dimensionless quantity, $N_2$and $N_3$are measured in [μm^2]and [μm^4]. The Dill parameters express the extinction coefficient as a function of the concentration of the photoactive compound (PAC) in the resists:

$$k = \lambda \frac{A(\lambda).PAC + B(\lambda)}{4\pi}$$

They are wavelength dependant and are measured in [μm^{-1}]. The concentration of PAC takes value from 0 for fully exposed to 1 for unexposed.

2.3.2 Substrate preparation

Solvent cleaning

To remove organic impurities and particles, the substrate undergoes cleaning in acetone and isopropanol. In the case of cleaning a resist residue, is recommended to have two acetone and two isopropanol baths in this order[131].

Plasma cleaning
After cleaning in acetone and isopropanol, and drying under a nitrogen gun, the substrate is placed in an oven for oxygen plasma cleaning (50 sccm O2 flow at 0.26 mbar pressure and 50 W power for 5 min.). The vacuum UV inside the oven easily breaks apart high-weight molecular contaminants. Oxygen species, such as ionized ozone and excited metastable oxygen atoms and molecules form H2O, C02, CO with the organic contaminants, which are then evacuated from the chamber.

Dehydration bake
This step is performed to evaporate residual water from the wafer surface. For clean 2-inch substrate 2 minutes at 100 ^{o}C is sufficient. The surface of the wafer turns hydrophobic and promotes better adhesion with the resist. The spin coating should be performed right after dehydration and cooling down on a cold plate. Dehydration bake, however, is not completely efficient. The silicon atoms on the surface of the substrate bond to water molecules and form Si-O-H connectivity named silanol groups. To remove this layer the temperature must exceed 600 ^{o}C. This method is ineffective in a water-containing environment since the silanol quickly reforms back on the surface [132].

Vapor priming
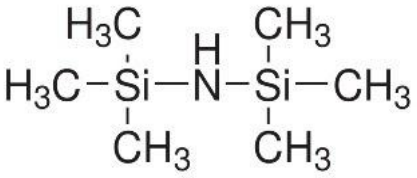
Introducing an adhesion promoter to the substrate surface is a common step in photolithography to achieve stable adherence of the resist layers. HMDS or hexamethyldisilazane (chemical structure shown on right) is an organosilicon compound that is widely used for this purpose. It is crucial for this step the wafer to be dehydrated from the water molecules that are bound to the silicon on the surface. Dehydration leaves OH-groups on the surface, meaning that it is still hydrophilic. After introducing HMDS, usually through vaporizing it in a vacuum chamber together with the wafer, the silicon atoms in the trimethylsilyl group ((H3C)3Si) bond to the oxygen in the OH-group, sufficiently maintaining this connection and exposing the (H3C)3Si-group as a surfactant that is highly hydrophobic.

2.3.3 Spin coating

Thickness influence factors
During spin coating, a few milliliters of photoresist are distributed over the substrate by the centrifugal force resulting from spinning with up to several 1000 rpm. The main goal of this procedure is to deposit a uniform thin film of photoactive polymer. Two parameters of the resist - viscosity and density (solid content) and two of the spinning - angular momentum and spin time are most important for achieving the desired film thickness [133]. The film thickness as a function of time is first derived by Emslie, Bonner, and Peck in 1958 [134]:

$$\frac{dh}{dt} = \frac{2\rho\omega^2 h^3}{3\eta_0}$$

, where $h$is thickness, ρis density, ωis angular momentum or spin speed and $\eta_0$is viscosity. The thickness is then determined by the equation:

$$h = \sqrt{\left(\frac{4\rho\omega^2}{3\eta_0} t\right)}$$

The next stage of film thinning is due to evaporation of the solvent during the soft bake and it is not depicted in this formula. However, some general conclusions could be derived from it. First, the film thickness increases with increasing viscosity. Second, lower spin speeds increase the spinning time for constant thickness. This dependence allows for adjustments of both the spin speed and spin time in order to achieve the desired thickness. For certain resist, the thickness of the film is mainly determined by the angular momentum ωof the substrate. A good approximation of the resist thickness dependence of the spin speed is that the thickness decreases with the reciprocal square root of the spin speed [131]. Thus for a given spin speed and thickness, one can calculate new values in order to achieve the intended thickness. Control of the spin time to control the thickness is more common for thick film resists where the spinning can be stopped before the complete spin-off of the resist. For thin-film coating, it is important to have a sufficiently long spin time (20-30 sec.) to achieve reproducible results. The temperature of the resists affects the rate of solvent evaporation and viscosity. These two parameters have an opposite effect on the thickness of the film and thus for a small deviation of the $t^0$with a few degrees no sufficient change will be observed. The recommended temperature for storage and use is in the range of 20-25 ^oC.

Thickness versus spin-speed

The general dependence between the thickness of a spin-coated film and the spin speed is given by:

$$h_f \propto \frac{1}{\sqrt{\omega}}$$

, where h_f is the thickness and w is the angular momentum, measured in [rpm]. The required thickness $h_2$can be achieved with the speed of rotation w_2[rpm] once one has measured the thickness h_1 obtained at speed w_1:

$$h_2 = h_1 . \sqrt{\frac{w1}{w2}}$$

$$w_2 = w_1 . h_1^{\,2} / h_2^{\,2}$$

These equations represent the connection between the ratio of the angular momentum and the squared reciprocal ratio of the thicknesses. The time and acceleration have to be kept constant.

2.4 Electroplating

Electrochemical deposition, or electroplating, is a thin film growth process that refers to the formation of a metallic coating onto a metal substrate by means of electron transfer between an electrolyte and an electrode. The process of deposition occurs through the electrochemical reduction of positively charged metal ions from the electrolyte on the negatively charged surface of the cathode. The electrolyte is a solution of positive and negative ions and can be considered an ionic conductor. The cathode and the anode are connected to a battery or other power source. This arrangement allows for electrons to be directed from the power supply to the cathode. The electric current through the bath is carried by positively charged ions which migrate from the anode to the cathode where they undergo reduction. The process can be generally described by the equation:

$$M^{+n} + ne^{-} \rightarrow M$$

The most common method to electroplate platinum in academic projects is to use solutions that contain hexachloroplatinic acid. Such baths have been used to electroplate Pt microparticles, arrays of Pt microwires, Pt foams, and Pt black coatings. The height of the coatings is directly related to the time of deposition while the morphology of the depositions is dependent on the rate of the reduction or reaction rate. The reaction rate can be either diffusion-limited or reaction-limited. In the first case, the applied voltage (or supply of electrons) is high enough to reduce all available ions and the rate of the reaction will be determined by the mass transport of ion species. In the second case, when the diffusion is sufficient to support the necessary concentrations, the reaction rate is limited by the applied potential or the current through the electrode. This allows for fine control of the thickness and the morphology of the deposited metal.

Besides the diffusivity of ionic species, their mobility and activity also play an important role in the dynamics of the electrolyte and subsequently on the deposition. The mobility of ions reflects their ability to move through a medium in a response to an electric field. It is measured in $[m^2/V.s]$ and is given by:

$$\mu = \frac{v_d}{E}$$

, where v_d is the drift speed and E is the electric field. The activity of ions is a measure of their effective concentration. Due to the fact that ions in solution will interact with other molecules, water, for example, the effective concentration of active, available for reaction ion species will be smaller than the real concentration in the bath.

Other important concepts for understanding the hydro- and electrodynamics of an electrolyte are the so-called solvation sphere and ionic atmosphere (see Fig. 16). Ionic atmosphere refers to the dynamic volumes of solution in which the unbalanced charge draws up ions of the opposite sign that tend to cancel it. The ions are also in constant motion due to their thermal energy and tend to move apart. The interplay of these two opposite forces produces a volume of ionic charge that effectively cancels the unbalanced charge, screening it from the rest of the fluid.

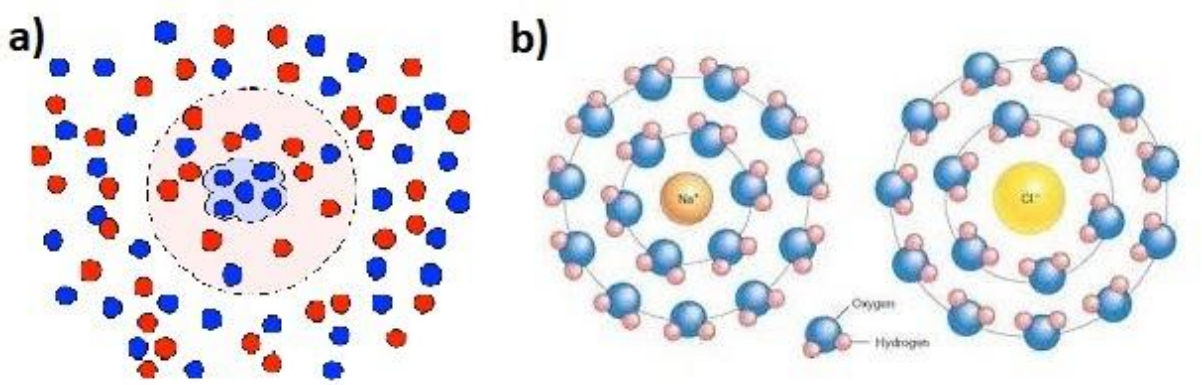

Fig. 16 a) The image depicts the concept of an ionic atmosphere. Charged species attract ions with opposite charges to form a local balance. The volume of charge cancelation is a dynamic entity that accounts for the electrolytic conductivity behavior. Image adapted from [137]. b) The image presents the concept of a solvation sphere. Molecules of the solvent arrange around charged particles due to the charge concentration gradient. Van der Waals's forces keep this formation relatively stable. Image adapted from [138].

The solvation sphere describes the solvent interface with charged ions. The molecules of the solvent arrange around the ions forming weak bonds that tend to cancel the charge gradient between them. This way a dynamic sphere around the ions can be distinguished. It consists of inner and outer layers of solvent molecules surrounding the charged species. This concept is important when considering the hydrodynamics of the system.

When considering the reduction reaction that happens at the surface of the electrode, it is important to understand the formation of the so-called Helmholtz double layer. This formation of two layers is generally the same as the electric double layer described in section 2.2.5. When the charged ions reach the surface of the electrode they form a one atom thick layer of evenly distributed reduced ions - the first layer of Helmholtz. This layer, also called

the surface layer, consists of the absorbed ions with shifted electron clouds due to the applied current/voltage. The unidirectionally shifted electron clouds give rise to polarization of the surface. The second layer consists of ions that are attracted to the surface layer via Coulomb's force. This layer, electrically screening the first layer gives rise to a so-called hindering reaction. The hindering reaction describes the oscillations in the system of two layers due to the interplay between screening the first layer and reducing the second layer to become a part of the substrate. The total amount of reduced ions can be measured by the current that passes through the electrode. This is a consequence of Faraday's first law of electrolysis which states that the extent of a chemical reaction, or the amount of electroplated metal, caused by the flow of current is proportional to the amount of electric charge that passed through the electrochemical cell. This can be written as:

$$Q = nFN$$

, where Q is the charge transfer, n is the number of electrons needed to reduce one ion to an atom, F is Faraday's constant, and N is the amount of reactant that is absorbed by the surface of the electrode. From $I = dQ/dt$, the following expression for the measured current can be written:

$$i = nFdN/dt$$

From the last equation, the rate of the reaction can be expressed as a function of the current. Taken for a given area of deposition, the rate of reaction or the total amount of reactant consumed, considering that we know the density of platinum, can be rewritten in the following form:

$$h = \frac{m.i.t}{nF\rho A}$$

, where h is the height of deposition, m is the molar mass for platinum, ρis the density, and A is the area of deposition.

By modeling the evolution of the concentration of ions at the electrode surface, using a one-dimensional model, it is suggested that the concentration of ions would fall to zero after a certain period of time, called Sand's time [139]. After this time, the potential on the electrode surface will start to diverge in order to escape the instability of the system, giving rise to dendritic formations [140]. Results from simulations of the deposition behavior of Li are shown in Fig. 17. They depict the general dependence of the morphology of the deposition on the current density which is also valid for other metals. In the figure, the background color represents the ionic concentration, the green lines represent the spatial distribution of the surface with equal potential energy in the electrolyte, and the red arrows indicate the strength and direction of the current density. Pronounced growth can be seen around the corners of the

seeding sites (shown in gray). This is due to higher densities of the ionic current around the corners which makes them preferential deposition sites. When a higher overpotential or current is applied to the cathode, directional growth towards the anode is observed. This is shown in Fig. 17c. Overpotential is the potential difference between the reduction potential and the potential at which the redox event is experimentally observed. For higher overpotentials, the inhomogeneity of the electrolyte will cause local disturbances of the field that will lead to higher ionic current densities and branching towards the counter electrode. This directional branching is supported by the depletion of ions below the active zone of deposition which is shown in blue on Fig. 17c,d, and e.

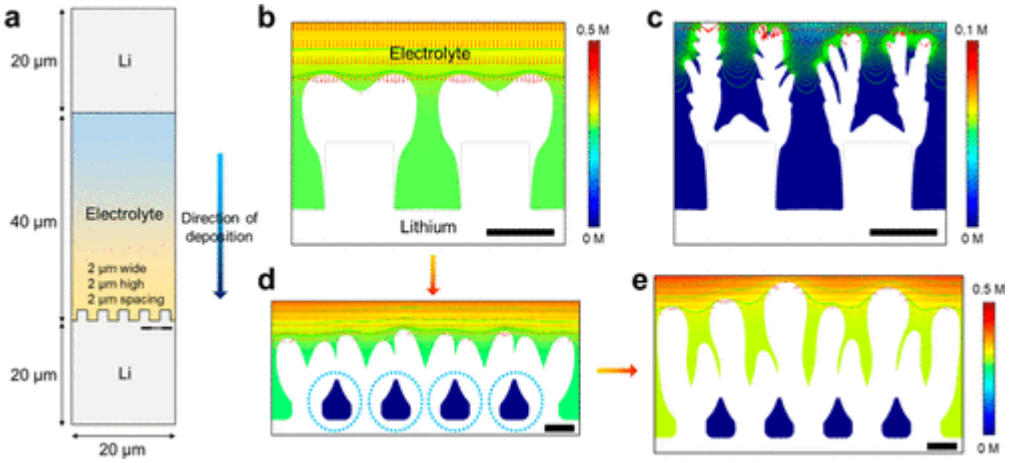

Fig. 17 a) Schematics of the cell. b-d-e) Results from simulation of low-rate deposition of Li. The background color indicates the concentration of ions, with green are shown the equipotential lines with a step of 2.5meV, the red arrows indicate the direction and strength of the ionic current, scale bar 2um. Image adapted from [140].

From the results for electrodeposition at different rates can be concluded that the deposition starts initially at unevenly distributed sites where the equipotential lines are more densely packed. The evolution of these deposition seeds depends on the density of the ionic current. For even depositions with less directional growth lower overpotential or current applied are needed.

2.5 Instruments

2.5.1 Maskless Aligner Heidelberg MLA150

The MLA150 is a maskless aligner capable of direct laser writing which makes it very useful for prototyping and small-scale production. It has two laser sources - 375 nm and 405 nm. This makes it compatible with all photoresists in NanoLab. The resolution limit of the instrument is 1 um. This means that it can expose patterns with features down to 1 um as a critical dimension. A spatial light modulator is used to imprint the design onto the photoresist

layer. It serves the function of a light switch (see Fig.18). The exposed pattern consists of many individually imprinted stripes. The laser unit consists of several laser diodes, that are projected onto a digital micromirror device (DMD). The DMD is a micro-electro-mechanical system that converts electrical signals into an optical laser output. It comprises a micrometer-sized semiconductor-based array of light switches, that individually corresponds to a pixel in the designed image intended to be written into the photoresist. When the laser light is directed onto the DMD, these optical mirrors will guide the light in the desired direction through the write head and onto the photoresist. The advancement of these devices allows splitting the laser beam into addressable dots, each of which can be concentrated in a different plane[141]. This is a promising tool in different fields - from photonics to biomedicine. Integrated into optical tweezers, DMD is used for the precise separation of cells in a PDMS chip[142, 143].

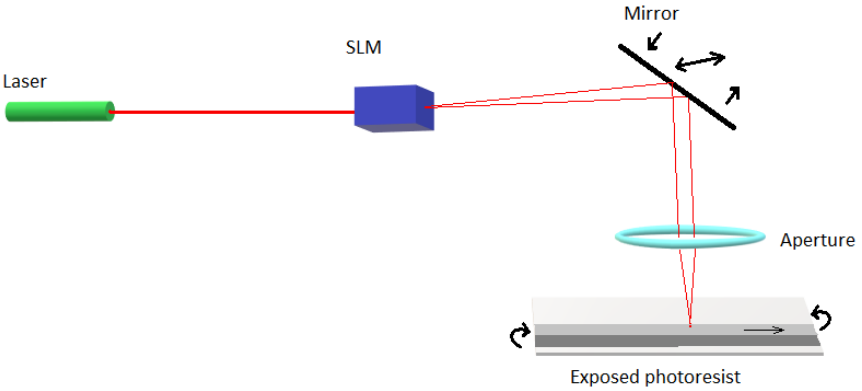

Fig.18 Optical path of a laser beam passing through a spatial light modulator and focused on the photoresist film. In dark grey is shown a fully exposed stripe of the resist, lighter gray indicates the stripe that is under exposure.

The exposure dose is measured in mJ/cm2 or the intensity of the laser (photons per unit area) times the duration of exposure. This characterizes the total amount of photons that a given area will receive and thus the degree of crosslinking in the negative or photoactivation in the positive resist. The spatial range for which the intensity of the focused laser spot is constant and keeps the resist profile of a given feature within all specifications (linewidth, sidewall angle, and resist loss) is called depth of focus (DOF) [144]. DOF is an important parameter to be taken into consideration when working with thick resist and/or small features with high aspect ratios[145-147].

2.5.2 E-beam evaporator and Sputter AJA International Inc. Custom ATC-2200V

The thin-film deposition is an essential part of micro-and nanofabrication. It allows depositing metals, dielectrics, or semiconductors onto developed photolithographic patterns.

In this project, metal vapor deposition was used with a subsequent lift-off in acetone to create the metal pattern of the MEAs. There are mainly two types of vapor deposition - chemical (CVD) and physical (PVD). CVD uses thermally induced chemical reactions at the surface of a heated substrate, the reactants are supplied in gaseous form. In PVD the film of coating material is deposited atom by atom on a substrate by condensation from a vapor phase to a solid phase. While the CVD processes require high temperatures and can lead to the formation of corrosive waste products, the PVD can take place at room temperatures without corrosive waste or impurities in the deposited film. One disadvantage of PVD over CVD is the lower growth rate of the film thickness. The E-beam evaporator is a PVD instrument that uses electrons with high kinetic energy to strike a metal target and evaporate part of the material. The main components of an e-beam evaporator are an electron gun in a vacuum chamber, a magnetic field to accelerate the electrons towards the target, a valve rotating the sample for even distribution of the condensed metallic gas, and a sapphire detector to measure the deposition rate and the endpoint for the process (see Fig. 19). The electron gun is

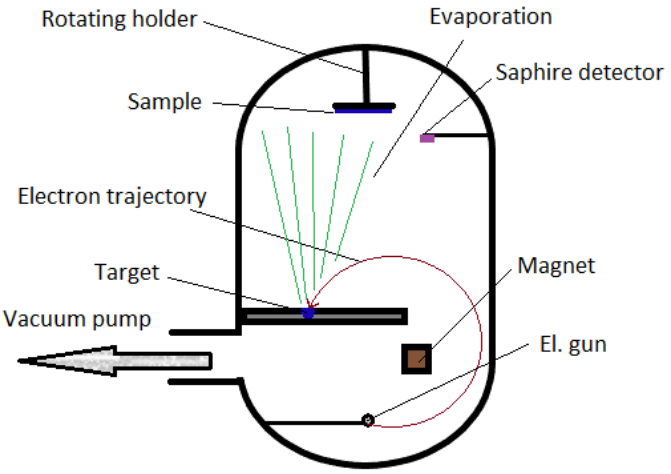

Fig.19 Schematic of e-beam evaporator with the main components of the system. The chamber is kept under a vacuum while the electrons from the e-gun are accelerated and their trajectory is bent towards the target. The evaporated material is then deposited by means of sublimation onto a rotating sample. The rate of deposition is monitored by a sapphire detector.

a metal chunk made out of tungsten and heated in order to extract electrons which are then accelerated towards the target. The whole process of deposition takes place in a high vacuum (10E-7 Torr) provided by a turbomolecular pump. For this particular project, the instrument was used to deposit 50 nm Ti on a borosilicate wafer as an adhesion promoter and 100 nm Pt to form the metallic part of the MEAs.

2.5.3 Oxford Instruments PLasmaLab System 100-PECVD

Plasma Enhanced Chemical Vapor Deposition is a version of CVD. Instead of using high temperatures to induce a chemical reaction, it uses plasma induced by electrical discharge.

PECVD is mainly used for the deposition of dielectric films and passivation films like silicon oxide or nitride at low temperatures and pressure of 0.5 - 2 mTorr. The basic construction of this instrument consists of two electrodes, gas inlets, and an exhaust. One of the electrodes is connected to a radiofrequency (RF) of 13.56 MHz and a low-frequency (LF) of 50-460 kHz sources that can be applied simultaneously, the other one is grounded. Switching between RF and LF allows for control of the film stress. The electric field between the electrodes ionizes the gasses. This ionization of the gasses makes their molecules chemically reactive and they migrate to form a thin layer onto the substrate. By-products of the reaction and process gasses are evacuated through the exhaust (see Fig. 20)

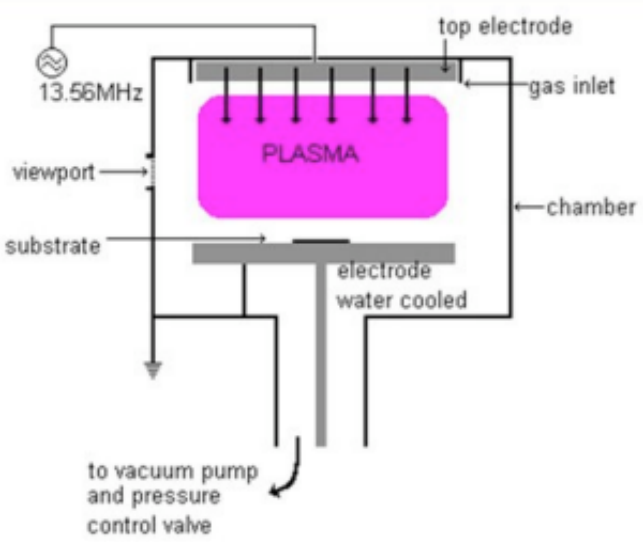

Fig.20 Schematic of PECVD chamber. The gas enters through a showerhead above the sample, then is ionized by the oscillating electric field. The excess material is brought out through the exhaust.

For this project, the PECVD (Oxford Instruments) system was used to deposit approximately 470 nm of Si3N4 as a passivation layer for the metal connecting lines of the MEAs. Process parameters that determine the deposition quality and rate are gas flow, pressure in the chamber, temperature of the substrate, plasma excitation power supply. They can be controlled manually from the software of the instrument. Changes in the parameters lead to changes in the growth rate and the structure of Si3N4 film which in turn affects the film stress[148]. The most relevant parameters in this regard are the excitation frequencies, the temperature, the pressure, and the gas flow. By using the two sources sequentially, the density of the plasma can be controlled, and thus the film stress. Increasing the excitation power will lead to denser films with more compressive film stress. The temperature of the substrate can affect the density of the film, as an increased temperature will cause a decreased deposition rate which will accumulate higher tensile stress. Higher pressure leads to an increased deposition rate. The ratio of the introduced gases will affect the stoichiometry of the deposited layer.

An already optimized recipe was used for the deposition (see Appendix). The chemical reaction that the gasses undergo in the chamber is:

$$SiH4(g) + 4NH3(g) \rightarrow Si3N4(s) + 12H2(g)$$

Silane and ammonia are mixed in a gaseous phase to form a solid silicon nitride film. Silicon nitride has a high heat-stability, wear, oxidation, and corrosion resistance. It is non-reactive to chemicals, a biocompatible material that finds applications in the medical field and particularly in the fabrication of implants and biosensors[149-151].

2.5.4 Oxford Instruments Plasmalab System 100 ICP-RIE 180

Inductively Coupled Plasma Reactive Ion Etching (ICP-RIE) is an anisotropic dry-etch technology that uses chemically-reactive plasma to remove thin film materials from substrates. The independent control of ion density and acceleration towards the sample enables high process flexibility, enlarging the window of working parameters. There are two RF sources connected to the instrument. The first one is connected to the plasma generator (a coil around the main chamber, see Fig. 21) and uses alternating RF magnetic fields to induce RF electric fields, which interact with the electrons in the gas molecules to create a high-density plasma. The second source is connected to the wafer stage and generates a DC bias that accelerates the ions towards the sample.

Process parameters such as excitation power, radiofrequency, gas flow, temperature, and pressure have tremendous effects on etch rates and etch selectivity. The film etch rate increases with the increase of the power under various pressure and flow rate conditions [152]. The same is valid for the temperature and the pressure. In this project, the ICP-RIE was used to etch through the Si3N4 passivation layer using fluorocarbon gases CF4 and CHF3. The areas above the deposited platinum were patterned with a negative photoresist that is resistant to these gases so that the developed areas are exposed to the plasma.

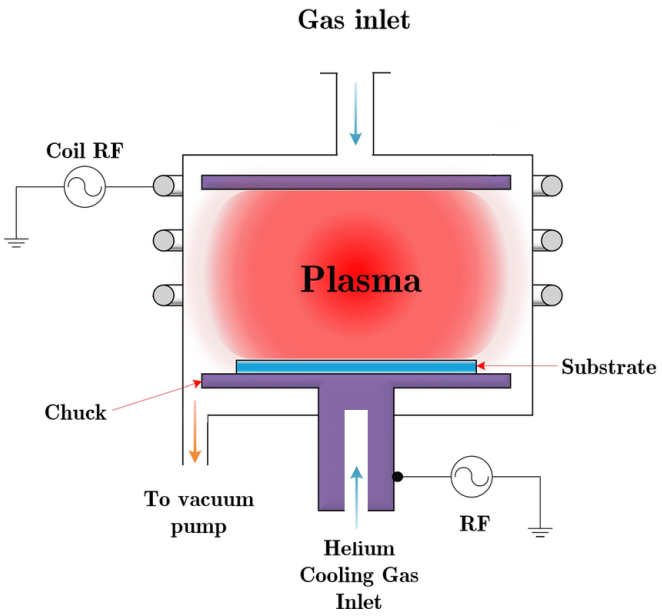

Fig. 21 Schematic of ICP-RIE. The gasses that are introduced to the chamber are ionized by means of applied RF fields. The flow through the gas inlet and the exhaust determines the pressure in the chamber. The temperature of the substrate is controlled by a helium cooling system.

Profilometry

Profilometry is a technique that uses either light or a physical probe to extract topographical data from the surface of a sample. Different modes of scanning include single-point scan, line scan, and full three-dimensional scan. The obtained data is used to determine the step height, surface morphology, and surface roughness of photoresist layers and electroplated 3D formations. Step height provides the height difference between two planes defined by two areas on a surface. The surface roughness is quantified by the deviations in the direction of the normal vector of a real surface from its ideal form.

2.5.5 Reflectometer

A reflectometer is an instrument that uses a light source and a detector to measure the amount of reflected light from a thin film (see Fig. 22). Changes in the reflectance are measured for a range of wavelengths to obtain reflectance spectra which are then compared to a series of calculated spectra. Reflectance can be expressed as a function of the refractive index and thus the system can be used to either measure thickness by having data for the λ-dependence of the refractive index of the film, or to measure the refractive index n by knowing the thickness. Once the necessary sets of data are uploaded the instrument is very easy to use for quick evaluation of film thickness. In this project, the optical system was used to collect data for the dependence of the film thickness versus spin coating parameters such as spin speed, spin time, and the substrate material.

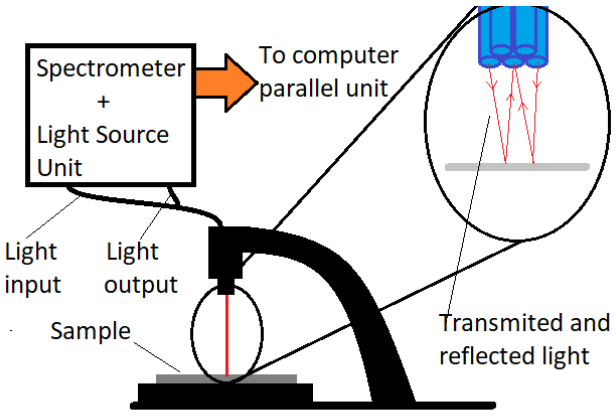

Fig. 22 Schematic of refractometer. Light transmitter and detector are employed to measure changes in the reflectance of light from a coated sample surface. These changes are used in algorithms to calculate the height of the coated film.

2.5.6 Profilometer Veeco Dektak 150

This is a contact measurement system. It works by physically moving a probe along the surface of a sample in order to extract topological data as step height and surface roughness. The tip of the probe is a diamant cone with 12.5 microns width. This limits the lateral feature sizes that can be detected. The instrument uses a force feedback system that provides constant pressure on the tip of the probe. This system is very sensitive to changes, thus having a high resolution in the z-direction, capable of detecting features with sizes down to a few angstroms. One limitation of the instrument is coming from the fact that it uses contact mode. This makes it not suitable for measurements of soft surfaces due to possible contamination of the probe and compromising the film structure. The feedback system of the profilometer usually consists of a magnetic solenoid on the opposite side of the pivot. A small magnet resides inside the solenoid and drives current through it when it moves. This allows for precise measurement of the position of the pivot according to the measured changes in the current. The feedback system uses this data to adjust the current and therefore the magnetic force applied on the pivot. This allows for the support of particular constant pressure on the tip, called Setpoint pressure. Different types of detectors can be used to account for changes in the position of the pivot. In Fig. 23 below is illustrated a scheme of the instrument with an optical lever - laser and photodiode.

In this project, a Stylus profilometer was used to determine the differences in film thickness of photoresist before exposure and after development. This data was used to analyze the

effect of different exposure doses and time of development on the film thickness. The instrument was also used to characterize the surface roughness of the resist and the profile of edge beads.

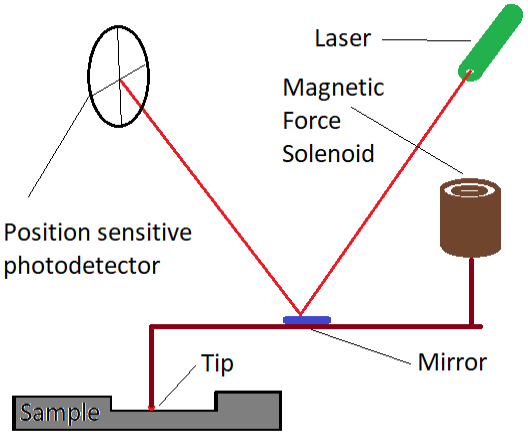

Fig. 23 Schematic of Stylus profilometer. The instrument consists of a solenoid that monitors changes in the pressure of the tip and an optical lever that measures changes in the position of the tip.

2.5.7 Optical Profiler Bruker Contour GT -K

In optical profilometry, a light source is used instead of a physical probe to obtain the surface features. This can be done by the usage of principles in optics such as optical interference, focus and phase detection, or projecting a pattern onto the surface to examine the topography. In general, optical profilometry exploits the interference between a reference light beam and a measuring beam reflected from the sample surface (see Fig. 24). If the traveled distances of the two beams differ by an even number of half wavelengths then a bright fringe (constructive interference) is created. If the difference is equal to an odd number of half-wavelengths a destructive interference occurs which creates dark fringes. In intermediate cases, a spectrum of gray lines is created. The height of a particular point on the sample surface can be calculated by the type of interference, which is captured by the color of the corresponding pixel. In this mode, the maximum height that can be measured is determined by the number of fringes. Measurements of thicknesses and refractive indices of transparent thick polymer films based on light interference are widely used and different algorithms are developed to properly account for specific properties of the coatings. They are based on the fact that fringes from the upper and lower boundaries of the film are well separated, which allows calculating the film thickness or the refractive index from the distance between the envelopes of the two fringe patterns. When the film thickness decreases below 1 um, the envelopes of the two fringes come so closer to each other that they overlap. This complicates the calculation of the distance between fringes, and thus the film thickness [153].

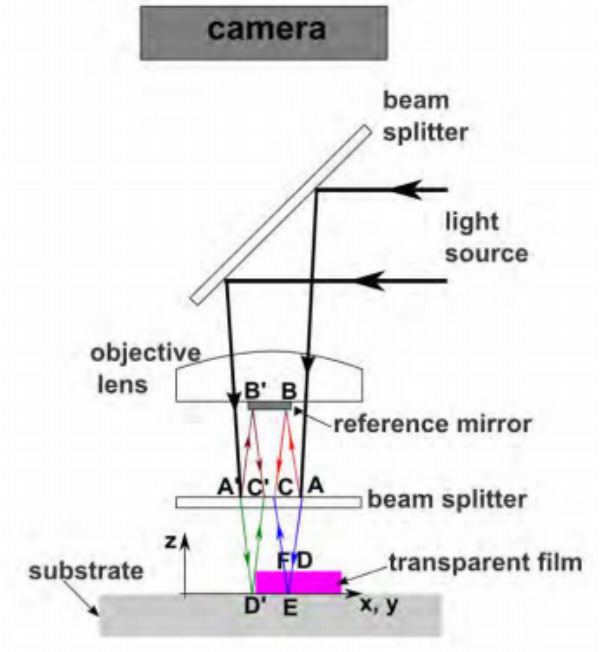

Fig. 24 Schematic of Optical profiler. The instrument consists of a light source, beam splitter, and reference mirror. The incoming beam is split in two and then merged again, the difference in the pathways creates the interference pattern that is used to calculate the film thickness.

2.5.8 Scanning Electron Microscope FEI Apreo

A scanning electron microscope (SEM) uses a focused beam of electrons to produce images of a sample by scanning the surface. The electrons interact with atoms in the sample, producing various signals that contain information about the surface topography of the sample. The signals used to produce an image result from interactions of the electron beam with atoms at various depths within the sample. The types of signals that are produced include secondary electrons (SE), reflected or back-scattered electrons (BSE), characteristic X-rays, absorbed current (specimen current), and transmitted electrons. These outcoming electrons/X-rays give information about topography, morphology, composition, orientation of grains, and crystallographic information for the material [154]. Characteristic x-rays are produced by displacement of an electron in the valence shell of the specimen by the primary electron beam. As the electron is displaced, an electron from a higher valence shell must fill its orbit, and X-rays are produced. Backscattered electrons are reflected back after elastic interactions between the beam and the sample. Secondary electrons originate from the atoms of the sample: they are a result of inelastic interactions between the electron beam and the sample. The electron beam is scanned in a raster scan pattern, and the position of the beam is combined with the intensity of the detected signal to produce an image. The most common SEM mode uses secondary electrons (SE). SE are emitted by atoms excited by the electron

beam and are detected using a secondary electron detector (see Fig. 25). The number of secondary electrons that are collected depends on specimen topography. This determines the

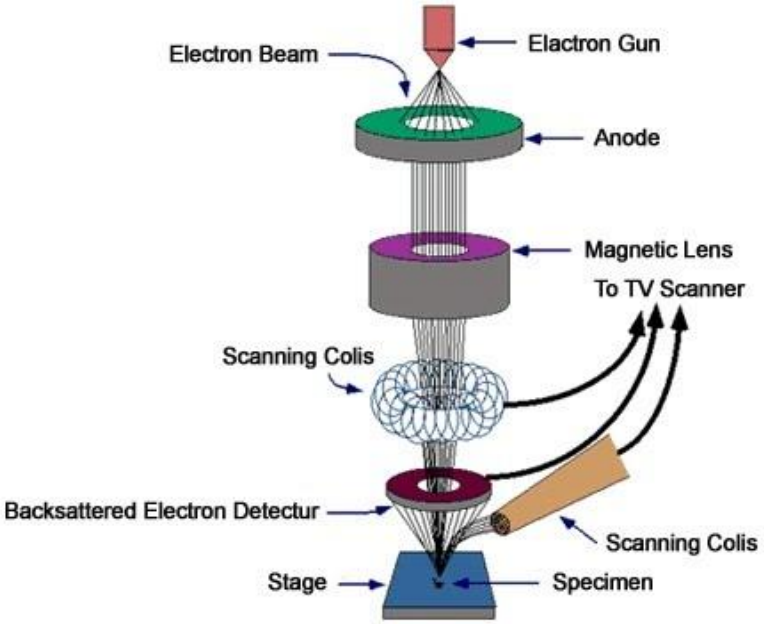

Fig. 25 Schematic of a Scanning electron microscope. SEM consists of a high tension system for generating electron beam - e-gun and anode for the acceleration of the electrons, a vacuum system that assures the electrons arrive at the specimen efficiently, a lens system for electrical control of the lens, and detection systems for collecting the signals. Image adapted from [156].

intensity of the signal. The samples are placed in a high vacuum to avoid contamination[155]. The electron beam is composed of electrons that are emitted from a filament and collimated in the electron source. The beam is then focused on the sample surface by a set of electromagnetic lenses placed in the electron column.

Chapter 3

Materials and methods

3.1 Fabrication of 3D MEAs

The fabrication of mushroom-shaped microelectrodes is described in the following section. An overview of the main process steps is provided in Fig. 26. The full protocol for fabrication can be found in Appendix A1.

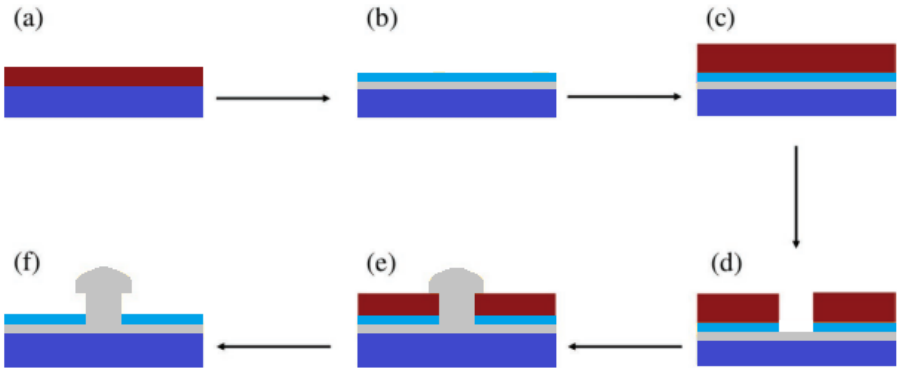

Fig. 26 Overview of the main steps in fabrication of mushroom-shaped microelectrodes: a) photolithography of the design for the metal contacts b) thin-film metal and passivation layers deposition. c) photolithography to determine the exposed metal sites d) etching through passivation layer e) electrodeposition f) stripping of photoresist.

3.1.1 Photolithography

Photolithography was used to form the pattern for the metal contacts of the MEA (see Fig. 27). The photoresist ma-N 440 was chosen for its suitability for lift-off and for its resilience to both etching and electroplating. 4-inch borosilicate wafers were used as a substrate for spin-coating of the photoresist at 3000 rpm for 30 sec. with an acceleration of 200 rpm/s. After soft-baking at 95 ^{0}C for 5 min., the pattern was exposed with Heidelberg MLA 150 with exposure doses of 2400 mJ/cm2 for the first layer and 800 mJ/cm2 for the second layer. The reflection of photons from the metal layer during the second exposure leads to a higher degree of crosslinking compared to the resist above areas without a metal layer. To reduce the resulting difference in the resist thickness across the sample, another exposure of the second layer with 200 mJ/cm2 was performed outside the metal pattern. After post-exposure bake at 110 $^{0}C$for 90 sec., the pattern was developer ma-D 332/S for 2 min. 15 sec.

3.1.2 Thin-film deposition

E-beam evaporator AJA International Inc. was used to deposit 50 nm of titanium and 100 nm of platinum on the developed pattern with a rate of 5Å/s (angstrom per second). After subsequent lift-off in acetone, followed by a rinse in IPA, the exposed metal pattern underwent a PECVD (PECVD system from Oxford instruments) of 470 nm of Si3N4 through mixing SiH4 at 20.0 sccm, NH3 at 20.0 sccm and N2 at 980 sccm. The release step was set to 30 min., and the temperature of the substrate to 300 ^{0}C.

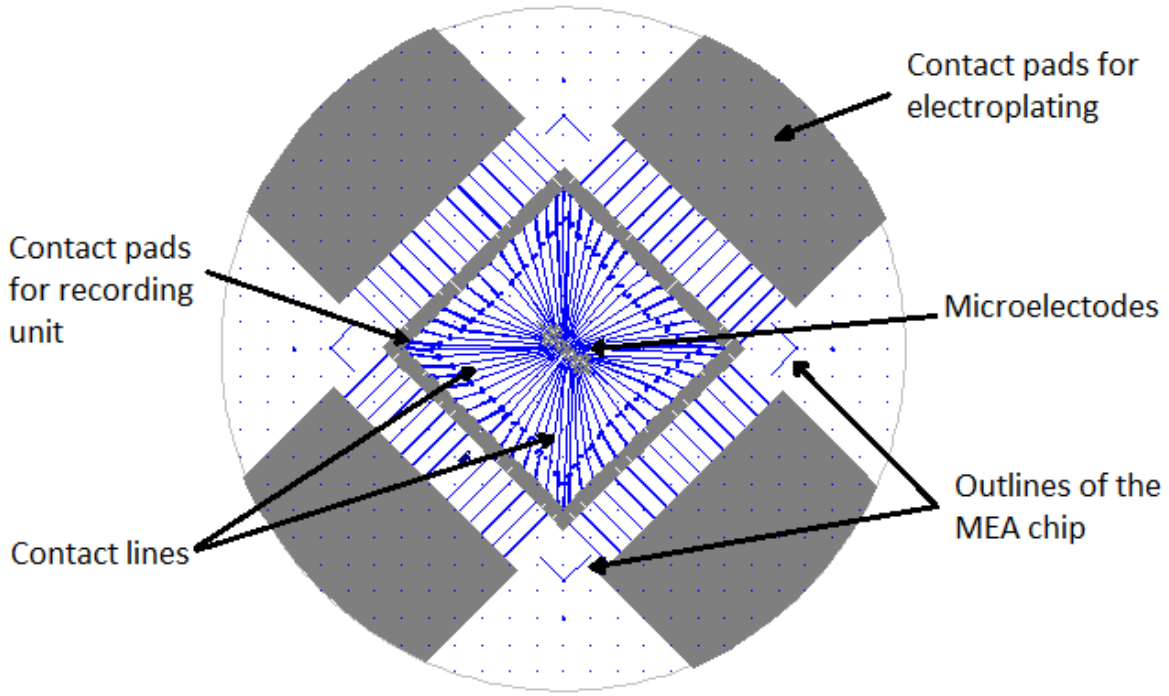

Fig. 27 Design used for fabrication of the metal contacts. The metal contacts exposed after etching are colored in gray. The metal contacts protected with a passivation layer are colored in blue. Design provided by Nicolai Winter-Hjelm.

Different designs of the metal connections, according to the size and number of the electrodes, were tested (see Fig. 28 and 29). Reproducible results are obtained for underlying metal contacts wider than the electrodes (with up to 10um) as this assures a more even surface for the electroplating sites and allows for a certain degree of misalignment between the first and second exposure (see Appendix A3, Fig. 4).

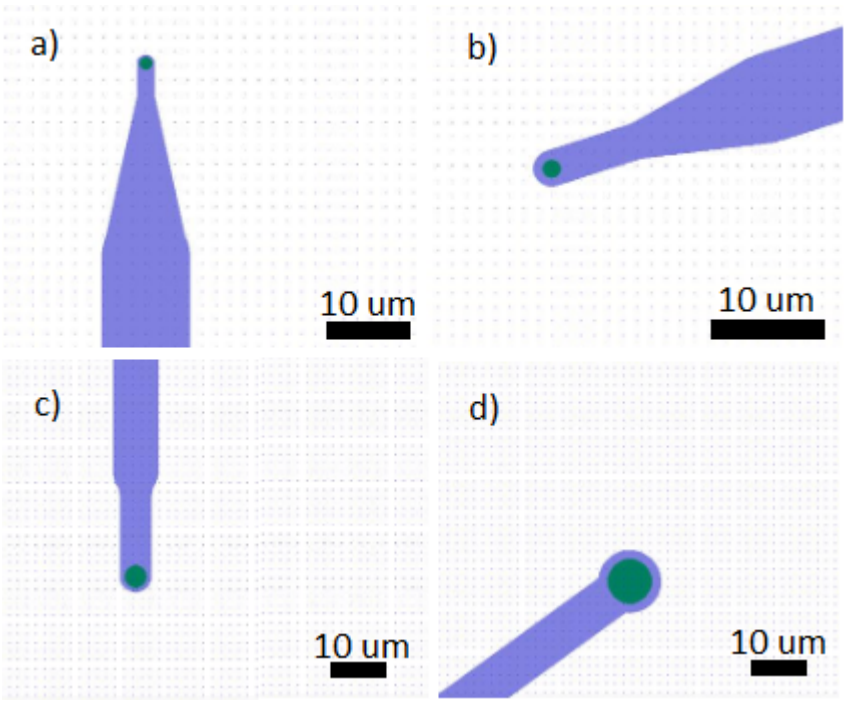

Fig. 28 Design of the metal contacts according to the size of the electrodes. Diameter of the electrodes (in green): a)1um b) 2um c) 5um and d) 10um.

3.1.3 Etching

After deposition of the passivation layer, a second lithographic step was used to determine the exposed metal contacts. This includes the electroplating site where the electrodes were grown, shown in gray in Fig. 29, and the contact pads shown in gray in Fig. 27. Fluorocarbon gasses CHF3 at 50.0 sccm, CF4 at 10.0 sccm, as well as O2 at 7.0 sccm, were used to etch away the Si3N4 layer above the metal contacts in ICP-RIE Chiller system from Oxford instruments. The release step was set to 6 min. 30 sec. at 20 ^{0}C .

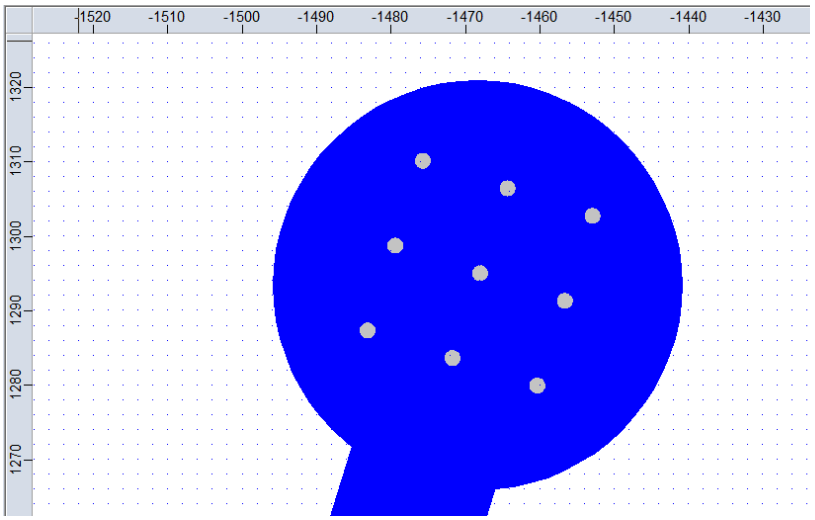

Fig. 29 Design of the mask for exposure of the first (blue) and the second (gray) layers of photoresist to determine the metal sites for electroplating. The diameter of the electroplating sites is 2 microns and the diameter of the underlying metal contact is 50 microns. The scale bars of the image are in microns.

3.1.4 Electroplating

The system used in the project is Silicon Wafer Plating electroplating Laboratory system (PP-type) from Yamamoto and includes a bath, a pump, an agitator, and a thermoregulation unit. Electrodeposition of platinum was done in hexachloroplatinic acid (from Sigma Aldrich) bath with a concentration of 2.5 mM, a temperature of 30 ^0C, and agitation of 60 rpm. The measurements during deposition are done with three electrodes set up: counter and working Pt-electrodes, and reference Ag/AgCl-electrode using PalmSense4. A constant voltage of 0.05V was applied for 10 min at each of the four contact pads at the periphery of the sample (see Fig. 27).

3.1.5 Bonding to PDMS chip

After the growth of the 3D electrodes, the MEA underwent cutting, cleaning, and bonding to a PDMS chip (see Fig. 30). The PDMS chip serves to confine the cells in the area of the recording. The sample was cut with Wafer saw Disco DAD and subsequently cleaned in a photoresist remover mr-Rem 660, acetone, ethanol, and DI water before plasma cleaning and thermal bonding to a PDMS chip. Both the MEA and the PDMS chip were treated with oxygen plasma for 1 min. at 100W and 100 sccm O2 at 0.34 mbar before bonding. The Chip was aligned with the MEA under an inverted microscope after which the bonded device was heated for 60 sec. at 95 ^0C.

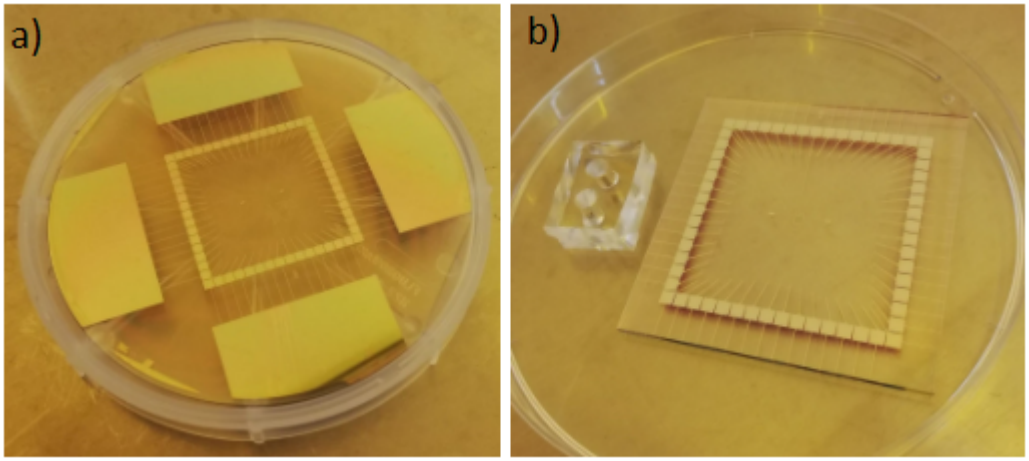

Fig. 30 a) Image of the sample before cutting. b) The cut sample with the PDMS chip before bonding.

3.2 Characterization

3.2.1 Mechanical profilometer

A mechanical profilometer Dektak 150 from Veeco with a 12.5 um diamant tip was used in this project to measure the film thickness of a photoresist for different resists, exposure doses, and development times. The scan length was up to 2000 um with a vertical resolution of 1 Å at a range of 6.55 um. The data was used to determine development rates of resist and to find the optimal parameters for the subsequent process requirements.

3.2.2 Optical microscope

An optical DIC microscope Carl Zeiss AxoScope A1 was used during and after the steps of fabrication for quick evaluation of the results. Investigated were the quality of the developed film, the adhesion of the deposited metal to the substrate, the electrodeposition of platinum, and the stripping of the resist at the end of fabrication.

3.2.3 Optical profilometer

An optical profilometer Contour GT-K from Bruker was used to evaluate the roughness of the platinum depositions and to obtain 3D images of the electrodes. PSI and VSI modes were used. The vertical resolution is sub 1 nm, and lateral resolution depends on the objective used. The optical profiler is equipped with 2.5x, 20x and 50x objective lenses, and with 0.55x and 2x zoom lenses. The software of the instrument was used to model a 3D representation of the electrodes and to measure the rate of deposition of platinum for depositions with a constant current.

3.2.4 Scanning electron microscope

SEM Apreo from FEI was used to obtain detailed images of the platinum depositions morphology for different currents and potentials applied to make the electrodes. SEM was used in three different modes: Standard, OptiPlan, and Immersion with detection of secondary electrons. The acceleration voltage for the electron beam was set to 2 - 5 kV and the current from 0.13 pA to 0.8nA. Images of the electrodes were taken at 0, 55, and 60 degrees angles of the sample stage.

3.2.5 Electrochemical characterization

For the electrochemical characterization, PalmSens 4 from PalmSens BVwas used with a three-electrode cell configuration where the microelectrodes were connected individually as the working electrode, a counter electrode - platinum plate for sweep voltammetry and pulsed amperometric deposition, and a platinum wire for impedance spectroscopy, and an Ag-AgCl as the reference electrode.

Pulsed amperometric detection in 2.5 mM hexachloroplatinic acid with a duty cycle of 50%. (step from 0 to 0.7V for 1 sec.) was performed to test for diffusion limitation of the process of deposition. Linear and cyclic sweep voltammetry were used to scan the applied current versus voltage in the range from -5 to 5V with a step of 0.1V and from -0.5 to 0.7V with a step of 0.01V.

The electrochemical behavior of microelectrodes in PBS (10 mM) was studied by electrochemical impedance spectroscopy (EIS). The impedance was measured in a frequency range from 1 Hz to 10 kHz by applying a square wave signal with an amplitude of 100 mV.

Chapter 4

Results

In this chapter, results from the optimization of the fabrication and characterization of MEAs will be presented. First, results from the optimization of spin recipes to achieve the desired photoresist thickness are presented in section 4.1. In section 4.2 are presented results from the optimization of exposure dose and development time as well as the designs used to obtain these results. In section 4.3, the optimization of the design for electroplating tests is presented. Section 4.4 shows results from the electrochemical characterization of the electrodes and section 4.5 shows results from electroplating.

4.1 Optimization of spin recipes

The thickness of three different photoresists at varying spin parameters was measured with a refractometer and mechanical profilometer to find spin recipes for thickness of the film of 3, 2, and 1 micron. The thickness of the film will determine the height of the stalks of the mushroom-shaped electrodes and is therefore important to achieve fine control of this parameter. The photoresists that were tested are: ma-N 440 for a dependence of the thickness on spin time, and AZ 5214E and SPR700 for a dependence of the thickness on spin speed. The collected data is shown in Appendix A2. The resists were chosen based on the range of thicknesses that can be achieved with each of them.

Calculations based on the formulas for thickness versus spin-speed (see section 2.3) were compared to the measurements presented in Appendix A2. The results agree with the theory within ~ 2 nm for changes in speed in the range of several hundred rpm. The spin-speed needed for desired thickness is then calculated for each of the resists as follow:

1. ma-N 440, 3μm: 6944 rpm for 30 sec at 1000 rpm/s
2. AZ 5214E, 2 μm: 2610 rpm for 30 sec at 500 rpm/s
3. SPR 700, 1μm: 3533 rpm for 34 sec at 1000 rpm/s

4.2 Optimization of exposure dose and development of ma-N 440

The aim of optimizing the process parameters for ma-N 440 was to develop the smallest micro-holes achievable with MLA 150 for a given thickness of the photoresist. This is done by testing designs of masks with different patterns, shown in section 4.2.1. Process parameters such as exposure dose and time of development were examined in a wide range to determine the changes in the resist they lead to. Results from measurements are shown in section 4.2.2. Tests of the exposure dose above deposited metal and passivation layer are

conducted to account for reflectivity from the metal surface when exposing the resist for MEAs fabrication, shown in section 4.2.3. Last, few general conclusions for the behavior of the resist are summarized in section 4.2.4.

4.2.1 Designs of test samples

Glass coverslips were used as a substrate for test samples for optimization of the exposure dose. The goal was to find the optimal exposure dose for feature sizes at the limit of the maskless aligner which is 1 um. Series of exposures were performed on each of the samples in the range of 200 - 4500 mJ/cm2 with steps of 50, 200, and 500 mJ/cm2.

The thickness of the photoresist for each exposure dose is measured every 15 sec. of the development (in developer ma-D 332/S) with mechanical profilometer Stylus, results shown in Fig. 31. This data was used to determine the development and dark erosion rates of photoresist ma-N 440 for exposure doses in the range of 400-2500 mJ/cm2. Results from development of the test samples are shown in Appendix A3.

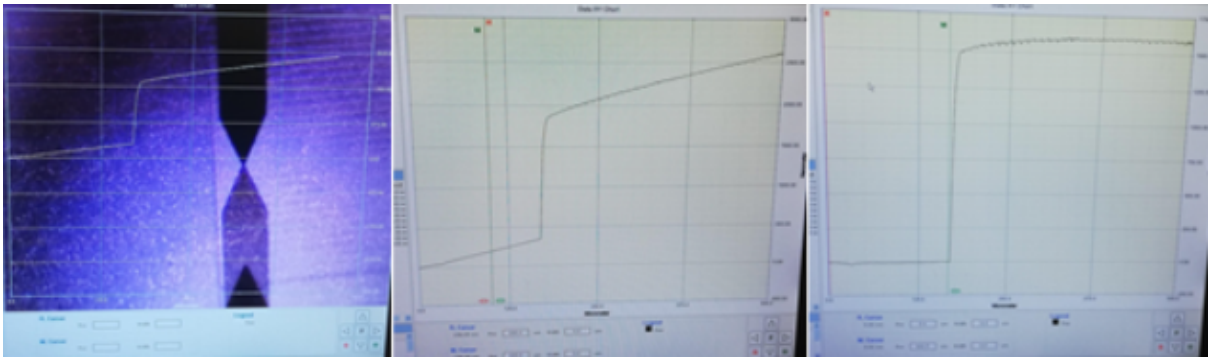

Fig. 31 Results from measuring film thickness with mechanical profilometer Veeco Dektak 150.

The design used to optimize the development time is also shown in Appendix A3, Fig. 1. Different geometries, from 1 to 50 microns, were implemented in the design to examine their effect on the time necessary for the proper development of the features. Furthermore, different designs of the mask were tested (see Appendix A3) to account for specific features of the final MEAs design such as wavy contact lines and their adhesion to the substrate after metalization or to investigate the profile of cylindrical holes in the photoresist.

4.2.2 Development time and dark erosion

The performance of the resist exposed with 1000 mJ/cm2 (recommended dose in the datasheets for the chosen 3 um thickness of the film) for different feature sizes is examined.

The average rate of dark erosion was measured for different exposure doses. Plot with the results is presented in Fig. 32.

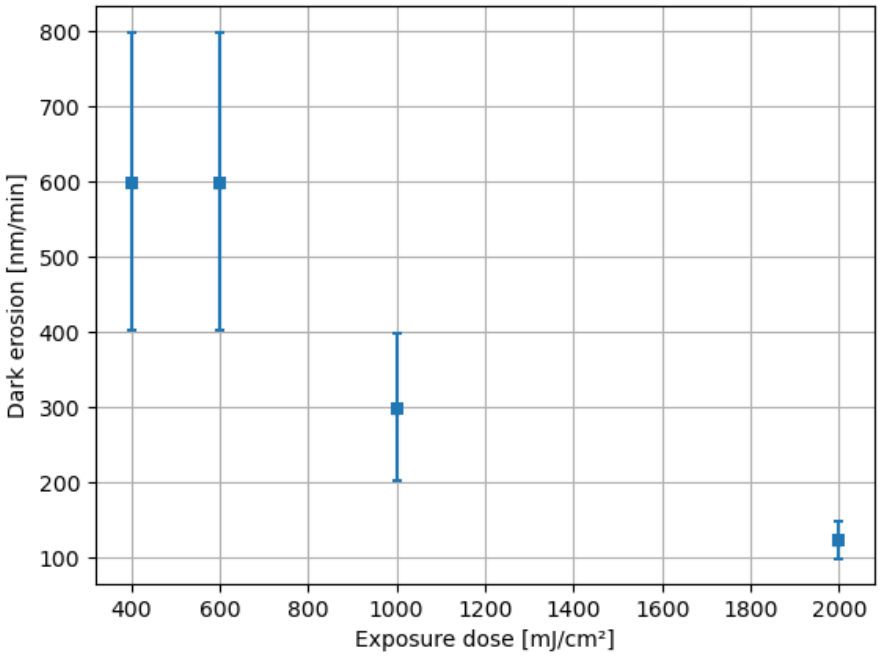

Fig. 32 Plot of dark erosion rates for photoresist ma-N 440 versus exposure dose.

This data was obtained by measurements of the film thickness every 15 sec. for exposure doses from 400 to 4500 mJ/cm2 and time of development from 2 to 9 min. It was observed that the rate of erosion increases when the thickness of the remaining film decreases. When the thickness reaches 1000 nm, the quality of the remaining film starts getting compromised. The film becomes semi-transparent and unevenly dissolved by the developer with defects in the structure of the film in order of 50 - 100 nm that starts being visible - the interference of light creates visible fringes giving a colorful topographic map off the resist surface and measurable - irregularities of 20 - 50 nm were measured along the resist surface with Veeco profilometer.

4.2.3 Metal deposition tests

Thin-film metal deposition was performed on samples to determine whether the development time was sufficient or not and to conclude whether the red color observed with an optical microscope in the middle of the microholes was due to interference of light or due underdevelopment. The results from metalization showed that the coloring is due to interference. A sufficient exposure dose and time of development for ma-N 440 to develop 1 and 2 um microholes were determined:

- optimal for 1um - 800 mJ/cm2 but bigger features (above 10 um) are overdeveloped, 3min 20sec in ma-D 332/S

- optimal for 2um - 1250 - 1450 mJ/cm2, 3min 20sec in ma-D 332/S

Exposure, development, metal deposition, and passivation were performed on two coverslips to test the optimized exposure doses under the condition of an underlying reflective metal layer. This was done to reproduce the fabrication of the MEAs. The optimal dose for developing microholes of 2 um in diameter in these conditions is found to be 800 mJ/cm2. For holes of 1 um in diameter no parameters that give reproducible results were found. This is due to limitations of the resolution of the MLA and a higher degree of crosslinking above the underlying metal layer which will be discussed in Chapter 5. Designs of the masks used for this experiment are shown in Appendix A3, Fig.2 (second row).

4.2.4 Additional conclusions from tests and measurements:

- The thickness of the spun film on glass vs. on silicone is 2900 vs. 2960 nm (measured after soft bake and before exposure). Measurements from the two instruments, Stylus and refractometer, coincide. The optimized spin recipe is giving reproducible results.
- For exposure doses above 2500 mJ/cm2 the process of crosslinking saturates, giving the same thickness as the measured before development - 2900 nm, showing that the maximum thickness for the given spin recipe is reached for exposure doses above twice the recommended and that the dark erosion is significantly reduced for such high doses.
- Overdevelopment of the bigger features is present when dissolving small features - 1 and 2 um that need more time of development. This leads to a decrease in the film thickness due to dark erosion (for recommended exposure doses). A possible solution is to use different exposures for different feature sizes.
- Tests showed that an exposure dose of 800 mJ/cm2 and 2 min - 2 min 25 sec.of development is optimal for developing 1 and 2 um features and gives a thickness of 1750 nm. Besides the dark erosion, another process that can influence the resist thickness after exposure is etching. Measurements of the thickness after etching show that the resist thickness decreases with 400-500 nm.

4.3 Optimization of design for test samples

For this project, a total of 11 samples, each with 20 contact pads and 5 electrodes connected to each contact pad were tested. The size of the electrodes was varied to test if this will alternate the process of deposition and the resulting morphology. There was no difference found indicating that the process of deposition does not depend on the area for deposition as long as that area is considerably bigger than the hydrodynamic radius of the ions and the local irregularities of the ionic atmosphere of the electrolyte. The sizes tested are 100um, 50um, 10um, 5um, and 2um. An overview of the design that was used to fabricate the test samples is shown in Fig. 33. A radial symmetry for grouping the electrodes on the 4-inch substrate

was chosen to use the maximum of the available space. The connections between the contact pad and the contact line are smoothened to avoid charge accumulation around corners. Above the contact pads, the second layer of the mask does not completely overlap the first layer in order to protect the edges of the pad with the passivation layer. On each pad, five electrodes are connected in order to investigate eventual differences in the deposition with constant voltage due to the imperfection of the metal connections. Design with one electrode per contact pad was also tested but proved to be not reliable due to the higher chance for defects that can not be directly compared with other electrodes with the same parameters of deposition.

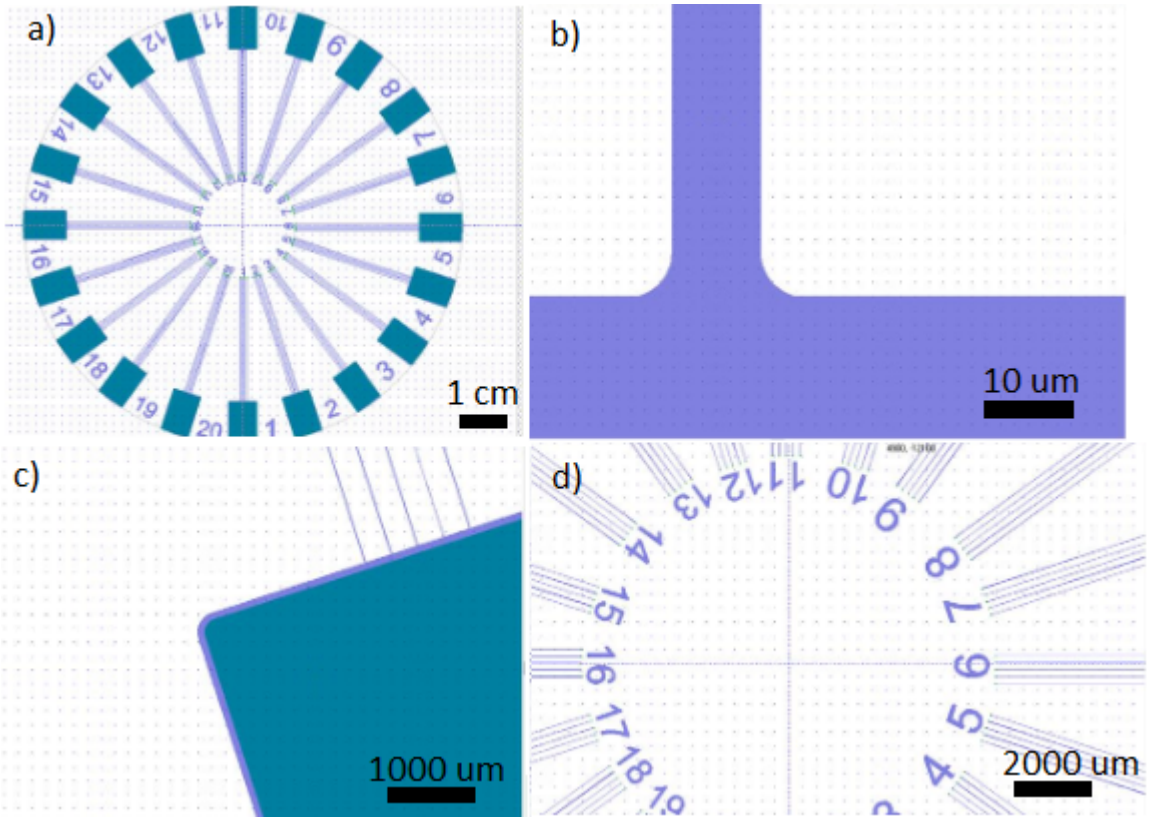

Fig. 33 Overview of the design used for fabrication of the test samples. a) and d) A radial symmetry for grouping the electrodes on the 4-inch substrate was chosen to optimize the use of the available space. b) The connections between the contact pad and the contact line are smoothened to avoid charge accumulation around corners. c) The second layer does not completely overlap the first one (above the contact pads) in order to protect the edges of the pad with the passivation layer.

4.4 Electrochemical characterization

4.4.1 Pulsed Amperometric Detection

Pulsed amperometric detection was performed on a 100um electrode to examine changes in the detected current. The measurement of the current was done while the electrode is under the applied voltage, in this case - $E_{applied} = 0V, \eta = 0.7V$ for 1 sec. When the voltage drops to the base value, in this case - $E_{applied} = 0.7V, \eta = 0V$ for 1 sec, no current was measured. Changes in the measured current can reveal information about the dependence of the reduction on the diffusion of ions at the proximity of the electrode. A result from the performed PAD is shown in Fig. 34. The current stays stable during the measurements which shows that the reaction at the electrode is not diffusion-limited. The active surface area during deposition increases, allowing for more ions to be reduced which leads to a slight increase in the absolute value of the measured current.

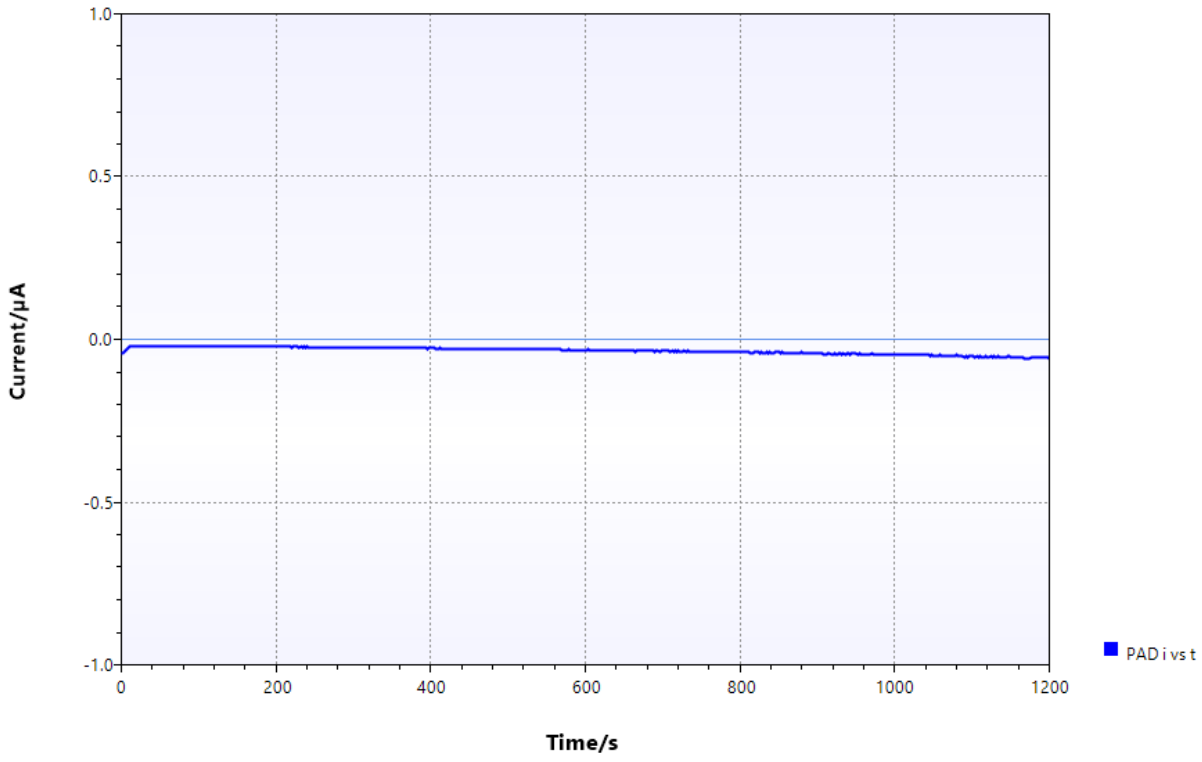

Fig. 34 Plot of the measured current vs. time during PAD is shown. The measurement is done for 1200 sec. , pulse: 1 sec. at 0V and 1 sec. at 0.7V. The monotonic change in the current is due to an increase in the active surface area for deposition. Lack of oscillations in the current between the pulses shows that the rate of reduction is not diffusion-limited.

4.4.2 Cyclic voltammetry

Cyclic voltammetry on 100 um electrodes is performed from -0.5 to 0.7V with a step of 0.01V/s and from -5 to 5V with a step of 0.1V/s. The purpose of obtaining voltammograms is to acquire information for the rate of the reaction at the electrode, given by the measured current, for a range of applied voltages. This gives information for the processes that occur both at the cathode and the anode. Voltammograms of the two baths used in this project are obtained and compared (shown in Fig. 35). Fig. 35 a) presents the results from two cyclic sweeps performed in a bath with 2.5 mM hexachloroplatinic acid, b) presents the same sweeps done in a bath with 2.5 mM hexachloroplatinic acid and 1.5 mM formic acid. The current values measured for each bath coincide showing that adding formic acid does not have a pronounced effect on the reaction for the given range of potential sweeps.

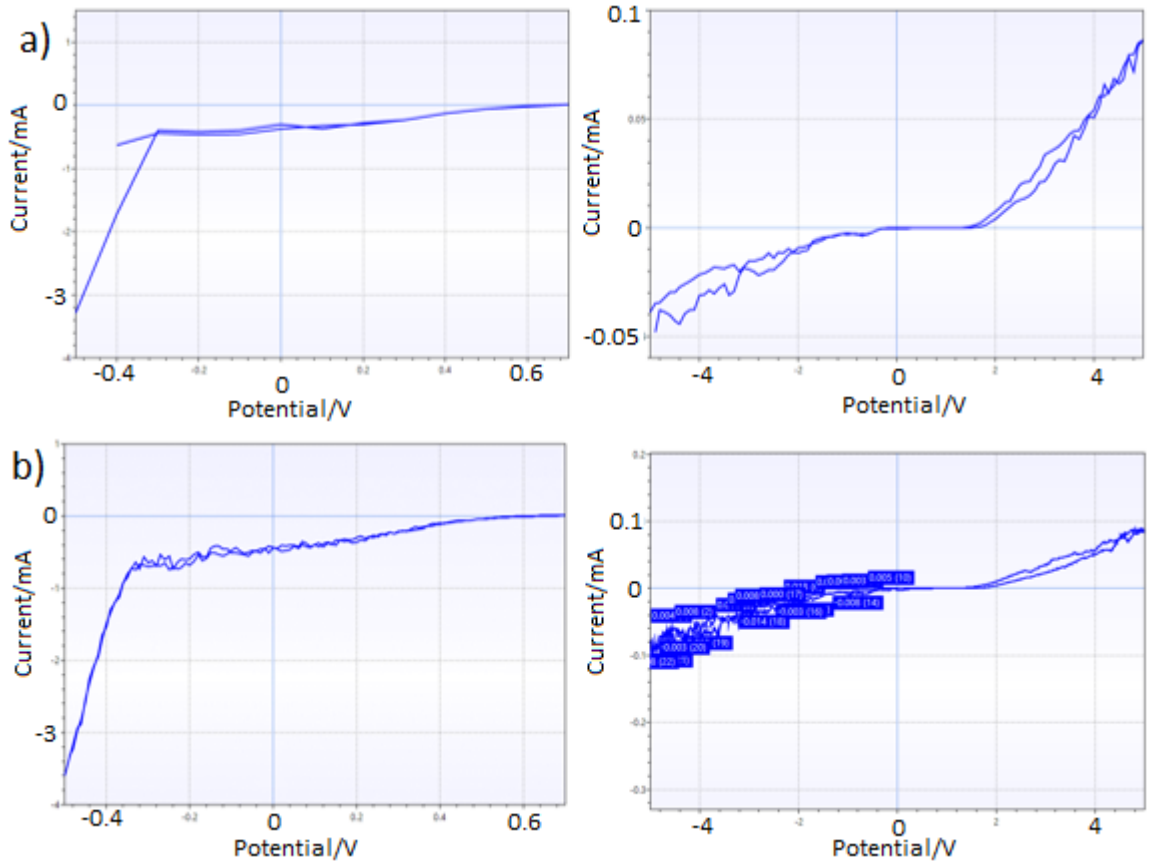

Fig. 35 Cyclic voltammograms for two electrolyte baths: 2.5 mM hexachloroplatinic acid (first row) and 2.5 mM hexachloroplatinic acid and 1.5 mM formic acid. The first images show voltage sweep from -0.5 to 0.7V, the second - from -5 to 5V. The current values are similar for both baths showing that the rate of the reaction is not affected by the given changes in the electrolyte.

4.4.3 Impedance measurements

Impedance measurements are done in 0.01 M PBS solution in a frequency range from 1 Hz to 10 kHz by applying a square wave signal with an amplitude of 100 mV. The measurements were done after deposition to evaluate the quality of the final electrodes. A plot of the results is shown in Fig. 36. For 100 Hz to 1000 Hz, the measured impedance is 0.2 MΩ to 0.9 MΩ which is a good range for detecting signals from neural activity. Measurements of the impedance with 50 um plain Pt-black electrodes, successfully used in previous projects and research activities, were conducted. The resulting impedance has the same values across the frequency range as for the much smaller 3D electrodes. However, the 3D electrodes are grouped in nine which increase the total surface area per electrode**.**

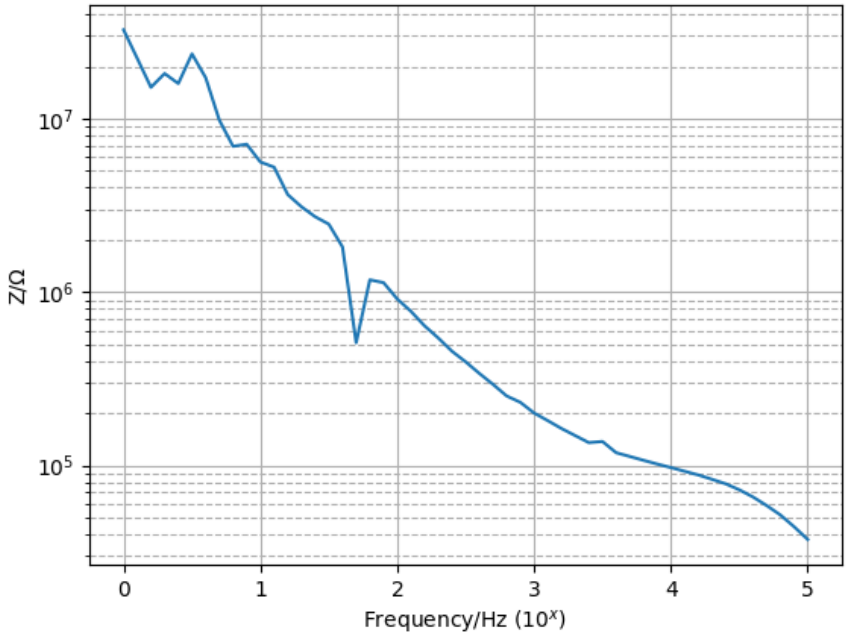

Fig. 36 Plot from EIS measurements shows the impedance versus frequency in the range of 1 Hz to 10 kHz. The measured values are comparative to the performance of the more common plain MEA for extracellular recordings.

4.5 Electroplating of platinum

Potentiostat PalmSense4 with constant current and constant voltage modes was used in this project to examine the effect of the following parameters on the morphology of the depositions of platinum:

Mode	Features of deposition
Constant current [nA/um2]	
1	very slow, even deposition, no edge defects
50	10nm/min, even deposition, no edge defects
100	20nm/min, even deposition, no edge defects
200	80nm/min, even deposition, no edge defects
400	very porous, edge defects
Constant Voltage [V]	
-0.5	very porous, no edge defects
-0.4 to -0.1	porous, edge defects
-0.05, 0, +0.05	less porous, edge defects
0.1 to 0.3	even deposition, no edge defects
0.4 to 0.7	slow to no deposition, no edge defects

Table 1. Range of tested parameters with constant current and voltage modes.

The choice of these parameters was based on an investigation of results from previous studies. The aim was to understand the electrodynamics of the process of deposition and to find what parameters are needed for even growth. The parameters were tested first in a bath consisting of an aqueous solution of 2.5 mM chloroplatinic acid (H_2PtCl_6, 8wt% in H_2O from Sigma-Aldrich) and 1.5 mM formic acid (HCOOH, 95% from Sigma-Aldrich). The depositions done in this bath with constant voltage mode were compared to depositions in a bath with 2.5 mM of chloroplatinic acid and no formic acid. Current measurements and results from deposition show no differences between the two baths indicating that the formic acid does not play a significant role in contributing to the deposition as expected. This was proven by performing pulsed amperometric detection (PAD) results of which are presented later in this Chapter. Results from depositions with constant current and constant voltage modes are provided below.

4.5.1 Constant current

Depositions with a constant current supply at the cathode are conducted to analyze changes in the morphology. The parameters to be considered were the current density and the voltage

limit. The tested current density range was 1 to 400 nA/um2 at voltage limits set to 0.7, 1, or 40V. These values for the voltage limit were chosen because 0.7V is the standard electrode potential for platinum, 1V was chosen to investigate for eventual differences in the deposition near the standard potential, and 40V was chosen as a limit that can not be reached with the currents used and therefore acts as a parameter that does not limit the deposition.

For current density of 1 nA/um2 (see Fig. 37 a) and Appendix A4 for more detailed images), the rate of reduction is low, resulting in a deposition of a thin layer of platinum which quickly delaminates, possibly due to the air gun used to dry out the sample after deposition. Depositions with current densities of 4, 8, 20, and 40 nA/um2 were also conducted. They as well showed a low rate of deposition.

Depositions with current densities of 50 and 100 nA/um2 were tested (see Fig. 37 b) and c) and Appendix A4) and the rate of the deposition in nm/min was assessed by comparing the data from the optical profiler before and after deposition. The average rate of deposition for 50 and 100 nA/um2 was 10 and 20 nm/min, respectively.

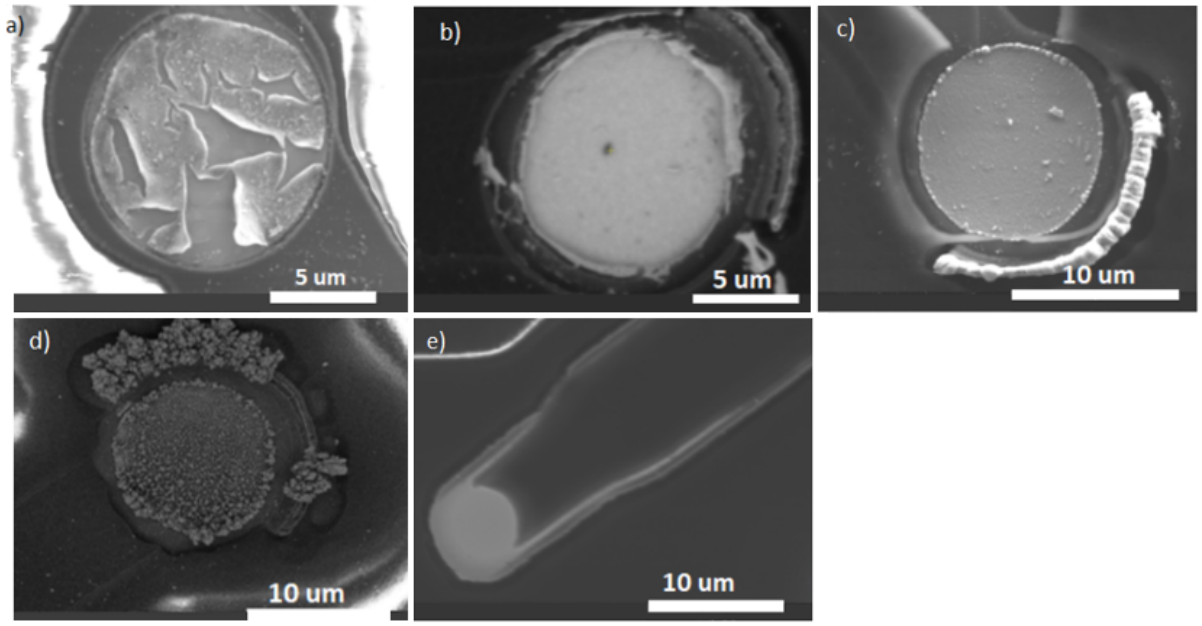

Fig. 37 SEM images of depositions at a) 1nA/um2, b) 50 nA/um2, c) 100 nA/um2, d) 400 nA/um2, limit 40V, and d) 400 nA/um2, limit 1V

In Fig. 38 are shown two 10um electrodes with depositions performed at 200 nA/um2 with a voltage limit of a) 40V and b) 1V. This value for the current density showed to be optimal with regard to the purpose of growing 3D microstructures by means of deposition. The pronounced benefits are even deposition, no edge defects, faster rate (80 nm/min).

Control of the smoothness can be achieved by controlling the voltage limit of the potentiostat. A lower voltage limit leads to a smoother deposition without altering the rate of deposition as long as the limit does not go below the potential equilibrium of the metal, 0.7V for platinum.

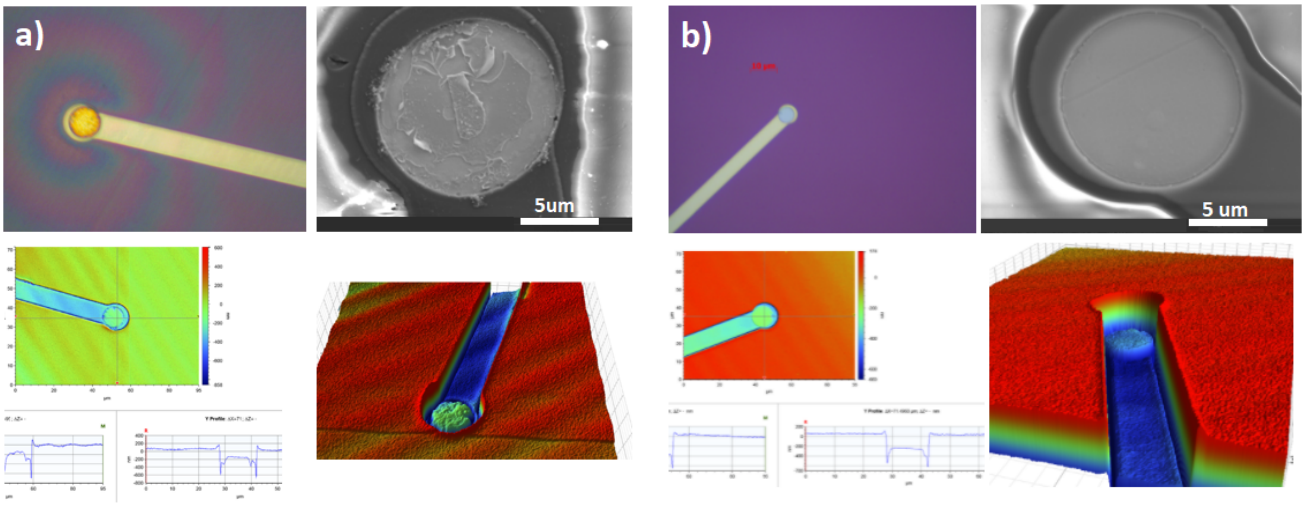

Fig. 38 Deposition on 10 um electrodes with 200 nA/um2, a) limit voltage 40V b) limit voltage 1V . Images were taken with an optical microscope (up left), SEM (up right), and optical profiler (second row). Smoother platinum deposition occurs at lower voltage limits. The rate of deposition, 80 nm/min, does not change when applying the lower limit. No edge defects are observed for all depositions at this value for the current density.

On two electrodes, 5 and 10 um in diameter, a deposition was performed at 400 nA/um2 with a different voltage limit - 40V for the 10 um electrode and 1V for the 5 um electrode (see Fig. 37 d) and e) and Appendix A4). Experiments were conducted prior to this deposition to investigate the effect of the size of the electrodes on the morphology of the deposition. It was found that sizes in the range of 1 to 100 um do not alternate the mechanism of electroplating, the resulting morphologies, and the presence of edge defects. The results from imaging the electrodes show that for current densities higher than 200 nA/um2 the deposition of platinum becomes porous when the voltage limit is high enough to not suppress the reduction. For lower voltage limits (close to the potential equilibrium of the metal deposited) the reduction is suppressed enough to significantly alternate the morphology.

4.5.2 Constant voltage

Depositions at constant voltage were performed for the range -0.5 to 0.7V with a step of 0.1V. The resulting platinum layers were investigated with an optical microscope, SEM, and optical profiler (see Fig. 39) to find parameters that produce plain deposition with less pronounced edge defects. Depositions in the range from -0.5 to -0.3V are shown in Fig. 40. Plots of the current measured at the electrode versus time of deposition (10min) is also shown. The current is a direct measure of the rate of the reduction reaction from which the amount of reactant and the height of the deposition can be calculated as shown in Chapter 2.

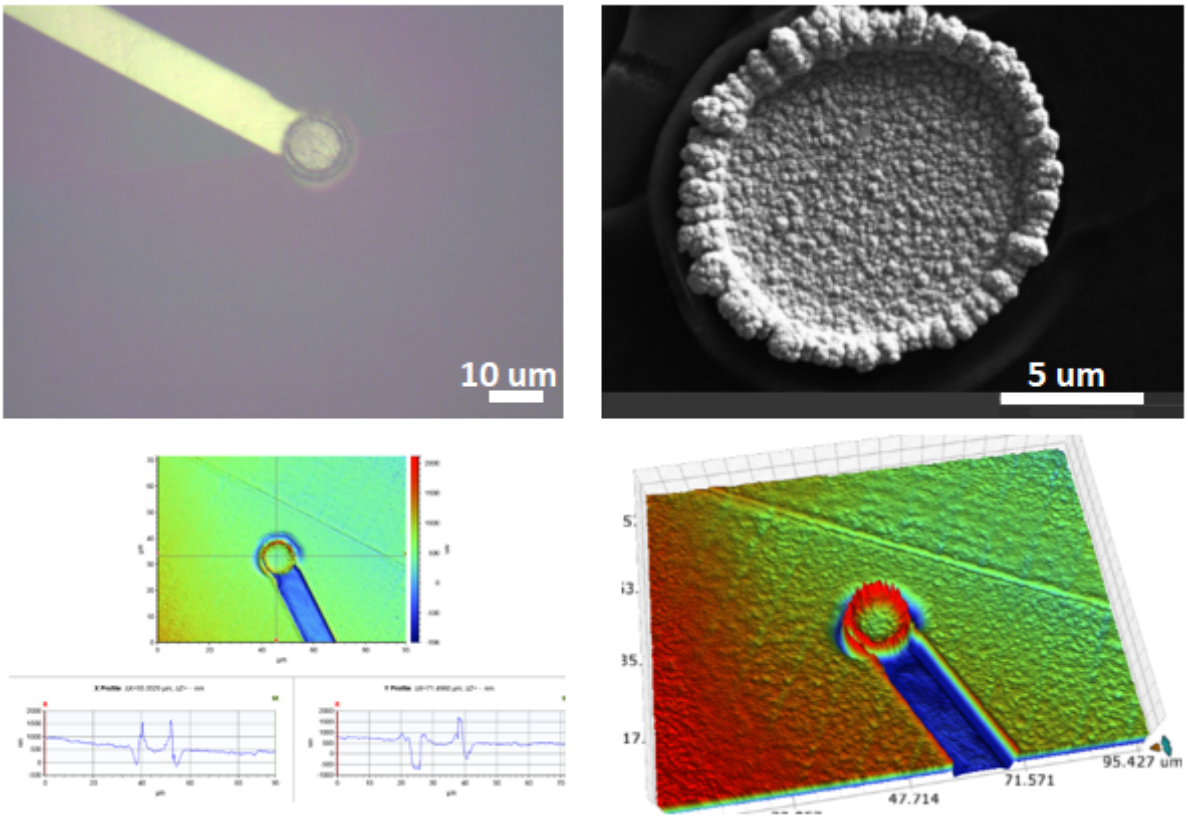

Fig. 39 Images of electrodeposition at -0.1V obtained with an optical microscope, SEM, and optical profiler. Edge defects are present for depositions at -0.4 to -0.1V.

For applied -0.5V the deposition is highly porous and without edge defects. For voltages up to -0.1V the depositions are porous with edge defects. Decreasing the overpotential ($\eta = E^0 - E_{applied}$) by alternating the applied voltage towards the equilibrium potential E^0 for platinum, results in less porous to flat depositions and less to no edge defects. The rate of the reaction approaches zero for applied voltage $E_{applied} \geq 0.3V$, $\eta \leq 0.4V$. Therefore, the interval $-0.1V \leq E_{applied} \leq 0.3V$ contains the values for the applied voltage at which even layers of platinum can be deposited onto the electrodes. The rate of the reaction is highest at -0.4V, approaches zero for $\eta \rightarrow 0$(see Fig. 41), and is given by the equation:

$$\frac{dN}{dt} = \frac{i}{n.F}$$

, where N is the amount of reactant in moles, $i$is the measured current, $n$gives the number of electrons needed to reduce one platinum ion to an atom, and $F$is Faraday's constant.

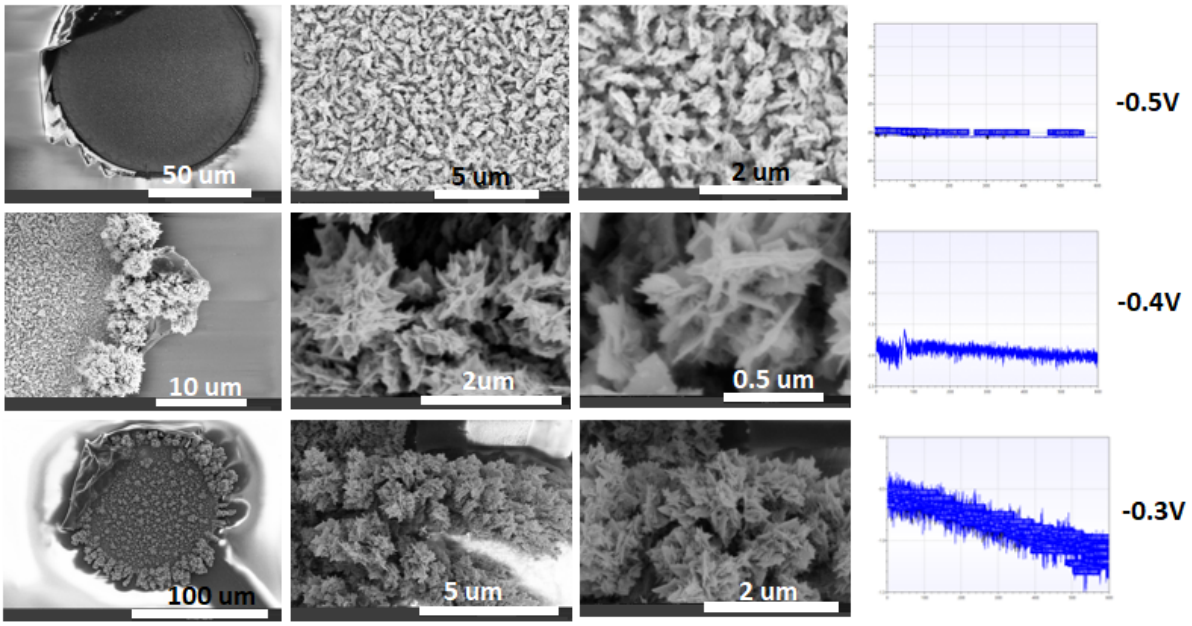

Fig. 40 Sem images of 100um electrodes after 10min of deposition at -0.5,-0.4, and -0.3V. Formation of porous structures with pronounced edge defects is present for values of the applied voltage up to -0.1V. The I vs.t diagrams show the measured current during deposition giving the rate at which the reactant is consumed in the reduction reaction.

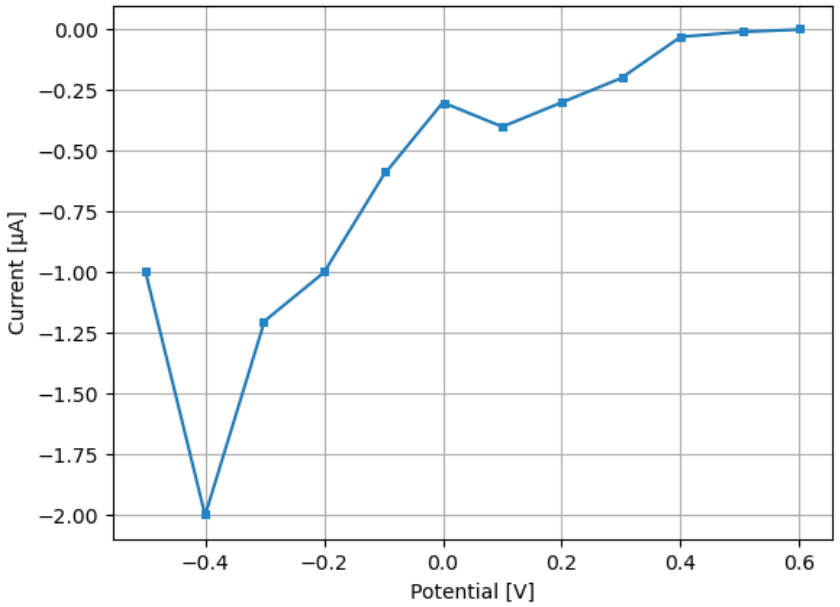

Fig. 41 The average current measured at 100 um diameter electrodes for applied voltage from -0.5 to 0.7V.

SEM images from depositions at 0.1, 0.2, and 0.3V Can be found in Appendix A5 with the respective I/t plots. The observed delamination of the deposited layers at 0.1 and 0.2V is discussed in Chapter 5.

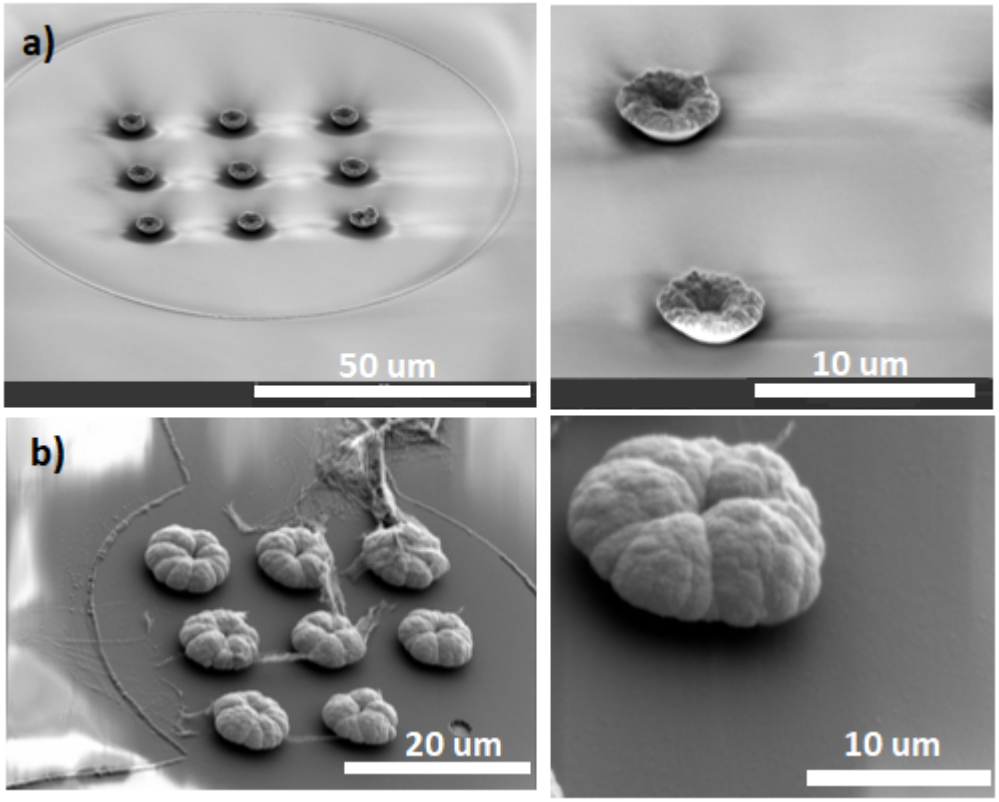

Fig. 42 SEM images of electrodeposition of platinum at a) 30 ^0C and b) 40 ^0C temperature of the electrolyte. Images are tilted at 50 ^{0}to the surface of the sample. The higher temperature of the electrolyte increases the ion mobility leading to a faster rate of deposition.

The difference in the deposition at 0.05V for a temperature of the bath 30 and 40 degrees is shown in Fig. 42. The time of deposition is 10min. For higher temperatures, the mobility of the ions increases and this leads to higher rates of deposition with more even distribution of the reduction at the interface electrode-electrolyte. The caps of the 3D mushroom-shaped electrodes deposited at 40 ^0C are considerably bigger, d=10um, with a hemispherical shape while the ones deposited at 30 ^0C have rather a conic shape and smaller diameter of 4-5um.

Depositions for 10min at 0.05 and -0.05V and standard temperature of 30 ^0C are shown in Fig. 43. The characteristic transition from porous to even deposition when switching from negative to positive $E_{applied}$, observed in previous measurements (see Fig 40 and Appendix A5), is also pronounced for smaller deviations from $E_{applied} = 0$, in this case, for $\Delta = \pm\ 0.05V$.For the fabrication of the 3D MEA for this project the applied voltage is chosen to be 0.05V due to biocompatibility considerations regarding the roughness of the caps at -0.05V, results are shown in Fig. 42 a) and 43 a). The diameter of the stalk is 2um and

the diameter of the cap is 5um. The second parameter $E_{applied}$ = -0.05V is potentially beneficial to be used as it has a bigger surface area and will increase the SNR of the recordings. However, the effects of such pronounced roughness on the engulfment from neurons are not investigated yet and this leaves an open question.

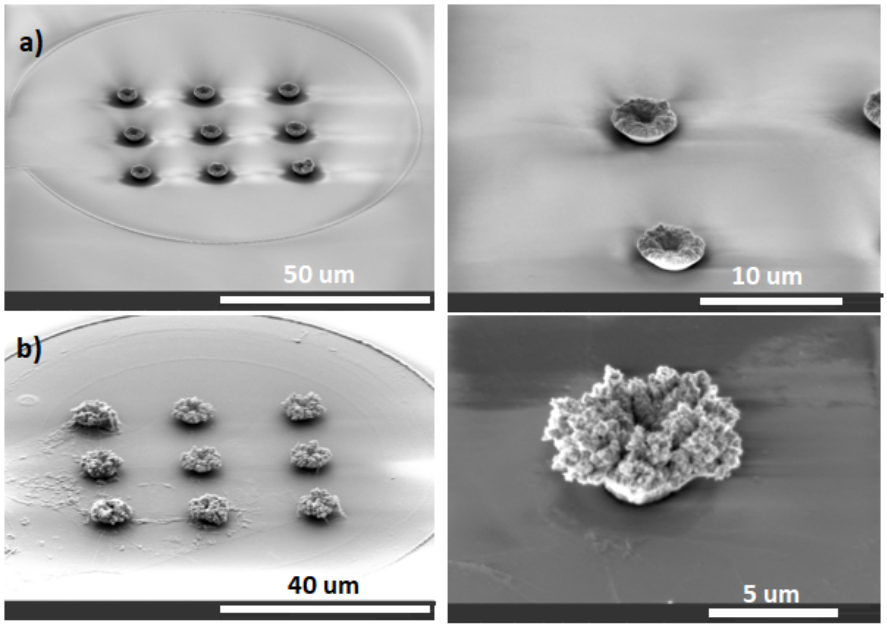

Fig. 43 SEM images from electrodeposition of platinum with constant voltage at a) 0.05V and b) -0.05V.

4.5.3 3D mushroom-shaped MEA

After optimization of the necessary process steps and characterization of the electrochemical deposition described above in this chapter, the parameters chosen for fabrication of the 3D MEAs were determined. For the development of the micro holes in the second layer of resist, which determines the geometry of the stalk of the electrodes, spin-coating with 3000 rpm for 30 sec. at 200 pm/sec. and exposure dose of 800 mJ/cm2 were used to produce vertical 1.75 microns thick sidewalls. Electrochemical deposition with constant voltage at 50 mV for 10 min. was used to develop the platinum 3D mushroom-shaped microelectrodes. The MEA was then cleaned, cut, and bound to a PDMS chip and prepared for cell culturing (see Fig. 44). Protocol with the complete steps of fabrication can be found in Appendix A1.

The prepared chip was seeded with rat primary cortical neurons and astrocytes by Edevard Hvide as part of his master's project. The cell culture was incubated for 2 weeks until the population matured enough to start exhibiting spontaneous activity. Protocol for seeding the cell cultures can be found in Appendix A6. The viability of the cells shows that the the device is biocompatible. Recordings were obtained from Nicolai Winter-Hjelm. Results from seeding and recordings are presented in Fig. 45. There were no distinguishable traits of

intracellular recordings, indicating that the size of the electrodes (caps are 5 um) is too big for engulfment from the neurons. However, prominent extracellular signals were detected, which confirms the functionality of the platform as a recording device.

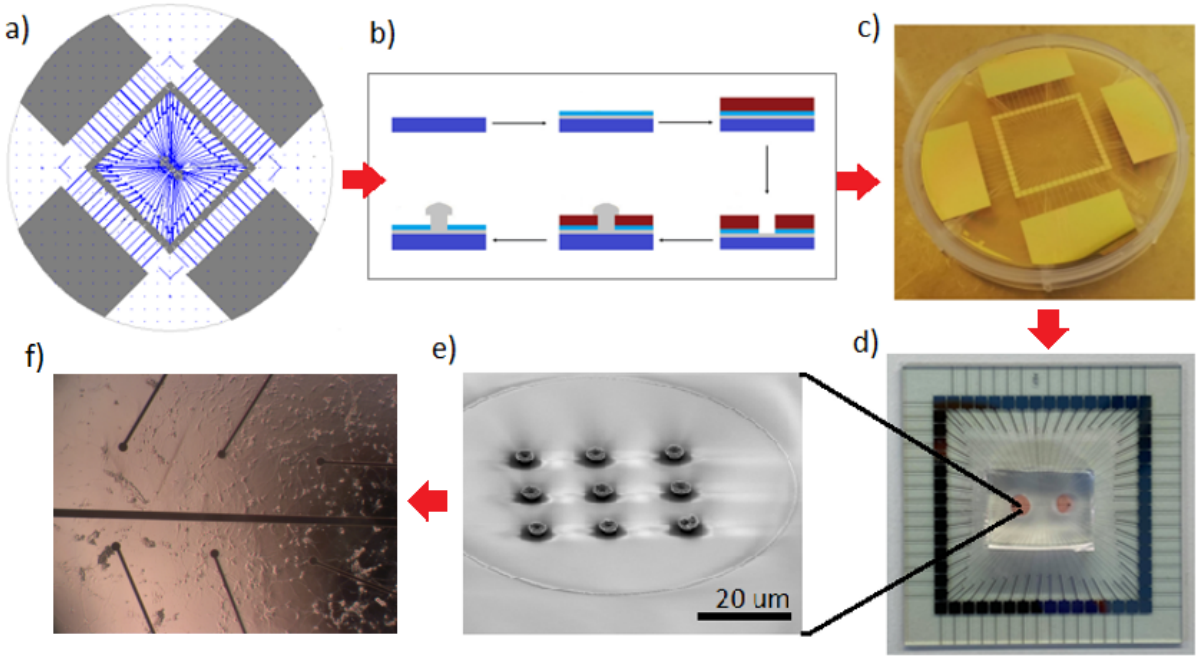

Fig. 44 The process of fabrication of platinum 3D mushroom-shaped MEAs. a) CAD design of the metal contacts and passivation layer. b) Nanofabrication steps by means of photolithography, thin-film deposition, and electrochemical deposition. c) Image of a sample after finishing the steps of nanofabrication. d) Cut MEA bound to microfluidic PDMS chip. e) SEM image of the mushroom-shaped microelectrodes. f) Image of viable neural cell culture above the electrodes, provided from Nicolai Winter-Hjelm.

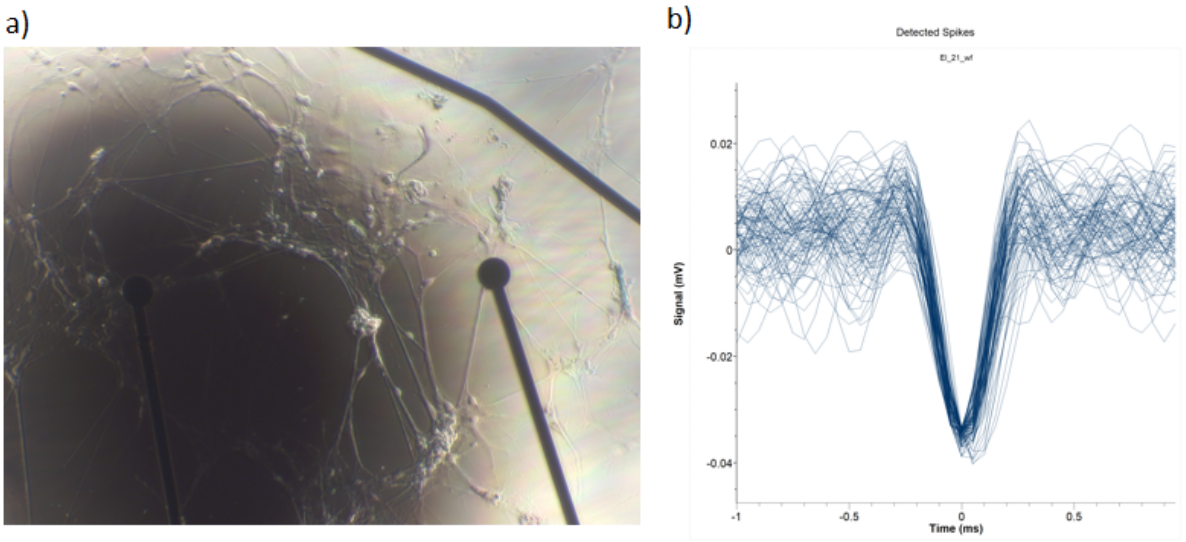

Fig. 45 a) Image of cells growing on top of the electrodes; obtained with an optical microscope. b) Plot of 100 overlaying spikes recorded with 3D MEA. Image and recordings obtained by Nicolai Winter-Hjelm.

Chapter 5

Discussion

In this Chapter, four aspects of the presented project and their perspectives on achieving more controlled Pt deposition and well-defined mushroom shapes with lower impedance will be discussed. The aspects are:

- Limitations of photoresist and MLA 150
- Constant current versus constant voltage
- Temperature of the electrolyte
- Delamination of the deposited layers
- Control of the surface area of the electrodes

The aim is to provide the reader with the most important considerations with regard to improvements in the processes of fabrication of 3D mushroom-shaped MEAs. Discussed are limitations and possible solutions.

5.1 Limitations of photoresist and MLA 150

In this project, the main objective was to fabricate mushroom-shaped microelectrodes small enough to be engulfed by neurons. The size of the electrodes is primarily determined by the size of the micro holes in the photoresists. Limitations for the smallest achievable size of micro-holes are due to the used photoresist and the laser wavelength of MLA 150. For developing small features with an aspect ratio higher than 1:1, a positive resist will be an advantage compared to a negative photoresist where features with sizes close to the minimum attainable resolution of the exposing system will experience parasitic crosslinking in the area of the features due to light scattering and diffraction. The wavelength of the writing laser is $\lambda = 405\,nm$. The limit for the smallest attainable features with MLA 150 is 1 um. For this project, the minimum size that gives reproducible results was 2 um because the underlying reflective metal surface significantly increases the effect of parasitic crosslinking of negative resists.

For positive resists, small features with a high aspect ratio can be developed more successfully because the ratio of dissolution of exposed versus unexposed parts increases with a dilution of the developer. Requirements for a positive resist will be resilience to etching and electroplating which are not commonly fulfilled for this type of resist. Smaller, sub-micron holes can be exposed with an electron beam lithography, and thus smaller 3D electrodes can be fabricated which will increase the chances for engulfment of the electrodes from neurons.

5.2 Constant current versus constant voltage

Results from electrodeposition with a constant current show promising results for current densities of $j = 50 \div 200$ nA/um2. The rate of deposition in this range can be precisely controlled by adjusting the current output and without compromising the uniformity of the deposited Pt film. Considering the resolution of the potentiostat which is several tens of millivolts, such a level of control is not achievable with constant voltage mode. Also, the depositions with constant current do not have edge defects in the aforementioned range for j which makes it a suitable parameter for the formation of smaller, denser, and more stable 3D microelectrodes. However, there are some disadvantages of using constant current. The current can not adjust to the growing electrodes and small deviations in the surface area will lead to changes in the current distribution which will make the process of deposition not reproducible.

5.3 Temperature of the electrolyte

Tests of the effect of changing the temperature of the electrolyte (from 30 to 40 degrees) on the electrode formation show that increasing the temperature helps for more homogenous electrode cap growth. Higher temperatures lead to an increase in the current efficiency of the solution and, as shown in paper [157], the influence of the temperature on the cathodic current is especially pronounced for temperatures above 60 degrees. In other literature and protocols, 70 degrees is recommended for optimal effect during deposition of platinum and 60 degrees for gold. These parameters also were found to be optimal for the formation of hemispherical caps where the ratio of the cap diameter over cap height is strongly dependent on the temperature of the solution.

5.4 Delamination of the deposition at 0.1V and 0.2V

The observed delamination of deposited at 0.1 and 0.2V Pt-lyers can be explained by an accumulation of internal stress during the deposition. The rate of reduction of platinum ions is faster compared to the deposition at 0.3V and this may lead to the formation of disoriented crystal domains in the deposited layer which tend to fall into a local minimum of their potential energy, rearranging the crystal structure of the layer and leading to the observed delamination.

5.5 Control of the surface area of the electrodes

As shown in section 4.5.2, a characteristic change in the morphology of Pt deposition when switching from negative to positive voltage applied is present. The deposition transitions from porous for negative to even for positive voltages. This result is observed both for -0.1V

compared to +0.1V and for -0.05V compared to +0.05V and is one way to control the roughness of depositions with minor changes in the rate of growth. Another way to control the roughness of the resulting structures is to deposit the 3D electrodes at a slow rate and strike them with a short impulse of high voltage or current density. This will deposit a porous layer onto the caps and will increase the surface area, decreasing the impedance, and contributing to better SNR. How the degree of roughness of the surface will affect the process of engulfment is not yet studied. It is known, however, that roughness at different scales can significantly alter the reaction of living tissues resulting in a surface more or less attractive for the cells.

5.6 Size of the electrodes

As mentioned in section 2.2.6, the neurons trigger their mechanisms of phagocytosis when they sense particles below 0.5 um. As reported for structures up to 2.5 um, the process results in partial engulfment [127]. The coupling coefficient of the neuron-electrode system, important for the SNR and therefore for detecting intracellular recordings, is determined by the size, the aspect ratio, and the topography of the microelectrodes. Ways to control these parameters are proposed in the previous sections of this chapter. In this project, due to the limitations discussed in section 5.1, the size of the electrodes was 2 um diameter of the stalks and 5 um of the caps. The electrodes were able to detect extracellular signals with sufficient SNR. However, they did not show signs of intracellular-like spike detection indicating that this size is not sufficient to trigger the process of engulfment.

5.7 Increasing the signal-to-noise ratio

One method to improve the quality of recordings from neural cells is electroporation. This method can increase the SNR by up to 100 fold. Similar to the transfection technique, by which DNA or different molecular carriers are introduced to the cell, the applied electric field changes the membrane potential inducing nanometer-sized pores. When current is applied to the neurons before obtaining recordings, an increase in the permeability of the membrane and its surface area leads to better sealing with the electrode. As described in sections 2.2.5 and 2.2.6, this contributes to better SNR. The degree of improvement in SNR after electroporation may contribute to the detection of intracellular-like signals despite the size of the electrodes. Considering the fact that the neurites are on average 10 um in diameter, the electrodes are small enough to be susceptible to engulfment when the process is externally stimulated.

Bibliography:

[1]. VON BARTHELD, Christopher S.; BAHNEY, Jami; HERCULANO-HOUZEL, Suzana. The search for true numbers of neurons and glial cells in the human brain: A review of 150 years of cell counting. Journal of Comparative Neurology, 2016, 524.18: 3865-3895.

[2]. LANDHUIS, Esther. Neuroscience: Big brain, big data. 2017.

[3]. AHMAD, Irfan; POTHUGANTI, Karunakar. Analysis of different convolution neural network models to diagnose Alzheimer's disease. *Materials Today: Proceedings*, 2020.

[4]. SADEK, Ramzi M., et al. Parkinson's Disease Prediction Using Artificial Neural Network. 2019.

[5]. KHALID, Nauman; KOBAYASHI, Isao; NAKAJIMA, Mitsutoshi. Recent lab-on-chip developments for novel drug discovery. *Wiley Interdisciplinary Reviews: Systems Biology and Medicine*, 2017, 9.4: e1381.

[6]. GUPTA, Shagun, et al. Lab-on-chip technology: A review on design trends and future scope in biomedical applications. *Int. J. Bio-Sci. Bio-Technol*, 2016, 8: 311-322.

[7]. VAN DE WIJDEVEN, Rosanne, et al. A novel lab-on-chip platform enabling axotomy and neuromodulation in a multi-nodal network. *Biosensors and Bioelectronics*, 2019, 140: 111329.

[8]. Dale Purves, George J. Augustine, David Fitzpatrick, William C. Hall, Anthony-Samuel LaMantia, and Leonard E. White. Neuroscience. Sinauer Associates Inc., 2012.

[9]. CONNORS, Barry W. Synchrony and so much more: Diverse roles for electrical synapses in neural circuits. *Developmental neurobiology*, 2017, 77.5: 610-624.

[10]. Patel, M. (2017). *Microtubule Severing Proteins Mediate Minus-End Growth in Drosophila Neurons* (Doctoral dissertation, Pennsylvania State University).

[11]. BEZANILLA, Francisco. How membrane proteins sense voltage. *Nature reviews Molecular cell biology*, 2008, 9.4: 323-332.

[11]. CHRYSAFIDES, Steven M.; SHARMA, Sandeep. Physiology, Resting Potential. In: *StatPearls [Internet]*. StatPearls Publishing, 2020.

[12]. Ma, Y., Poole, K., Goyette, J., & Gaus, K. (2017). Introducing membrane charge and membrane potential to T cell signaling. *Frontiers in immunology*, *8*, 1513.

[13]. Cell Membrane Dynamics in Infrared Nerve Stimulation and Blocking Michelle Y. Sander Electrical and Computer Engineering, Biophysics Review Meeting, 2018

[14]. CHRYSAFIDES, Steven M.; SHARMA, Sandeep. Physiology, Resting Potential. In: *StatPearls [Internet]*. StatPearls Publishing, 2020.

[15]. KOESTER, John; SIEGELBAUM, Steven A. Membrane potential. *Principles of neural science*, 1991, 4: 125-139.

[16]. WRIGHT, Stephen H. Generation of resting membrane potential. *Advances in physiology education*, 2004, 28.4: 139-142.

[17]. BEAN, Bruce P. The action potential in mammalian central neurons. *Nature Reviews Neuroscience*, 2007, 8.6: 451-465.

[18]. Nerve Action Potential and Propagation, Section 4 - Neurophysiology. David Chambers, Christopher Huang, *University of Cambridge*, Gareth Matthews, *University of Cambridge* Publisher: Cambridge University Press. DOI: https://doi.org/10.1017/9781108565011.055 pp 225-230

[19]. ROSENBAUM, Daniel M.; RASMUSSEN, Søren GF; KOBILKA, Brian K. The structure and function of G-protein-coupled receptors. *Nature*, 2009, 459.7245: 356-363.

[20]. SÜDHOF, Thomas C.; RIZO, Josep. Synaptic vesicle exocytosis. *Cold Spring Harbor perspectives in biology*, 2011, 3.12: a005637.

[21]. PANG, Zhiping P.; SÜDHOF, Thomas C. Cell biology of Ca2+-triggered exocytosis. Current opinion in cell biology, 2010, 22.4: 496-505.

[22]. LODISH, Harvey, et al. Neurotransmitters, synapses, and impulse transmission. In: *Molecular Cell Biology. 4th edition*. WH Freeman, 2000.

[23]. BLAKELY, Randy D.; EDWARDS, Robert H. Vesicular and plasma membrane transporters for neurotransmitters. *Cold Spring Harbor perspectives in biology*, 2012, 4.2: a005595.

[24]. [20]. RUDNICK, Gary; CLARK, Janet. From synapse to vesicle: the reuptake and storage of biogenic amine neurotransmitters. *Biochimica et Biophysica Acta (BBA)-Bioenergetics*, 1993, 1144.3: 249-263.

[25]. Structural and functional analysis of prokaryotic pentameric ligand-gated ion channels. Engeler, Sibylle, Posted at the Zurich Open Repository and Archive, University of Zurich ZORA URL: https://doi.org/10.5167/uzh-129636, Dissertation, 2016

[26]. GULLEDGE, Allan T.; STUART, Greg J. Excitatory actions of GABA in the cortex. *Neuron*, 2003, 37.2: 299-309.

[27]. KHAZIPOV, Roustem; VALEEVA, Guzel; KHALILOV, Ilgam. Depolarizing GABA and developmental epilepsies. *CNS Neuroscience & Therapeutics*, 2015, 21.2: 83-91.

[28]. BEN-ARI, Yehezkel, et al. The GABA excitatory/inhibitory shift in brain maturation and neurological disorders. *The Neuroscientist*, 2012, 18.5: 467-486.

[29]. CASH, Sydney; YUSTE, Rafael. Linear summation of excitatory inputs by CA1 pyramidal neurons. *Neuron*, 1999, 22.2: 383-394.

[30]. HAO, Jiang, et al. An arithmetic rule for spatial summation of excitatory and inhibitory inputs in pyramidal neurons. *Proceedings of the National Academy of Sciences*, 2009, 106.51: 21906-21911.

[31]. SILVER, R. Angus. Neuronal arithmetic. *Nature Reviews Neuroscience*, 2010, 11.7: 474-489.

[32]. BACCELLI, Guido, et al. NACU: a non-linear arithmetic unit for neural networks. In: *2020 57th ACM/IEEE Design Automation Conference (DAC)*. IEEE, 2020. p. 1-6.

[33]. POIRAZI, Panayiota; BRANNON, Terrence; MEL, Bartlett W. Arithmetic of subthreshold synaptic summation in a model CA1 pyramidal cell. *Neuron*, 2003, 37.6: 977-987.

[34]. STILES, Joan. Neural plasticity and cognitive development. *Developmental neuropsychology*, 2000, 18.2: 237-272.

[35]. GALVÁN, Adriana. Neural plasticity of development and learning. *Human brain mapping*, 2010, 31.6: 879-890.

[36]. DANCAUSE, Numa, et al. Extensive cortical rewiring after brain injury. *Journal of Neuroscience*, 2005, 25.44: 10167-10179.

[37]. THOMSON, Alex M. Facilitation, augmentation and potentiation at central synapses. *Trends in neurosciences*, 2000, 23.7: 305-312.

[38]. CHENG, Qing; SONG, Sang-Ho; AUGUSTINE, George J. Molecular Mechanisms of Short-Term Plasticity: Role of Synapsin Phosphorylation in Augmentation and Potentiation of Spontaneous Glutamate Release. *Frontiers in Synaptic Neuroscience*, 2018, 10: 33.

[39]. ROSENMUND, Christian, et al. Differential control of vesicle priming and short-term plasticity by Munc13 isoforms. *Neuron*, 2002, 33.3: 411-424.

[40]. WEIS, Sibylle; SCHNEGGENBURGER, Ralf; NEHER, Erwin. Properties of a model of Ca++-dependent vesicle pool dynamics and short term synaptic depression. *Biophysical Journal*, 1999, 77.5: 2418-2429.

[41]. WEIS, Sibylle; SCHNEGGENBURGER, Ralf; NEHER, Erwin. Properties of a model of Ca++-dependent vesicle pool dynamics and short term synaptic depression. *Biophysical Journal*, 1999, 77.5: 2418-2429.

[42]. HEBB, Donald Olding. *The organization of behavior: A neuropsychological theory*. Psychology Press, 2005.

[43]. CUTSURIDIS, Vassilis; COBB, Stuart; GRAHAM, Bruce P. A Ca 2+ dynamics model of the STDP symmetry-to-asymmetry transition in the CA1 pyramidal cell of the hippocampus. In: *International Conference on Artificial Neural Networks*. Springer, Berlin, Heidelberg, 2008. p. 627-635.

[44 ABDULMANAPH, Nimshitha, et al. Modeling granular layer local field potential using single neuron and network based approaches to predict LTP/LTD in extracellular recordings.

[45]. NONAKA, Yukihiro; HAYASHI, Hatsuo. Spike-timing-dependent LTP/LTD caused by uncorrelated signals through medial and lateral perforant pathways in the dentate granule cell. In: *Brain-inspired information technology*. Springer, Berlin, Heidelberg, 2010. p. 115-118.

[46]. CUTSURIDIS, Vassilis; COBB, Stuart; GRAHAM, Bruce P. A CA1 heteroassociative microcircuit model of the hippocampus. *ARIADNE: Research in Encoding and Decoding of Neural Ensembles, Santorini, Greece, June*, 2008, 26-29.

[47]. LÜSCHER, Christian; MALENKA, Robert C. NMDA receptor-dependent long-term potentiation and long-term depression (LTP/LTD). *Cold Spring Harbor perspectives in biology*, 2012, 4.6: a005710.

[48]. CHEVALIER-LARSEN, Erica; HOLZBAUR, Erika LF. Axonal transport and neurodegenerative disease. *Biochimica et Biophysica Acta (BBA)-Molecular Basis of Disease*, 2006, 1762.11-12: 1094-1108.

[49]. STOKIN, Gorazd B.; GOLDSTEIN, Lawrence SB. Axonal transport and Alzheimer's disease. *Annu. Rev. Biochem.*, 2006, 75: 607-627.

[50]. FORNITO, Alex; ZALESKY, Andrew; BREAKSPEAR, Michael. The connectomics of brain disorders. *Nature Reviews Neuroscience*, 2015, 16.3: 159-172.

[51].BRAAK, Heiko, et al. Amyotrophic lateral sclerosis—a model of corticofugal axonal spread. *Nature Reviews Neurology*, 2013, 9.12: 708-714.

[52].SLEIGH, James N., et al. Axonal transport and neurological disease. *Nature Reviews Neurology*, 2019, 1-13.

[53]. JU, Yumeng, et al. Connectome-based models can predict early symptom improvement in major depressive disorder. *Journal of Affective Disorders*, 2020.

[54]. SONG, Kun-Ru, et al. Resting-state connectome-based support-vector-machine predictive modeling of internet gaming disorder. *Addiction Biology*, 2020, e12969.

[55]. YIP, Sarah W., et al. Connectome-based prediction of cocaine abstinence. *American Journal of Psychiatry*, 2019, 176.2: 156-164.

[56]. UPADHYAY, Arun, et al. Lanosterol suppresses the aggregation and cytotoxicity of misfolded proteins linked with neurodegenerative diseases. *Molecular neurobiology*, 2018, 55.2: 1169-1182.

[57]. PIETRUCHA-DUTCZAK, Marita, et al. The role of endogenous neuroprotective mechanisms in the prevention of retinal ganglion cells degeneration. *Frontiers in Neuroscience*, 2018, 12: 834.

[58]. BYLICKY, Michelle A.; MUELLER, Gregory P.; DAY, Regina M. Mechanisms of endogenous neuroprotective effects of astrocytes in brain injury. *Oxidative medicine and cellular longevity*, 2018, 2018.

[59]. BYLICKY, Michelle A.; MUELLER, Gregory P.; DAY, Regina M. Mechanisms of endogenous neuroprotective effects of astrocytes in brain injury. *Oxidative medicine and cellular longevity*, 2018, 2018.

[60]. VISSERS, Caroline; MING, Guo-li; SONG, Hongjun. Nanoparticle technology and stem cell therapy team up against neurodegenerative disorders. *Advanced drug delivery reviews*, 2019, 148: 239-251.

[61]. ZIAI, Wendy C.; LEWIN III, John J. Update in the diagnosis and management of central nervous system infections. *Neurologic clinics*, 2008, 26.2: 427-468.

[62]. ESPAY, Alberto J., et al. Current concepts in diagnosis and treatment of functional neurological disorders. *JAMA neurology*, 2018, 75.9: 1132-1141.

[63]. BUTLER, Matthew, et al. Psychedelic treatment of functional neurological disorder: a systematic review. *Therapeutic Advances in Psychopharmacology*, 2020, 10: 2045125320912125.

[64]. Koellhoffer, E. C., McCullough, L. D., & Ritzel, R. M. (2017). Old maids: aging and its impact on microglia function. *International journal of molecular sciences*, *18*(4), 769.

[65]. FATTORE, Liana (ed.). *Cannabinoids in Neurologic and Mental Disease*. Academic Press, 2015.

[66]. HABIB, Syed Shahid, et al. Role of endocannabinoids on neuroinflammation in autism spectrum disorder prevention. *Journal of clinical and diagnostic research: JCDR*, 2017, 11.6: CE01.

[67]. PRYCE, Gareth, et al. Neuroprotection in experimental autoimmune encephalomyelitis and progressive multiple sclerosis by cannabis-based cannabinoids. *Journal of neuroimmune pharmacology*, 2015, 10.2: 281-292.

[68]. DHOUAFLI, Zohra, et al. Inhibition of protein misfolding and aggregation by natural phenolic compounds. *Cellular and molecular life sciences*, 2018, 75.19: 3521-3538.

[69]. Richardson PM, McGuinness UM, Aguayo AJ. Axons from CNS neurons regenerate into PNS grafts. Nature. 1980;284:264–265

[70]. Richardson PM, Issa VM, Aguayo AJ. Regeneration of long spinal axons in the rat. J Neurocytol. 1984;13:165–182

[71]. BENFEY, Martin; AGUAYO, Albert J. Extensive elongation of axons from rat brain into peripheral nerve grafts. *Nature*, 1982, 296.5853: 150-152.

[72]. DAVID, Samuel; AGUAYO, Albert J. Axonal elongation into peripheral nervous system" bridges" after central nervous system injury in adult rats. *Science*, 1981, 214.4523: 931-933.

[73]. HUEBNER, Eric A.; STRITTMATTER, Stephen M. Axon regeneration in the peripheral and central nervous systems. In: *Cell biology of the axon*. Springer, Berlin, Heidelberg, 2009. p. 305-360.

[74]. FAWCETT, James W. The struggle to make CNS axons regenerate: why has it been so difficult?. *Neurochemical research*, 2020, 45.1: 144-158.

[75]. STEWART, John D. Peripheral nerve fascicles: anatomy and clinical relevance. *Muscle & nerve*, 2003, 28.5: 525-541.

[76]. UBOGU, Eroboghene E. Biology of the human blood-nerve barrier in health and disease. *Experimental neurology*, 2020, 328: 113272.

[77]. Reina, M. A., Boezaart, A. P., Tubbs, R. S., Zasimovich, Y., Fernández-Domínguez, M., Fernández, P., & Sala-Blanch, X. (2020). Another (internal) epineurium: beyond the anatomical barriers of nerves. *Clinical Anatomy*, *33*(2), 199-206.

[78]. ALVITES, Rui, et al. Peripheral nerve injury and axonotmesis: State of the art and recent advances. *Cogent Medicine*, 2018, 5.1: 1466404.

[79]. WAN, Lidan, et al. Short-term low-frequency electrical stimulation enhanced remyelination of injured peripheral nerves by inducing the promyelination effect of brain-derived neurotrophic factor on Schwann cell polarization. *Journal of neuroscience research*, 2010, 88.12: 2578-2587.

[80]. ZHANG, Xu, et al. Electrical stimulation enhances peripheral nerve regeneration after crush injury in rats. *Molecular medicine reports*, 2013, 7.5: 1523-1527.

[81]. ROCHKIND, Shimon. Phototherapy in peripheral nerve regeneration: From basic science to clinical study. *Neurosurgical Focus*, 2009, 26.2: E8.

[82].Kim, C. K., Adhikari, A., & Deisseroth, K. (2017). Integration of optogenetics with complementary methodologies in systems neuroscience. *Nature Reviews Neuroscience*, *18*(4), 222-235.

[83].Boyle, P. M., Karathanos, T. V., & Trayanova, N. A. (2018). Cardiac optogenetics: 2018. *JACC: Clinical Electrophysiology*, *4*(2), 155-167.

[84].Lin, M. Z., & Schnitzer, M. J. (2016). Genetically encoded indicators of neuronal activity. *Nature neuroscience*, *19*(9), 1142.

[85].Piatkevich, K. D., Murdock, M. H., & Subach, F. V. (2019). Advances in engineering and application of optogenetic indicators for neuroscience. *Applied Sciences*, *9*(3), 562.

[86].Vogt, C. C., Bruegmann, T., Malan, D., Ottersbach, A., Roell, W., Fleischmann, B. K., & Sasse, P. (2015). Systemic gene transfer enables optogenetic pacing of mouse hearts. *Cardiovascular research*, *106*(2), 338-343.

[87].Crocini, C., Ferrantini, C., Coppini, R., Scardigli, M., Yan, P., Loew, L. M., ... & Sacconi, L. (2016). Optogenetics design of mechanistically-based stimulation patterns for cardiac defibrillation. *Scientific reports*, *6*(1), 1-7.

[88].Vinepinsky, E., Donchin, O., & Segev, R. (2017). Wireless electrophysiology of the brain of freely swimming goldfish. *Journal of neuroscience methods*, *278*, 76-86.

[89].Bilodeau, G., Gagnon-Turcotte, G., Gagnon, L. L., Ethier, C., Timofeev, I., & Gosselin, B. (2020, October). A Wireless Electro-Optic Headstage with Digital Signal Processing and Data Compression for Multimodal Electrophysiology and Optogenetic Stimulation. In *2020 IEEE International Symposium on Circuits and Systems (ISCAS)* (pp. 1-5). IEEE.

[90].Zhang, L. (2017, July). Implementation of fixed-point neuron models with threshold, ramp and sigmoid activation functions. In *IOP Conference Series: Materials Science and Engineering* (Vol. 224, No. 1, p. 012054). IOP Publishing.

[91].Yang, S., Deng, B., Wang, J., Li, H., Lu, M., Che, Y., ... & Loparo, K. A. (2019). Scalable digital neuromorphic architecture for large-scale biophysically meaningful neural network with multi-compartment neurons. *IEEE transactions on neural networks and learning systems*, *31*(1), 148-162.

[92].Venkadesh, S., Komendantov, A. O., Listopad, S., Scott, E. O., De Jong, K., Krichmar, J. L., & Ascoli, G. A. (2018). Evolving simple models of diverse intrinsic dynamics in hippocampal neuron types. *Frontiers in neuroinformatics*, *12*, 8.

[93].Hu, X., & Liu, C. (2019). Dynamic property analysis and circuit implementation of simplified memristive Hodgkin–Huxley neuron model. *Nonlinear Dynamics*, *97*(2), 1721-1733.

[94].Niebur, E. (2008). Neuronal cable theory. *Scholarpedia*, *3*(5), 2674.

[95].Jaeger, D. (2005). Realistic single cell modeling–from experiment to simulation. *Brains, Minds and Media*, *1*(2).

[96].Rob Phillips, Jane Kondev, Julie Theriot, Hernan G. Garcia, and Nigel Orme. Physical Biology of the Cell. Garland Science, 2013.

[97].Buzsáki, G., Anastassiou, C. A., & Koch, C. (2012). The origin of extracellular fields and currents—EEG, ECoG, LFP and spikes. *Nature reviews neuroscience*, *13*(6), 407-420.

[98].Fabrication and Optimization of Microelectrode Arrays for Neural Networks, Leik Bjelland Isdal, CC-BY 2020/12/18

[99].Obien, M. E. J., Deligkaris, K., Bullmann, T., Bakkum, D. J., & Frey, U. (2015). Revealing neuronal function through microelectrode array recordings. *Frontiers in neuroscience*, *8*, 423.

[100].Deligkaris, K., Bullmann, T., & Frey, U. (2016). Extracellularly recorded somatic and neuritic signal shapes and classification algorithms for high-density microelectrode array electrophysiology. *Frontiers in neuroscience*, *10*, 421.

[101].Camuñas-Mesa, L. A., & Quiroga, R. Q. (2013). A detailed and fast model of extracellular recordings. *Neural computation*, *25*(5), 1191-1212.

[102].Rutkove, S. B. (2007). Introduction to volume conduction. In *The clinical neurophysiology primer* (pp. 43-53). Humana Press.

[103].De Munck, J. C., & Van Dijk, B. W. (1991). Symmetry considerations in the quasi-static approximation of volume conductor theory. *Physics in medicine & biology*, *36*(4), 521.

[104].Bossetti, C. A., Birdno, M. J., & Grill, W. M. (2007). Analysis of the quasi-static approximation for calculating potentials generated by neural stimulation. *Journal of neural engineering*, *5*(1), 44.

[105].Camuñas-Mesa, L. A., & Quiroga, R. Q. (2013). A detailed and fast model of extracellular recordings. *Neural computation*, *25*(5), 1191-1212.

[106].Hodgkin, A. L., & Huxley, A. F. (1952). A quantitative description of membrane current and its application to conduction and excitation in nerve. *The Journal of physiology*, *117*(4), 500-544.

[107].ROBINSON, David A. The electrical properties of metal microelectrodes. *Proceedings of the IEEE*, 1968, 56.6: 1065-1071.

[108].GOLD, Carl, et al. On the origin of the extracellular action potential waveform: a modeling study. *Journal of neurophysiology*, 2006, 95.5: 3113-3128.

[109].Moffitt, M. A., & McIntyre, C. C. (2005). Model-based analysis of cortical recording with silicon microelectrodes. *Clinical neurophysiology*, *116*(9), 2240-2250.

[110].Lind, R., Connolly, P., Wilkinson, C. D. W., & Thomson, R. D. (1991). Finite-element analysis applied to extracellular microelectrode design. *Sensors and Actuators B: Chemical*, *3*(1), 23-30.

[111].Fromherz, P. (2006). Three levels of neuroelectronic interfacing: silicon chips with ion channels, nerve cells, and brain tissue. *Annals of the New York Academy of Sciences*, *1093*(1), 143-160.

[112].Ingebrandt, S., Yeung, C. K., Krause, M., & Offenhäusser, A. (2005). Neuron–transistor coupling: interpretation of individual extracellular recorded signals. *European biophysics journal*, *34*(2), 144-154.

[113].Joye, N., Schmid, A., & Leblebici, Y. (2008, August). An electrical model of the cell-electrode interface for high-density microelectrode arrays. In *2008 30th Annual International Conference of the IEEE Engineering in Medicine and Biology Society* (pp. 559-562). IEEE.

[114].Thakore, V., Molnar, P., & Hickman, J. J. (2012). An optimization-based study of equivalent circuit models for representing recordings at the neuron–electrode interface. *IEEE transactions on biomedical engineering*, *59*(8), 2338-2347.

[115].HIERLEMANN, Andreas, et al. Growing cells atop microelectronic chips: interfacing electrogenic cells in vitro with CMOS-based microelectrode arrays. *Proceedings of the IEEE*, 2010, 99.2: 252-284.

[116].Obien, M. E. J., Deligkaris, K., Bullmann, T., Bakkum, D. J., & Frey, U. (2015). Revealing neuronal function through microelectrode array recordings. *Frontiers in neuroscience*, *8*, 423.

[117].Oldham, K. B. (2008). A Gouy–Chapman–Stern model of the double layer at a (metal)/(ionic liquid) interface. *Journal of Electroanalytical Chemistry*, *613*(2), 131-138.

[118]https://web.nmsu.edu/~snsm/classes/chem435/Lab14/double_layer.html

[119].Ojovan, S. M., Rabieh, N., Shmoel, N., Erez, H., Maydan, E., Cohen, A., & Spira, M. E. (2015). A feasibility study of multi-site, intracellular recordings from mammalian neurons by extracellular gold mushroom-shaped microelectrodes. *Scientific reports*, *5*(1), 1-14.

[120].Duan, X., Gao, R., Xie, P., Cohen-Karni, T., Qing, Q., Choe, H. S., ... & Lieber, C. M. (2012). Intracellular recordings of action potentials by an extracellular nanoscale field-effect transistor. *Nature nanotechnology*, *7*(3), 174-179.

[121].Lin, Z. C., Xie, C., Osakada, Y., Cui, Y., & Cui, B. (2014). Iridium oxide nanotube electrodes for sensitive and prolonged intracellular measurement of action potentials. *Nature communications*, *5*(1), 1-10.

[122].Fendyur, A., Mazurski, N., Shappir, J., & Spira, M. E. (2011). Formation of essential ultrastructural interface between cultured hippocampal cells and gold mushroom-shaped MEA-toward “IN-CELL” recordings from vertebrate neurons. *Frontiers in neuroengineering*, *4*, 14.

[123].Santoro, F., Schnitker, J., Panaitov, G., & Offenhäusser, A. (2013). On chip guidance and recording of cardiomyocytes with 3D mushroom-shaped electrodes. *Nano letters*, *13*(11), 5379-5384.

[124].Massobrio, G., Martinoia, S., & Massobrio, P. (2017). Equivalent circuit of the neuro-electronic junction for signal recordings from planar and engulfed micro-nano-electrodes. *IEEE transactions on biomedical circuits and systems*, *12*(1), 3-12.

[125].Hamilton, F., Berry, T., & Sauer, T. (2018). Tracking intracellular dynamics through extracellular measurements. *PloS one*, *13*(10), e0205031.

[126].Jones, P. D., Moskalyuk, A., Barthold, C., Gutöhrlein, K., Heusel, G., Schröppel, B., ... & Giugliano, M. (2020). Low-impedance 3D PEDOT: PSS ultramicroelectrodes. *Frontiers in Neuroscience*, *14*.

[127].Teixeira, H., Dias, C., Aguiar, P., & Ventura, J. (2021). Gold-Mushroom Microelectrode Arrays and the Quest for Intracellular-Like Recordings: Perspectives and Outlooks. *Advanced Materials Technologies*, *6*(2), 2000770.

[128].Cerquido, M., Proenca, M. P., Dias, C., Leitao, D. C., Cardoso, S., Freitas, P. P., ... & Ventura, J. (2018). Tailoring the cap's morphology of electrodeposited gold micro-mushrooms. *Applied Surface Science*, *445*, 512-518.

[129].Trejo, G., Gil, A. F., & Gonzalez, I. (1996). Electrodeposition of gold in ammoniacal medium: influence of substrate and temperature. *Journal of applied electrochemistry*, *26*(12), 1287-1294.

[130].Cerquido, M. C. C. (2016). Fabrication of biocompatible gold mushrooms-shaped microelectrodes for the recording of neuronal signals.

[131]. Photolithography: Basics of Microstructuring. Authors, Titus J. Rinke, Christian Koch. Editor, MicroChemicals GmbH. Publisher, MicroChemicals, 2017.

[132]. http://www.lithoguru.com/scientist/lithobasics.html

[133]. Spin Coating of Thin and Ultrathin Polymer Films DAVID B. HALL,',' PATRICK UNDERHILL,2 &JOHN M. TORKELSON~,~,~ Department of Chemical Engineering Materials Research Center Department of Materials Science and Engineering Northwestern University Evanston, Hinois 60208-3 120

[134]. A. G. Emslie, F. T. Bonner, and L. G. Peck, J. Appl. Phys., 29. 858 (1958)

[135].https://cnx.org/contents/KZdIG-zX@2/Composition-and-Photochemical-Mechanisms-of-Photoresists

[136]. QUIRK, Michael; SERDA, Julian. *Semiconductor manufacturing technology*. Upper Saddle River, NJ: Prentice Hall, 2001, page 348-357

[137].https://www.compadre.org/nexusph/course/Debye_length

[138].https://www.78stepshealth.us/human-physiology/ionic-bonds.html

[139].Sand, H. J. S., III. On the concentration at the electrodes in a solution, with special reference to the liberation of hydrogen by electrolysis of a mixture of copper sulphate and sulphuric acid. *Philos. Mag.* 1901, *1*, 45– 79, DOI: 10.1080/14786440109462590

[140].Yoon, G., Moon, S., Ceder, G., & Kang, K. (2018). Deposition and stripping behavior of lithium metal in electrochemical system: continuum mechanics study. *Chemistry of Materials*, *30*(19), 6769-6776.

[141]. Savage, N. Digital spatial light modulators. *Nature Photon* 3, 170–172 (2009).

[142]. Keloth, Anusha, et al. "Single-cell isolation using optical tweezers." *Micromachines* 9.9 (2018): 434.

[143]. Lee, Michael P., and Miles J. Padgett. "Optical tweezers: A light touch." *Journal of Microscopy* 248.3 (2012): 219-222.

[144]. Mack, Chris A. "Resolution and depth of focus in optical lithography." *Microlithographic Techniques in IC Fabrication*. Vol. 3183. International Society for Optics and Photonics, 1997.

[145]. Mack, “Understanding Focus Effects in Submicron Optical Lithography,” Optical/Laser Microlithography, Proc., SPIE Vol. 922 (1988) pp. 135-148, and Optical Engineering, Vol. 27, No. 12 (Dec. 1988) pp. 1093-1100.

[146]. Mack, Chris A., and Patricia M. Kaufman. "Understanding focus effects in submicron optical lithography, part 2: Photoresist effects." *Optical/Laser Microlithography II*. Vol. 1088. International Society for Optics and Photonics, 1989.

[147]. Mack, Chris A. "Understanding focus effects in submicron optical lithography: Part 3--methods for depth-of-focus improvement." *Optical/Laser Microlithography V*. Vol. 1674. International Society for Optics and Photonics, 1992.

[148]. Shuttleworth, Ro. "The surface tension of solids." *Proceedings of the physical society. Section A* 63.5 (1950): 444.

[149]. Onat Akbulut, Serder, et al. "Impedance testing of porous Si3N4 scaffolds for skeletal implant applications." *SN Applied Sciences* 2 (2020).
[10]. Suh, Sean, and Jon Suh. "Silicon nitride implants and coatings." U.S. Patent Application No. 16/726,043.

[150]. Maloney, J. M., Lipka, S. A., & Baldwin, S. P. (2005). In vivo biostability of CVD silicon oxide and silicon nitride films. MRS Online Proceedings Library (OPL), 872.

[151]. Pezzotti, Giuseppe, et al. "Incorporating Si3N4 into PEEK to produce antibacterial, osteocondutive, and radiolucent spinal implants." *Macromolecular bioscience* 18.6 (2018): 1800033.

[152]. Kuo, Yue. "Reactive ion etching of PECVD amorphous silicon and silicon nitride thin films with fluorocarbon gases." *Journal of the Electrochemical Society* 137.4 (1990): 1235.
Shuttleworth, Ro. "The surface tension of solids." *Proceedings of the physical society. Section A* 63.5 (1950): 444.

[153]. Padron, I. (Ed.). (2012). *Interferometry: Research and Applications in Science and Technology*. BoD–Books on Demand.

[154]. Akhtar, K., Khan, S. A., Khan, S. B., & Asiri, A. M. (2018). Scanning electron microscopy: Principle and applications in nanomaterials characterization. In *Handbook of materials characterization* (pp. 113-145). Springer, Cham.

[155]. Stokes, D. (2008). *Principles and practice of variable pressure/environmental scanning electron microscopy (VP-ESEM)*. John Wiley & Sons.

[156]. Stokes, D. (2008). *Principles and practice of variable pressure/environmental scanning electron microscopy (VP-ESEM)*. John Wiley & Sons.

[157]. Baumgärtner, M. E., & Raub, J. (1988). The electrodeposition of platinum and platinum alloys. *Platinum Metals Review*, *32*(4), 188-197.

Appendix

A.1 Protocol for Fabrication of MEAs

Preparation of Substrate (15 min)

1. Waferclean (borosilicate 4-inch wafer):
    - Wash in acetone for 1 minute
    - Wash in isopropyl alcohol (IPA) for 1 minute
    - Dry under nitrogen air gun
2. Remove organic residues from substrate with a plasma oven for 5 minutes at 50% power and 50% oxygen flow (50 sccm O_2 at 0.26 mbar and 50 W)
3. Dehydration bake: Heat the substrate on a hotplate for 2 minutes using a temperature of 100 °C

Photoresist Layer 1 (20 min)

1. Blow clean the substrate surface with a nitrogen air gun
2. Place the substrate on an appropriate sized chuck in a spin coater and spin coat the photoresist MaN-440 (~ 3 mL for a 4-inch wafer) using a single-use pipette onto the substrate in one step:

    • 3000 rpm for 30 seconds at 200 rpm/sec
3. Relaxation: Let the film rest for 5 - 10 minutes on a cleanroom wipe covered with a glass beaker (to avoid contamination)
4. Soft bake: Heat the substrate on a hotplate for 5 minutes at a temperature of 95 °C

Exposure 1 (45 min)

1. Follow the user protocol of the MLA150: Upload the design into the software of the computer. Make sure to invert the design if necessary (maN-440 is a negative resist). Set the exposure dose to 2400 MJ/cm^2 (405 nm laser)
2. Relaxation: Let the film rest for 5 - 10 minutes on a cleanroom wipe covered with a glass beaker (to avoid contamination)

Development 1 (10 min)

1. Develop the exposed substrate by gently stirring it in the developer ma-D332/S every 15 sec for a total of 2 min 15 sec - 2 min 30 sec

2. Rinse the substrate with DI water from a squirt bottle directly after development for 30 seconds

3. Dry the substrate with a nitrogen air gun

4. Check the developed pattern under the microscope. Check for the following:

    - Overdeveloped/overexposed features (seen as development/removal of photoresist outside of the exposed pattern): Remove pattern in acetone and start over
    - Underdeveloped/underexposed features (seen as areas with remaining photoresist, often visible as colored fringes): Develop pattern for 10 - 20 sec longer and check again

Metal Evaporation (45 min)

1. Descum the substrate: Place the substrate in the plasma oven and descum the surface for 1 minute at 50% power and 50% oxygen flow
(50 sccm O_2 at 0.26 mbar and 50 W)
2. Follow the protocol of the AJA Evaporator: Evaporate 50 nm of titanium and 100 nm of platinum onto the substrate

3. Do a lift-off in acetone for 3-5 min (do not let the acetone dry up on the substrate). Use a brush to gently remove smaller particles from the substrate

4. Rinse the substrate subsequently with fresh acetone and IPA, before drying it with a nitrogen air gun

5. Check the substrate under a microscope: Make sure that there are no metal particles left on the surface and that the metal circuit is intact. This is especially important for the reference electrode and its contact pad.

Passivation Layer Deposition (60 min)

1. Place the substrate in a plasma oven and descum the surface for 1 min at 50% power and 50% oxygen flow (50 sccm O_2 at 0.26 mbar and 50 W)

2. Place the substrate in the PECVD load lock, and select the appropriate recipe (OPT Si3N4). The duration of the gas (SiH_4 at 20.0 sccm, NH_3 at 20.0 sccm and N_2 at 980 sccm) release step should be set to 30 minutes. Nothing else should be changed.

3. Run the recipe and follow further instructions stated in the protocol of the device.

Photoresist Layer 2 (20 min)

1. Place the substrate in a plasma oven and descum the surface for 1 min at 50% power and 50% oxygen flow (50 sccm O_2 at 0.26 mbar and 50 W)

2. Blow clean the substrate surface with a nitrogen air gun

3. Place the substrate on an appropriate sized chuck in a spin coater and spin coat the photoresist MaN-440 (~ 3 mL for a 4-inch wafer) using a single-use pipette onto the substrate in one step:

   • 3000 rpm for 30 seconds at 200 rpm/sec
4. Relaxation: Let the film rest for 5 - 10 minutes on a cleanroom wipe covered with a glass beaker (to avoid contamination)

5. Soft bake: Heat the substrate on a hotplate for 5 minutes at a temperature of 95 °C

Exposure 2 (45 min)

1. Follow the user protocol of the MLA150: Upload the design into the software of the computer. Make sure to invert the design if necessary (maN-440 is a negative resist). Use the MLA to align the second layer to the first one with use of the alignment marks, and set the exposure dose to 800 MJ/cm^2 (405 nm laser)

2. Post-exposure bake: Heat the substrate on a hot plate for 90 seconds at a temperature of 110 °C

3. Relaxation: Let the film rest for 5 - 10 minutes on a cleanroom wipe covered with a glass beaker (to avoid contamination)

Development 2 (10 min)

1. Develop the exposed substrate by gently stirring it in the developer ma-D332/S every 15 sec for a total of 1 min 45 sec - 2 min 15 sec

2. Rinse the substrate with DI water from a squirt bottle directly after development for 30 seconds

3. Dry the substrate with a nitrogen air gun

4. Check the developed pattern under the microscope. Check for the following:

   - Overdeveloped/overexposed features (seen as development/removal of photoresist outside of the exposed pattern): Remove pattern in acetone and start over
   - Underdeveloped/underexposed features (seen as areas with remaining photoresist, often visible as colored fringes): Develop pattern for 10 - 20 sec longer and check again

Etch Passivation Layer (40 min)

1. Place the substrate in a plasma oven and descum the surface for 1 min at 50% power and 50% oxygen flow (50 sccm O_2 at 0.26 mbar and 50 W)
2. Place the substrate in the ICP-RIE chiller load lock according to the markings and follow the user protocol of the machine

3. Select the correct recipe ("Jens nitride etch"), and change the duration of the gas release step (CHF_3 at 50.0 sccm, CF_4 at 10.0 sccm and O_2 at 7.0 sccm) to 6 min 30 sec. Nothing else should be changed.

Electroplating (60 min)

1. Follow the user protocol for electroplating system Yamamoto. Place the substrate in the holder, connect the potentiostat to the electrodes, and then to the computer.
2. From the software, choose mode ‘’Chronoamperometry’’ and set the voltage at 0.05V for 600 sec.
3. Rinse with DI water and gently dry with nitrogen gun
4. Perform step number 2 and 3 on each of the contact pads connected to the working electrodes

Photoresist layer 3 (40 min)

1. Place the substrate on an appropriate sized chuck in a spin coater and spin coat the photoresist MaN-440 (~ 3 mL for a 4-inch wafer) using a single-use pipette onto the substrate in one step:

   • 3000 rpm for 30 seconds at 200 rpm/sec
2. Relaxation: Let the film rest for 5 - 10 minutes on a cleanroom wipe covered with a glass beaker (to avoid contamination)
3. Soft bake: Heat the substrate on a hotplate for 5 minutes at a temperature of 95 °C

Dicing of MEA to Appropriate Size (20 min)

1. Prepare the substrate by sticking it onto tape and ring using the appropriate device
2. Follow the user protocol of the dicing machine
3. Select the appropriate job, created for the substrate (a three step dicing of 0.9 - 0.45 - 0.1 dicing depth is appropriate for a borosilicate wafer)
4. Measure ‘saw thickness’ before dicing and check correspondance with the log book
5. Align the machine with the square outline, along which the MEA will be diced
6. Dice the substrate
7. Remove the MEA from the tape after exposing it to UV light
8. Bring the MEA back into the cleanroom and remove the photoresist etch mask with acetone
9. In case there are traces of photoresist left after removal of the etch mask, do a descum of the surface in the plasma cleaner for 10-15 minutes at 50% power and 50% oxygen flow (50 sccm O_2 at 0.26 mbar and 50 W)

Cleaning of the MEAs

1. Prepare three beakers: one with acetone, one with mr-Rem 660, and one with ethanol.
2. Place the MEA in acetone for 3 min, rinse with acetone from a squirt bottle before moving to the next beaker.
3. Place the MEA in remover mr-Rem 660 for 3 min, rinse with ethanol from a squirt bottle before moving to the next beaker.
4. Place the MEA in ethanol for 2 min, rinse with ethanol from a squirt bottle
5. Dry the MEA with a nitrogen air gun

A.2 Table with measurements of photoresist thickness versus spin parameters

photoreisit	average thickness [nm]	max deviation from average thickness	spin reciepe
ma-N 440	3228	4.6 nm / 0.12 %	6000 rpm, 30 sec. at 1000 rpm/s
AZ 5214E	2332	42.2 nm / 1.8 %	2000 rpm, 30 sec. at 500 rpm/s
SPR 700	940	0.25 nm / 0.03 %	4000 rpm, 34 sec at 1000 rpm/s
Second trial			
ma-N 440	2960	64.4 nm / 2.2 %	6000 rpm, 34 sec. at 1000 rpm/s
AZ 5214E	2285	52.4 nm / 2.3 %	2000 rpm, 30 sec. at 500 rpm/s
SPR 700	960	0.37 nm / 0.03 %	3900 rpm, 34s sec. at 1000 rpm/s
Third trial			
ma-N 440	3126	6.1 nm / 0.2 %	6000 rpm, 33 sec. at 1000 rpm/s
AZ 5214E	2083	113.8 nm / 5.5 %	2400 rpm, 30 sec. at 500 rpm/s
SPR 700	974	< 1 nm / < 0.1 %	3700 rpm, 34 sec. at 1000 rpm/s

photoreisit	measurement [nm]	#1	#2	#3	#4	#5	#6	#7
ma-N 440		3227.3	3228.2	3233	3230.2	3228.7	3226.3	3225.2
AZ 5214E		2374.4	2346.1	1598.8	2341.9	2291.8	1531.8	2307
SPR 700		940.57	940.62	940.62	940.33	940.62	940.55	940.77
Second trial								
ma-N 440		2913.8	2914.2	2912.5	3023.1	2913.1	3019.2	3022.3
AZ 5214E		2320.8	2306.6	2278.7	2301.7	2285.8	2232.5	2268.7
SPR 700		960.67	960.22	960.05	960.62	960.44	960.62	960.37
Third trial								
ma-N 440		3122.9	3124.6	3123	3126.1	3128.8	3125.6	3129
AZ 5214E		2076.1	2061.9	2140.1	1969.2	2083.2	2124.9	2127.5
SPR 700		974.47	974.19	974.31	974.65	974.07	974.76	973.46

Table with measurements of film thickness for different conditions of the spin process - for ma N - 440 - different spin-time, for AZ 5214E and SPR 700 - different spin-speed. The average thickness and deviation of the measurements from the average thickness (measured in nm and %) for the three photoresists are also presented. The data was used to investigate the thickness dependence on the spin-speed and spin-time and to confirm the formula for the thickness versus spin-speed

A3 Designs of exposure dose test samples

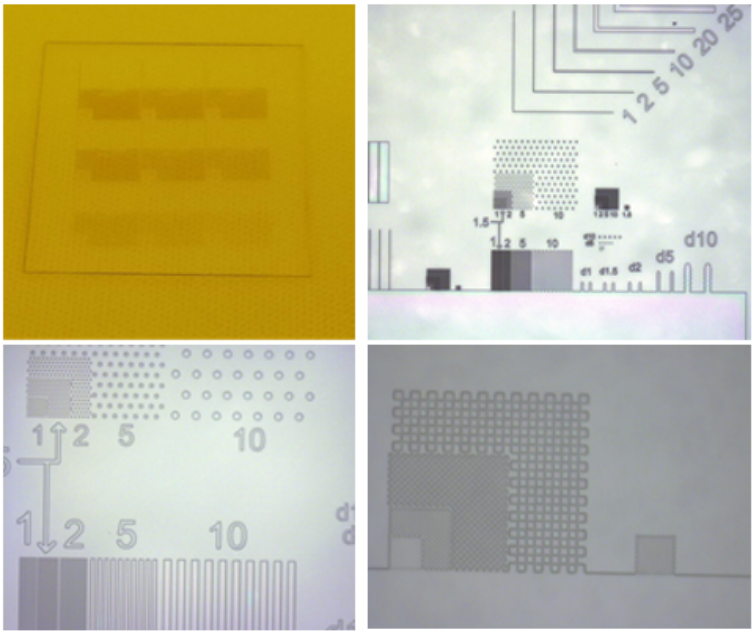

Fig. 1 Overview of the test samples used for the optimization of the exposure dose. Glass coverslips exposed with 405nm laser wavelength in a range of 400-2500 mJ/cm2, side length of the coverslip is 24mm. The numbers in the mask show the size of the features in microns.

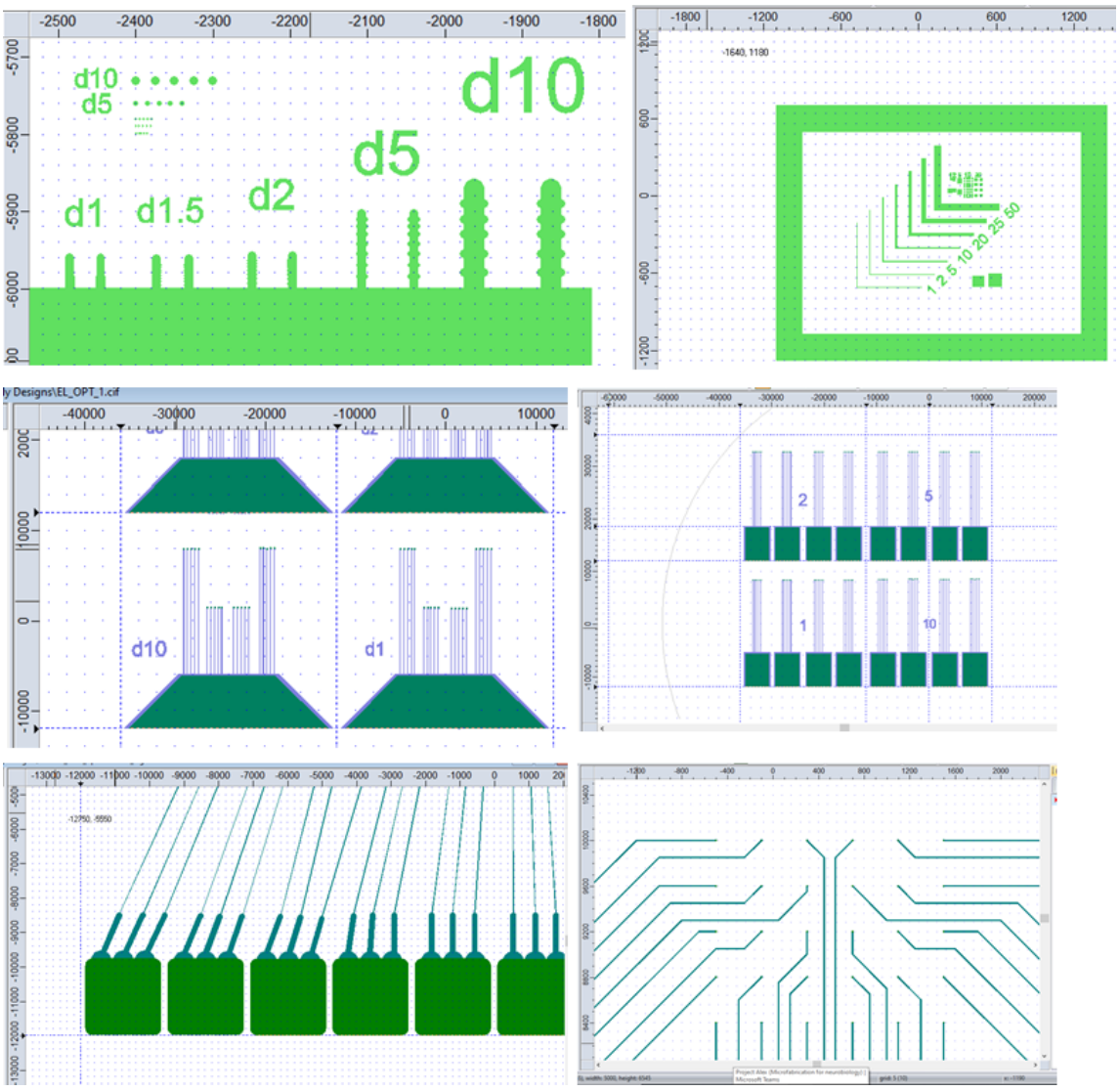

Fig. 2 Mask designs used for the optimization of the exposure dose (first row), for testing the optimized parameters of the exposure dose onto the underlying reflective metal surface (second row), and for testing the adhesion of the metal contact lines to the substrate (third row).

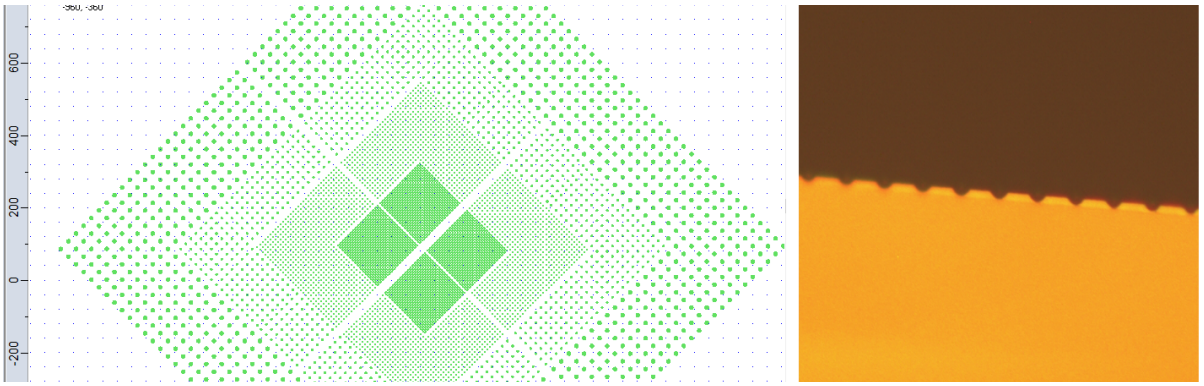

Fig. 3 Design of the mask (first image) for imaging the cross-section of the photoresist (second image). The features are circular with a diameter of 2 microns and the spacing between them decreases towards the central point to optimize the resolution. The coverslip is cut along the diagonal of the mask to reveal a cross-section of the microholes, magnification 50x.

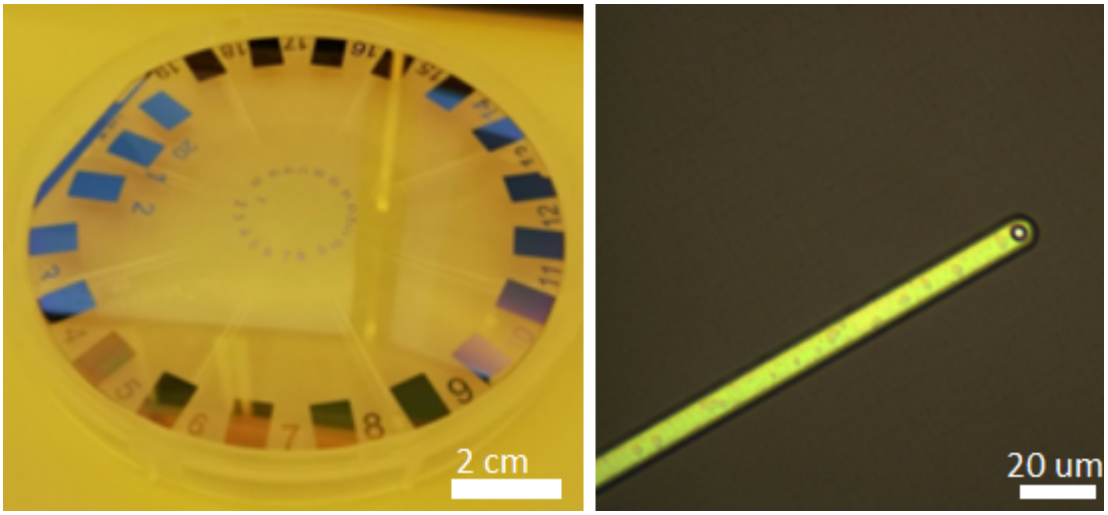

Fig. 4 First image shows a test sample prepared for electroplating. The second image is taken with an optical microscope and shows an electrode with a diameter of 5um, contact metal line is 10um wide, magnification 20x.

A4 Results from characterization of electrodeposition with constant current

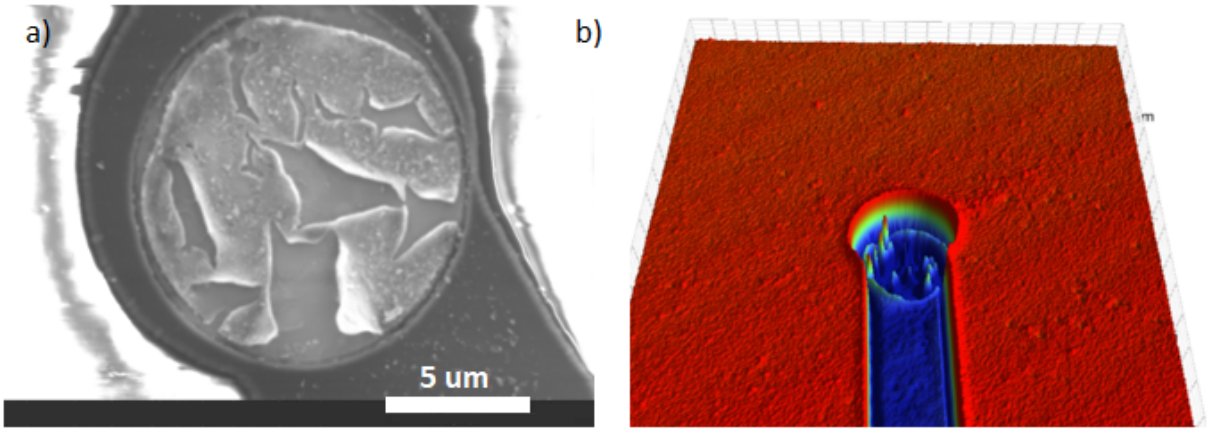

Fig. 1 a) SEM image and b) 3D image from optical profilometer of 10um electrode deposition for 5min with 1nA/um2, voltage limit 40V. The resulting thin delaminated layer is not sufficient for the purpose of growing 3D structures.

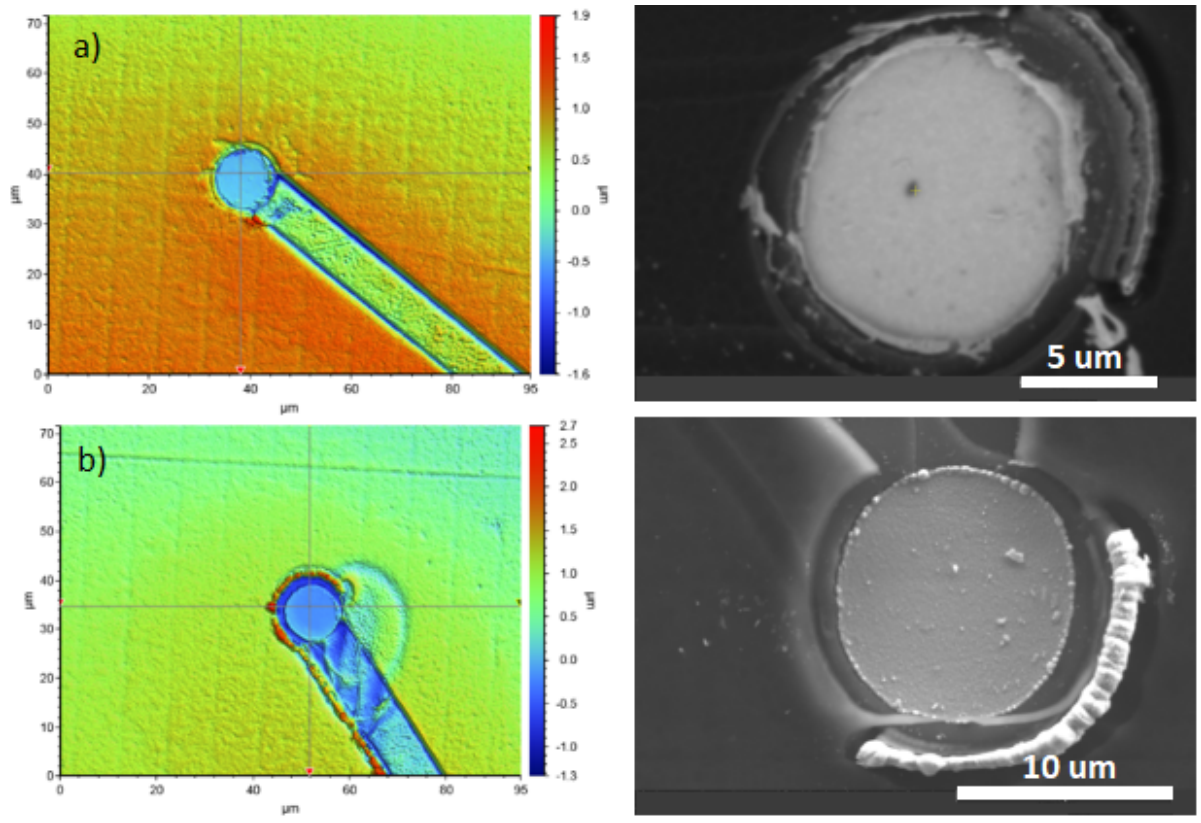

Fig. 2 Even depositions on 10 um electrodes with a current density of a) 50 and b) 100 nA/um2, voltage limit 40V. The rate of the deposition, 10 and 20 nm/min respectively, is slow for the purpose of this project.

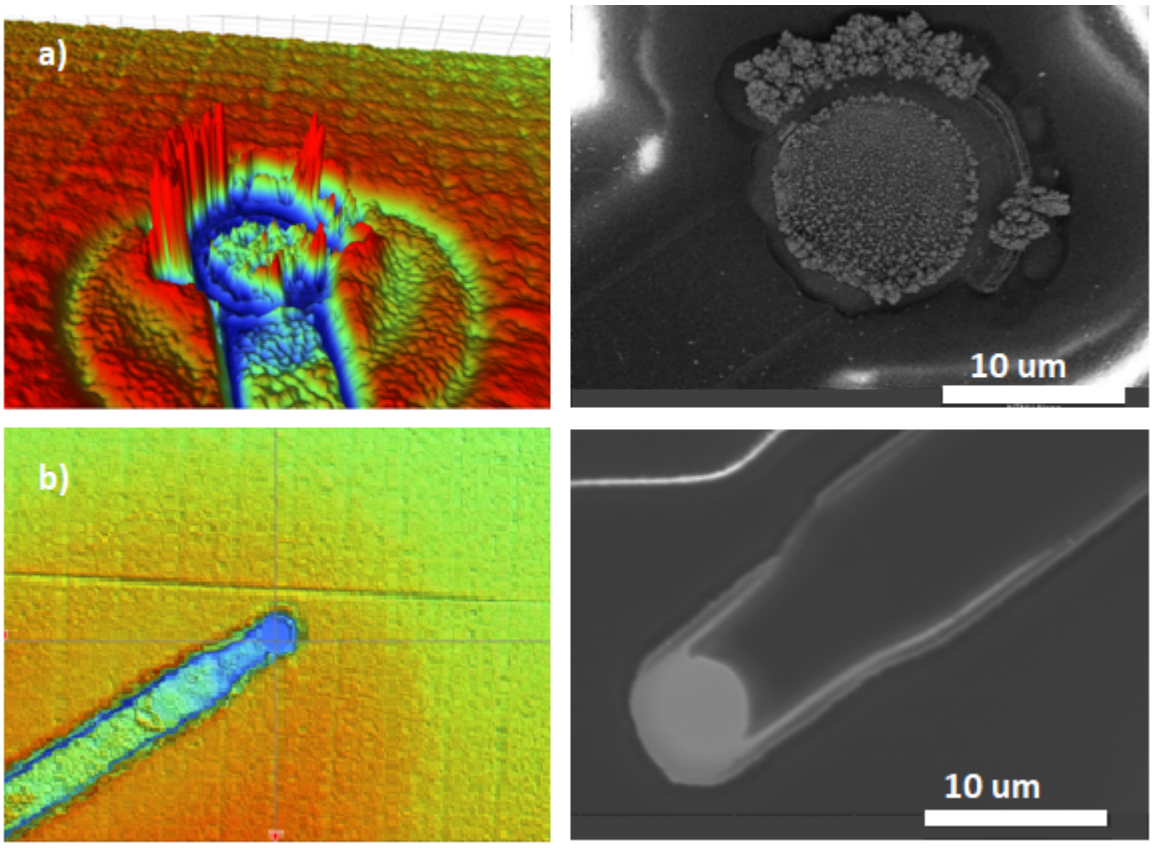

Fig. 3 Images of deposition on two electrodes with 400 nA/um2 and voltage limits of a) 40V and b) 1V. High current density with a high voltage limit leads to the formation of porous morphology with pronounced edge defects. For a low voltage limit of 1V, the deposition is even.

A5 Results from characterization of electrodeposition with constant voltage

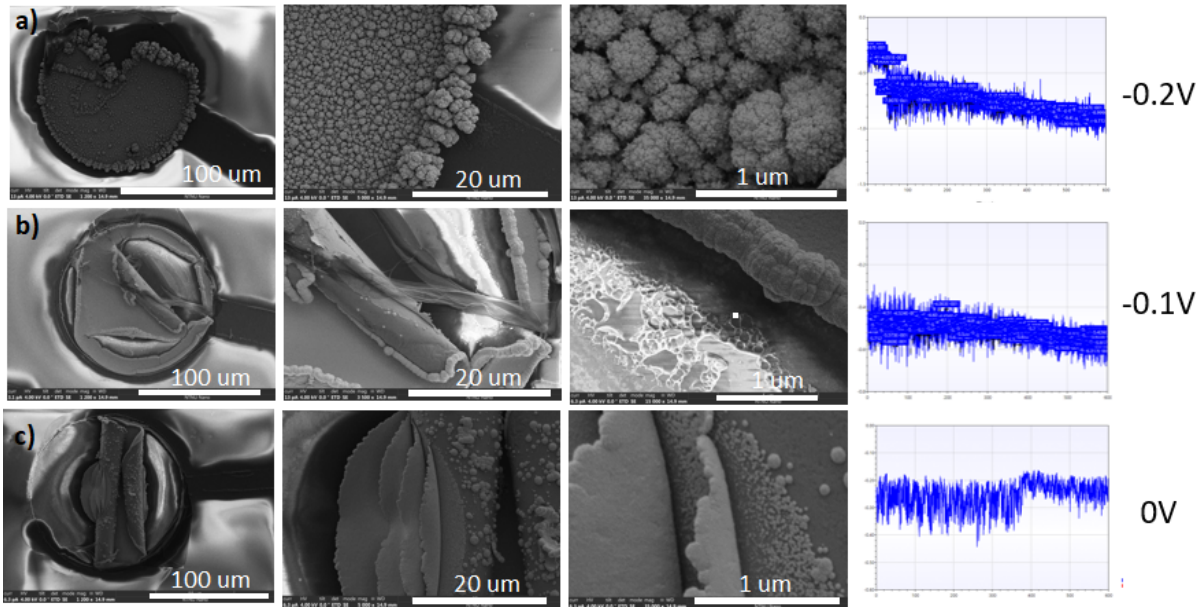

Fig. 1 SEM images and I/t plots from depositions at a) -0.2V b) -0.1V and c) 0V, each for 10 min.

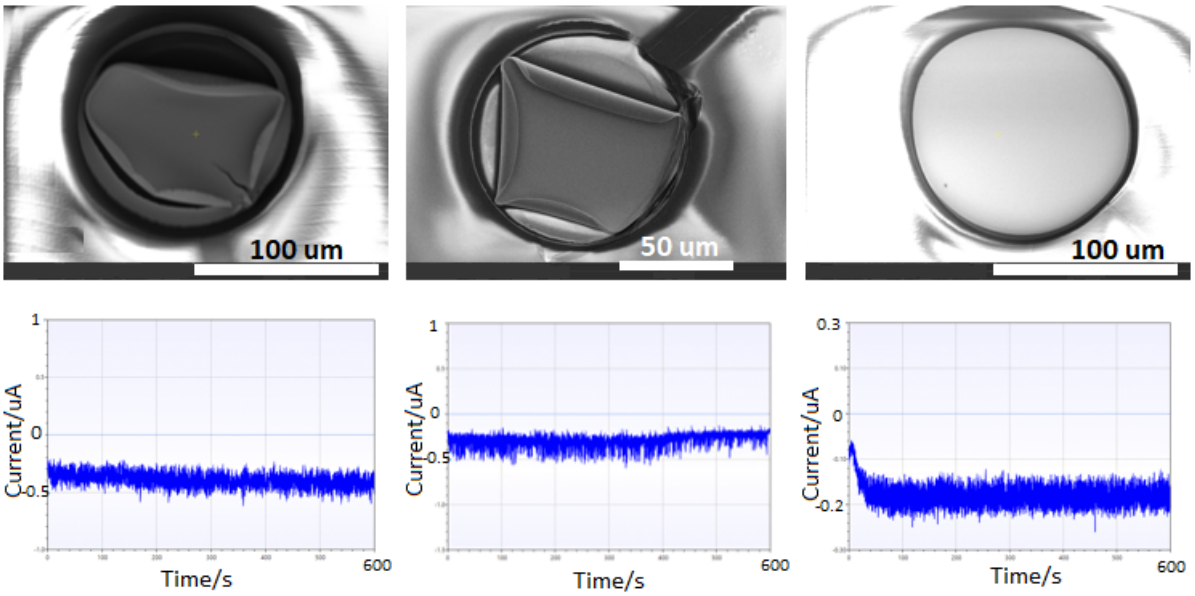

Fig. 2 SEM images from depositions on 100 um electrodes with 0.1, 0.2, and 0.3V (left to right) and the respective current measured at the electrode: -0.4, -0.3, and -0.2 uA.

A6 Protocol for seeding rat cortical neurons and astrocytes

[redacted]

Rat Cortical astrocytes and neurons

Protocol for coating and seeding in microfluidic chips

Integrative Neuroscience Group, April 2021

Introduction

- The following document gives an overview of how to coat microfluidic chips bonded to glass surfaces with laminin, and furthermore seed them with commercial rat cortical astrocytes and neurons from Sprague Dawley Rats.

Laminin Coating

1. Sterilize the microfluidic chip by placing it under UV light in a fume hood for at least one hour (preferentially overnight)
2. Put a smaller petri dish with DI water filled 50% up into the larger petri dish containing the chip (for proper hydration)
3. Remove the DI water from the wells and replace with Poly-L-ornithine (PLO) solution (make sure to have the presynaptic compartment slightly fuller than the other, so that hydrostatic pressure flushes out any remaining liquid from the channels) and incubate at 37°C for 30 minutes
4. Remove the PLO solution from the wells and replace with new PLO solution and incubate at 37°C for 1 hour
5. Remove the PLO solution and wash the chip with DI water a total of 3 times with 10 minutes in between each round (to generate flow through the channels)
6. Remove the water from the chambers and replace with laminin solution consisting of:
    - 96% L15 (*found in cell lab fridge*)
    - 2.4% sodium bicarbonate (*found in drawer next to cell lab fridge*)
    - 1.6% laminin (*found in -80°C freezer*)

    (or equivalent proportions depending on the amount needed)

    OBS: The laminin should be defrosted in the fridge. While defrosting the laminin: Mix the sodium bicarbonate and L15 together in a 15mL tube and place in the fridge to cool down. Remember to not touch the laminin vial (pick it up by the top) to avoid heating it up (which will cause gelling).

7. Incubate at 37°C for 30 minutes

8. Remove the solution from the wells and replace with a new laminin solution. Incubate at 37°C for 2 hours.

If coating and seeding will not be performed the same day: Leave the chip in the fridge overnight to avoid too excessive gelling of the laminin.

Seeding of rat cortical astrocytes

1. Remove the laminin solution and replace with pre-warmed astrocyte cell media consisting of:
    - 83% D-MEM, high glucose (*found in cell lab fridge*)
    - 15% Gibco Fetal Bovine Serum (FBS) (*found in cell lab freezer*)
    - 2% Penicillin-Streptomycin (*found in cell lab freezer*)

2. Remove the rat primary cortical astrocytes from liquid nitrogen storage, and immediately transfer the cells to a 37°C water bath to prevent crystal formation. This is crucial, as the storage medium is toxic to the cells.

3. Thaw the vial of cells by gently swirling it in the 37°C water bath, and remove it immediately when all the ice has melted (approximately 2 minutes)

4. Gently transfer the cells into a pre-rinsed 15-mL centrifuge tube with 10mL astrocyte cell media (one drop/second). Rinse the vial with 1 mL of astrocyte cell media and transfer to the centrifuge tube to make sure all astrocytes have been transferred and resuspend slowly.

5. Centrifuge the cells at 250·g for 5 minutes.

6. Aspirate the supernatant and resuspend cells in 1mL of astrocyte growth medium

7. Determine the viable cell count:
    - Mix 10 µL of cell solution with 10 µL of Trypan blue (Thermofischer Scientific)
    - Use a micropipette to inject 10 µL of the mixed solution into each side of the cell count chip
    - Do a cell count of each side in the cell counter and take an average of the alive cells to find the cell count

8. Transfer approximately 2 000 cells to each cell chamber of the chip (containing roughly 50 µL medium in total)

9. Incubate at 37°C, 5% CO2, and 90% humidity

10. Allow the astrocytes to attach and start proliferation for 2 days before seeding rat cortical neurons

Protocol from supplier can be found here:
https://www.fishersci.no/shop/products/rat-primary-cortical-astrocytes/10648888#?keyword=rat%20cortical

Seeding of rat cortical neurons

1. Prepare the neural cell media consisting of:
    - 95% Neurobasal™ plus Medium (*found in cell lab fridge*)
    - 2% B-27™ Plus Supplement (50X) (*found in cell lab freezer*)
    - 1% Gibco GlutaMAX™ Supplement (*found in drawer next to cell lab fridge*)
    - 2% Penicillin-Streptomycin (*found in cell lab fridge*)

2. Remove the rat cortical neurons from liquid nitrogen storage, and immediately transfer the cells to a 37°C water bath to prevent crystal formation. This is crucial, as the storage medium is toxic to the cells.

3. Thaw the vial of cells by gently swirling it in the 37°C water bath, and remove it immediately when all the ice has melted (approximately 2 minutes)

4. Gently transfer the cells into a pre-rinsed 15-mL centrifuge tube with 500 µL neural cell media (one drop/second). Add 0.1% Rock Inhibitor to increase the survival rate of the neurons during seeding. Resuspend slowly.

5. Replace the astrocyte media in the cell chambers with neural cell media, and transfer approximately 20 000 rat cortical neurons to each cell chamber of the chip (containing roughly 50-100 µL medium in total).

6. Change 50% of the neural cell media 5 hours after seeding with fresh media

7. Change 50% of the neural cell media with fresh media the next day

8. From then on, change approximately half the cell media every third day

9. The networks start maturing and showing complex behaviour at approximately day 12-14, at which recordings can begin

Protocol from supplier can be found here:

https://www.fishersci.no/shop/products/primary-rat-cortex-neurons-sprague-dawley-2/p-7180449#?keyword=rat%20cortical

Aleksandar Kavazov

NTNU
Norwegian University of
Science and Technology